# The Microwave Response of Square Mesh Metamaterials

Celia Amy Macklin Butler
School of Physics
University of Exeter

A thesis submitted for the degree of
*Doctor of Philosophy in Physics*
May 2012

# The Microwave Response of Square Mesh Metamaterials

Submitted by Celia Amy Macklin Butler to the University of Exeter
as a thesis for the degree of Doctor of Philosophy in Physics
May 2012

I certify that all material in this thesis which is not my own work has been identified and that no material has previously been submitted and approved for the award of a degree by this or any other University.

Celia Amy Macklin Butler
May 2012

# Acknowledgements

I would like to take this opportunity to thank everybody who has contributed (both directly and indirectly) towards this project.

I would like to thank Roy for being my constant inspiration, for guiding me through my PhD. Roy's curiosity and unique insight have always captivated me from the first lecture. I would like to thank Alastair firstly for supervising my project, but more for being on hand and involved day to day, and for the conference entertainment - the gingham mop cap really suited you! My thanks also go to my mentor Ian Summers.

I would like to thank all my friends from the lab both past and present; Biggy, Helen, Mel, Lizzy, Tim, Dima, Simon Berry, Simon Richards, Ciaran, James Edmunds, Toby, those who emerge from the basement: Ed, Caz, Chris, Tom, Alfie, Matt Nixon, Steve, and Baptiste, and honorary G31 members: Sam, Pete, and Joe. For the BBQs on the G31 "patio", the incidents with the hazard tape, and conference "prizes" (including the cow print apron and Gertrude). Also Nina, Joe, Laura and Ali all fairly new to the group.

I would like to thank Matt Lockyear, James Parsons, Ian, Euan, and Martyn Gadsdon for their support and collaboration at various stages of this project. My thanks also go to Bill, and Pete V for being on hand to talk through ideas.

I would like to thank QinetiQ, in particular Pete Hobson and Chris Lawrence for being so much more than just a funding body. For providing access to their labs, knowledge, and also their PhD experiences. Also to Rich Willis who always predicted I would undertake a PhD - you were right all those years ago! I would also like to thank Phil Pering, and James Watts at Flann Microwave for letting me bombard them with questions about the VNA and microwave components. Plus to Jim Trethewey for sanity.

I must also thank the tireless efforts of the workshop, in particular Nick, for the shoe stretcher that made my bridesmaid shoes bearable! And to Paul for hours of discussion which almost made me trailer my wreck of Land Rover down to work on (luckily I didn't as I don't think Ad would have forgiven me!), and to Matt, John, Kev, Russ, Adam and Pete Cann, for letting me wander around the workshop asking questions.

I must also mention here my real world distractions that have kept me grounded during my research. To 3rd Crediton Brownies, leaders and helpers Jill, Linda, Katie, Kathy, Chloe and Becky, hopefully I have inspired a few of you to look at science in a new light. To the Exeter Open Award Centre, to the leaders Bob, Michelle, and Kevin plus fellow "Golden Oldies" Brendon, Matt, Rosie, and Chris who helped me complete my Gold Duke of Edinburgh's Award. I will never forget the nights wild camping, and the flapjack and jelly cubes to tempt me up hills! To Exeter Firebugs (Network) and Hades (Scout Active Support), for reminding me there is so much to life than the lab. To Chipping Campden Guides and North Cotswold Rangers for our annual back to basics camp, in particular to Rosemary Grimes, Kathleen Punchard, Kate Grimes and Abby Young, for giving me so many treasured memories of bonfires, bubbles and collecting glow sticks in the middle of a thunderstorm! And to my new GOLD team Sophie (our glorious leader), Vanessa, Kirstie, Sophie and Lindsey for giving me something to look forward to on those dark days in the cupboard.

Finally I must thank the people who have made this possible, to my wonderful Mum and Dad who have tirelessly supported and encouraged me throughout my education and life. To my brother Patrick who has constantly made me jealous with his choice of employment (even the swift exit from Tripoli, Libya in Feb 2011), and to Sam for her help and support. And finally to Adam, the house is almost finished and I admit the 2 months with no flushing toilet, bath or shower were "fun" in retrospect. Adam literally put up with me being so ecstatically happy I couldn't sleep, and has also given me a hug when I needed it most. I cannot say how much I have appreciated you being there for me.

Without each and every one of you this would not have been possible!

# Abstract

Metamaterials are a class of artificial material, known to produce electromagnetic (EM) responses not found in nature due to their engineered subwavelength structure. In this thesis very thin subwavelength meshes are utilised to form layered metamaterials. The EM characteristics of the transmission and reflection response from these materials, including the polarisation converting behaviour, are explored to further understanding and develop structures to exploit and control the propagation of microwave radiation.

Original experimental studies are presented across two sections; the first examines the response of stacks assembled from metallic meshes and dielectric plates; the second explores a rotated layered structure formed of square symmetric elements in a square subwavelength array that demonstrates chirality through evanescent coupling of the near fields.

When metallic meshes are excited with EM radiation below the cut off frequency, only evanescently decaying fields are supported in the holes. By combining these subwavelength metallic meshes with dielectric plates in different arrangements, remarkably wide bands of high transmission and low reflection may be observed. The non-interacting resonant modes allow the response to be tuned through a suitable choice of the metallic mesh geometry and the properties of the dielectric. Further the low frequency band edge and the bandwidth are not dependent on the number of unit cells in the stack; but are dependent on the properties of the unit cell.

The second section demonstrates “evanescent handedness” proposed as a new type of chirality. Two subwavelength square arrays of square elements are rotated with respect to one another. When the rotated arrays are positioned far from one another in the propagation direction, each acts as an effective medium layer. However when placed in close proximity the structure is shown to rotate the plane of polarisation of the incident radiation.

All these mesh based structures share the property of producing an EM response that is tunable by design, allowing a structure to be tailored to a specific application.

# Contents

# List of Figures

# List of Tables

# Chapter 1

# Introduction

## 1.1 Aim of Research

The work presented in this thesis focuses on understanding and developing subwavelength metamaterial structures built from mesh structures for the control of microwave propagation. Although the material classification of “metamaterial” describing media with artificial subwavelength structure is relatively new, the exploitation of composite materials used for electromagnetic (EM) control is much older, having been used in stained glass and mirrors for centuries. Structures containing meshes in the microwave regime have been studied over many years as frequency selective surfaces (FSSs) utilising the resonant response close to the onset of diffraction for filters and antennae such as those in books by Munk [1] and Wu [2] (and references therein).

The publication of Ebbesen *et al.*’s seminal paper on enhanced optical transmission through an array of subwavelength holes [3] sparked new interest in this field of metallic meshes (also referred to as hole arrays). Ebbesen and co-workers reported transmission intensities many orders of magnitude larger than previously proposed by Bethe [4] for an isolated hole, and a wealth of work shortly followed to explain this phenomenon as transmission enhanced by diffractively coupled surface waves [5].

In this thesis very thin subwavelength meshes form the basis of metal–dielectric metamaterial structures to undertake novel experimental investigations into the microwave response of structures that are tunable by design.

## 1.2 Outline of Thesis

In this thesis the EM response of mesh based metamaterial structures is considered. In order to perform such studies, Chapter 2 provides a review of the mechanisms by which metallic meshes may transmit EM radiation. First by considering each hole as supporting quantised waveguide modes; continuing to discuss the binding of surface waves and the enhanced optical transmission or extraordinary transmission phenomena; and finally reviewing the advancement in understanding of subwavelength structure and metamaterials for EM propagation and control.

In Chapter 3 the techniques used to simulate the observed EM experimental results are discussed. Specific attention is paid to using Finite Element Method (FEM) to model thin metallic meshes. A brief overview of Finite Difference Time Domain (FDTD), Moment of Methods (MoM), LCR circuit theory, and modal matching is given as an alternative to FEM.

Chapter 4 considers the experimental methods used to observe the results presented in this thesis. This starts with a discussion of the apparatus used, followed by the interchangeable reflection and transmission arrangement for planar and stacked samples.

Chapter 5 considers a simple metamaterial structure comprising a metallic mesh symmetrically surrounded by subwavelength thickness dielectric layers, and is shown to give near total microwave transmission over a broad frequency range. The metallic mesh may be considered to be a tunnel barrier since it behaves as an ideal plasmonic metamaterial with a negative effective permittivity and no loss. The introduction of the metallic mesh into the dielectric cavity imposes a finite gradient on the electromagnetic fields at the two metallic mesh–dielectric interfaces. This defines a finite wavelength of the zeroth order Fabry–Pérot–like mode, which would otherwise be infinite. Suitable choice of the metallic mesh parameters yields a broad band of near total transmission associated with the overlap of this zeroth order mode, with that of the first order half–wavelength Fabry–Pérot–like resonance.

Chapter 6 considers the origins and tunability of the resonant modes supported by a thin metallic mesh stacked between thick dielectric slabs. The resonant field profiles are numerically modelled revealing that neighbouring dielectric cavities oscillate in and out of phase depending on the hyperbolic form of the evanescent field inside the subwavelength holes of the metallic mesh that separates the dielectric layers. Interestingly the lowest frequency resonant modes and the bandwidth are not dependent on the number of unit cells in the stack, only the properties of the unit cell.

In Chapter 7 the microwave reflection response is experimentally measured for a stack consisting of alternating thickness metallic meshes spaced by thick dielectric. By numerically modelling the reflection response as the metallic meshes evolve from being identical to dissimilar thicknesses, a defect mode is observed in the formation of the band gap.

In Chapter 8 the chiral EM responses of double layers of subwavelength metallic meshes and metallic patch arrays are considered. The response is shown to be due to the evanescent coupling of the near fields between the layers - it exhibits "evanescent handedness". Despite each layer being intrinsically non–chiral and isotropic, significant polarization rotation was found in the resonant microwave transmission for any incident linear polarization.

In Chapter 9 the general conclusions from this thesis are made and suggestions for further study are presented.

# Chapter 2

# Transmission Through Metallic Meshes

## 2.1 Introduction

The focus of the experimental investigations within this thesis mainly concern the transmission of electromagnetic (EM) radiation through a metallic mesh as an array of holes. The EM response can be split into three frequency regimes. The regime where the incident wavelength is much smaller than the feature size (pitch and hole size) of the array where transmission through the metallic mesh can be considered using classical ray theory. The regime where the incident wavelength is much greater than the feature size, that considers the metallic mesh as an effective homogeneous medium. This can only be implemented when the layers act independently, and do not interact via near fields. The final regime is where the feature size is comparable to the wavelength. Although the metallic meshes explored within this thesis are all studied in the subwavelength regime, it is important to consider the situation where the feature size is comparable to the incident wavelength as this provides a basis for discussions within this thesis. This chapter will overview the mechanisms that allow transmission when the incident wavelength is comparable to the hole size $\lambda \sim a$, comparable to the pitch $\lambda \sim d$ $(\lambda > a)$, and finally when the wavelength is much larger than the pitch and hole size $\lambda >> d > a$.

Here and throughout this thesis the real and imaginary parts of a complex variable, $A$, is denoted by $A'$ and $A''$ respectively.

## 2.2 Microwave Response When the Incident Wavelength is Comparable to the Hole Size

In the regime where the incident radiation has a free space wavelength comparable to the hole size of the metallic mesh, a series of quantisations within the holes produce resonant modes, allowing strong transmission, and minimum reflection at these frequencies.

The square holes of the metallic mesh are considered as hollow metallic tubes supporting resonant modes with possible quantisations in three directions. This system is more commonly referred to as a waveguide. Commercial waveguides have been heavily developed since the 1960s for RADAR (RAdio Detection And Ranging), communication systems, and printed circuit board structures (also referred to as strip line) [6–10].

The experimental studies in this thesis all utilise thin metallic meshes at microwave frequencies ($< 100\mu$m thick, $\sim \lambda/150$) therefore no quantisations are considered in the propagation direction. When neglecting the diffraction into and out of the waveguide it is reasonable to approximate the cut–off frequency (below which no propagating modes are allowed, discussed later) of the very thin metallic mesh as a series of infinitely long waveguides, as no quantisation occurs in the propagation direction (defined here as the $z$ direction as shown in Figure 2.1). Therefore, the discussion in this thesis will be limited to quantisation orthogonal to the propagation direction i.e. in the $xy$-plane.

A comprehensive derivation of the electric and magnetic fields ($\mathbf{E}$ and $\mathbf{H}$ fields) for transverse electric and transverse magnetic resonant modes (defined below) for a generic waveguide with an arbitrary cross-section, followed by rectangular, circular, and annular cross-sections is developed from [6] and shown in [11]. The following derivation is based on this work, and adapted for a waveguide with a square cross-section. From this the form of the propagation constant and the cut–off frequency is found that is of great use throughout the following sections of this chapter, and later in this thesis.

### 2.2.1 Generic Waveguide Modes

In order to derive the resonant modes within a waveguide with a square cross-section, the boundary conditions of the structure are first defined. Here it will be assumed that the walls of the square waveguide are perfectly electrically conducting (PEC), implying that all fields are excluded from this region.

By applying Maxwell's equations and Gauss's law, using a 'pillbox' method spanning the interface, assuming uniform fields over it, and assuming one side of the rectangle in a region where $\mathbf{E} = \mathbf{B} = 0$, expressions 2.1–2.4 are found:

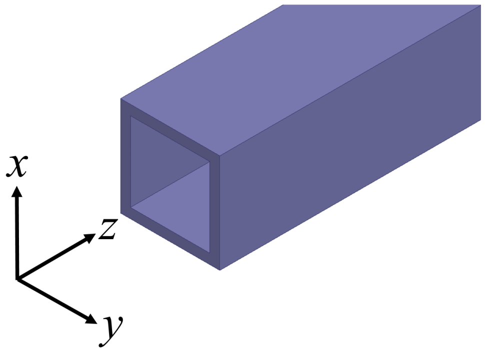

Figure 2.1: Schematic showing a single metallic waveguide with a square cross section in the $xy$ plane, extending to infinity in the $z$ (propagation) direction.

$$\hat{n} \cdot \mathbf{D} = \rho, \tag{2.1}$$

$$\hat{n} \cdot \mathbf{B} = 0, \tag{2.2}$$

$$\hat{n} \times \mathbf{E} = 0, \tag{2.3}$$

$$\hat{n} \times \mathbf{H} = \mathbf{J}, \tag{2.4}$$

where $\hat{n}$ is the unit vector normal to the surface, $\mathbf{D}$ is the electric flux density, $\rho$ is the electric charge density (or the free surface charge), $\mathbf{B}$ is the magnetic flux density, $\mathbf{E}$ is the electric field intensity, $\mathbf{H}$ is the magnetic field intensity and $\mathbf{J}$ is the electric current density (or the free surface current density).

Now assume that the fields vary in time with a harmonic oscillation represented by $e^{j\omega t}$, where $j = \sqrt{-1}$, $\omega$ is the angular frequency and $t$ is time. Then the spatial parts of $\mathbf{E}$ and $\mathbf{H}$ can be written as:

$$\mathbf{E} = (\bar{E}(x,y) + \hat{z}E_z(x,y))e^{-jk_z}, \tag{2.5}$$

$$\mathbf{H} = (\bar{H}(x,y) + \hat{z}H_z(x,y))e^{-jk_z}, \tag{2.6}$$

where $\bar{E}(x,y)$ and $\bar{H}(x,y)$ are the transverse field components, $E_z$ and $H_z$ are the axial components, and $k_z = \frac{2\pi}{\lambda}$, the wave vector of the incident radiation. From Maxwell's equations:

$$\nabla \times \mathbf{E} = -j\omega\mu\mathbf{H}, \tag{2.7}$$

$$\nabla \times \mathbf{H} = j\omega\varepsilon\mathbf{E}, \tag{2.8}$$

where $\mu$ is the relative permeability and $\varepsilon$ is the relative permittivity. The axial dependence means that the three components in each of the equations above can be reduced to:

$$\frac{\partial E_z}{\partial y} + jk_z E_y = -j\omega\mu H_x, \tag{2.9}$$

$$-\frac{\partial E_z}{\partial x} - jk_z E_x = -j\omega\mu H_y, \tag{2.10}$$

$$\frac{\partial E_y}{\partial x} - \frac{\partial E_x}{\partial y} = -j\omega\mu H_z, \tag{2.11}$$

$$\frac{\partial H_z}{\partial y} + jk_z H_y = -j\omega\varepsilon E_x, \tag{2.12}$$

$$-\frac{\partial H_z}{\partial x} - jk_z H_x = j\omega\varepsilon E_y, \tag{2.13}$$

$$\frac{\partial H_y}{\partial x} - \frac{\partial H_x}{\partial y} = -j\omega\varepsilon E_z. \tag{2.14}$$

Now combine these to give expressions for $H_x, H_y, E_x, E_y$ (the transverse components) in terms of $E_z$ and $H_z$ (the axial components),

$$H_x = \frac{j}{k_c^2}\left(\omega\varepsilon\frac{\partial E_z}{\partial y} - k_z\frac{\partial H_z}{\partial x}\right), \tag{2.15}$$

$$H_y = \frac{-j}{k_c^2}\left(\omega\varepsilon\frac{\partial E_z}{\partial x} - k_z\frac{\partial H_z}{\partial y}\right), \tag{2.16}$$

$$E_x = \frac{-j}{k_c^2}\left(k_z\frac{\partial E_z}{\partial x} + \omega\mu\frac{\partial H_z}{\partial y}\right), \tag{2.17}$$

$$E_y = \frac{j}{k_c^2}\left(k_z\frac{\partial E_z}{\partial y} - \omega\mu\frac{\partial H_z}{\partial x}\right), \tag{2.18}$$

where $k_c^2 = \omega^2\varepsilon\mu - k_z^2 = k_0^2 - k_z^2$ is the cut–off wave number. These equations describe the generic transverse electric and magnetic fields within any arbitrary cross-section of an infinitely long waveguide with PEC walls.

#### 2.2.1.1 Types of Waves

At this point the type of wave supported by the system is considered. There are three types, transverse electric (TE, also known as s-polarised), transverse magnetic (TM, also known as p-polarised) and transverse electric and magnetic (TEM). TE waves are characterised by $E_z = 0$ and $H_z \neq 0$, TM waves are characterised by $E_z \neq 0$ and $H_z = 0$, and finally TEM waves are characterised by $E_z = H_z = 0$. In the following section TE waves are considered, followed by TM for an arbitrary waveguide, then the geometry of the cross–section is applied. TEM waves are not supported by this structure (and are not considered further) as in order for both the electric and magnetic vectors to be transverse two electrically conducting elements are required. However, TEM modes may be supported by waveguide geometries with two or more separate conductors such as, coaxial or parallel plate waveguide systems. For more information see [6]. Definitions of the polarisation for the experimental investigations in transmission and reflection can be found in sections 4.3 and 4.4 respectively.

#### 2.2.1.2 TE Waveguide Modes for an Arbitrary Waveguide

By applying the condition that $E_z = 0$ and $H_z \neq 0$ to Equations 2.15 to 2.18, the following equations hold:

$$H_x = \frac{-jk_z}{k_c^2}\frac{\partial H_z}{\partial x}, \tag{2.19}$$

$$H_y = \frac{jk_z}{k_c^2}\frac{\partial H_z}{\partial y}, \tag{2.20}$$

$$E_x = \frac{-j\omega\mu}{k_c^2}\frac{\partial H_z}{\partial y}, \tag{2.21}$$

$$E_y = \frac{j\omega\mu}{k_c^2}\frac{\partial H_z}{\partial x}. \tag{2.22}$$

From these equations, to find the particular TE resonant mode supported by a specific geometry waveguide, an expression for $H_z$ must be found. This can be done using the Helmholtz wave equation:

$$\nabla^2\mathbf{H} - \omega^2\mu\varepsilon\mathbf{H} = 0, \tag{2.23}$$

as introduced at the beginning, $H_z(x, y, z) = H_z(x, y)e^{-jk_z z}$, so Equation 2.23 reduces to 2.24 (below) which can be applied to the square geometry in section 2.2.2.1

$$\left(\frac{\partial^2}{\partial x^2} + \frac{\partial^2}{\partial y^2} + k_c^2\right) H_z = 0. \tag{2.24}$$

#### 2.2.1.3 TM Waveguide Modes for an Arbitrary Waveguide

By applying the condition that $E_z \neq 0$ and $H_z = 0$ to Equations 2.15 to 2.18, the following equations hold:

$$H_x = \frac{j\omega\varepsilon}{k_c^2}\frac{\partial E_z}{\partial y}, \tag{2.25}$$

$$H_y = \frac{-j\omega\varepsilon}{k_c^2}\frac{\partial E_z}{\partial x}, \tag{2.26}$$

$$E_x = \frac{-jk_z}{k_c^2}\frac{\partial E_z}{\partial x}, \tag{2.27}$$

$$E_y = \frac{jk_z}{k_c^2}\frac{\partial E_z}{\partial y}, \tag{2.28}$$

As in the TE case the wave equation can be used and reduced to the 2D wave equation for $E_z$:

$$\left(\frac{\partial^2}{\partial x^2} + \frac{\partial^2}{\partial y^2} + k_c^2\right) E_z = 0. \tag{2.29}$$

### 2.2.2 The Square Waveguide

Here the geometry of the waveguide is applied to the 2D wave equation found for $E_z$ and $H_z$ (Equations 2.24 and 2.29), to find the unknown constants $k_x$ and $k_y$. Consider a tube with a square cross-section, filled with a lossless material (permittivity $\varepsilon$, permeability $\mu$), formed of PEC material as shown in Figure 2.1. One corner of the tube lies at

$x = y = z = 0$. The tube extends to infinity in the $z$ direction. The sides of the tube are equal and of length $a$ in the $x$ and $y$ directions.

#### 2.2.2.1 The TE Solution

Starting with Equation 2.24, separation of variables can be used to turn the partial differential equations into ordinary differential equations, as below:

$$\frac{1}{X}\frac{d^2X}{dx^2} + \frac{1}{Y}\frac{d^2Y}{dy^2} + k_c^2 = 0, \tag{2.30}$$

where $H_z(x, y) = X(x)Y(y)$. As each term must be equal to a constant the equations can be separated to form Equations 2.30 into two equations:

$$\frac{d^2X}{dx^2} + k_x^2 X = 0, \tag{2.31}$$

$$\frac{d^2Y}{dy^2} + k_y^2 X = 0, \tag{2.32}$$

where:

$$k_x^2 + k_y^2 = k_c^2. \tag{2.33}$$

The general form of $H_z$ can now be written as:

$$H_z(x, y) = (A\cos k_x x + B\sin k_x x)(C\cos k_y y + D\sin k_y y), \tag{2.34}$$

By considering the waveguide geometry, the boundary conditions can be applied (below), and use Equations 2.21 and 2.22 (which express $E_x$ and $E_y$ as a function of $H_z$ to form Equations 2.35 and 2.36).

$$E_x(x, y) = 0 \begin{cases} y = 0 \\ y = a \end{cases}$$

$$E_y(x, y) = 0 \begin{cases} x = 0 \\ x = a \end{cases}$$

$$E_x = \frac{-j\omega\mu}{k_c^2} k_y (A\cos k_x x + B\sin k_x x)(-C\sin k_y y + D\cos k_y y), \tag{2.35}$$

$$E_y = \frac{-j\omega\mu}{k_c^2} k_x(-A\sin k_x x + B\cos k_x x)(C\cos k_y y + D\sin k_y y). \tag{2.36}$$

When the boundary conditions are applied to Equations 2.35 and 2.36, it is clear that when $x = 0$; $B = 0$, and when $x = a$; $k_x = \frac{m\pi}{a}$, similarly when $y = 0$; $D = 0$ and when $y = a$; $k_y = \frac{m\pi}{a}$. Where $m$ and $n$ are integer numbers that represent the mode number (number of quantisations in the $x$ and $y$ directions respectively). By combining these the final solution for $H_z$ is:

$$H_z(x, y, z) = A_{mn} \cos\frac{m\pi x}{a} \cos\frac{n\pi y}{a} e^{-jk_z z}, \tag{2.37}$$

where $A_{mn}$ is a constant composed of $A$ and $C$ from Equations 2.35 and 2.36. From this, the transverse fields $E_x, E_y, H_x, H_y$ can be found (Equations 2.38 to 2.41) as well as the propagation constant $k_z$ (Equation 2.42):

$$E_x = \frac{j\omega\mu n\pi}{k_c^2 a} A_{mn} \cos\frac{m\pi x}{a} \sin\frac{n\pi y}{a} e^{-jk_z z}, \tag{2.38}$$

$$E_y = \frac{-j\omega\mu m\pi}{k_c^2 a} A_{mn} \sin\frac{m\pi x}{a} \cos\frac{n\pi y}{a} e^{-jk_z z}, \tag{2.39}$$

$$H_x = \frac{jk_z m\pi}{k_c^2 a} A_{mn} \sin\frac{m\pi x}{a} \cos\frac{n\pi y}{a} e^{-jk_z z}, \tag{2.40}$$

$$H_y = \frac{jk_z m\pi}{k_c^2 a} A_{mn} \cos\frac{m\pi x}{a} \sin\frac{n\pi y}{a} e^{-jk_z z}, \tag{2.41}$$

$$k_z = \sqrt{k_0^2 - k_c^2} = \sqrt{k_0^2 - (m\pi/a)^2 + (n\pi/a)^2}. \tag{2.42}$$

The propagation constant ($k_z$) is real when $k_0$ is greater than the cut–off wave number ($k_c$). Each mode supported by the square waveguide has a cut–off frequency below which the mode will not propagate given by:

$$f_c = \frac{1}{2\pi\sqrt{\varepsilon\mu}} \sqrt{(m\pi/a)^2 + (n\pi/a)^2}. \tag{2.43}$$

Discrete solutions to the cut–off wave number only occur when $m$ and $n$ are integers. This is due to the physical boundary conditions of the waveguide structure (i.e. $\mathbf{E} = 0$ at the PEC walls) in the $x$ and $y$ direction implying discrete quantisations across the waveguide. The cut–off frequency for the first three TE modes supported by this structure can be seen in table 2.1 and the corresponding field profiles shown in Figure 2.2.

| $m$ | $n$ | Frequency (GHz) |
|---|---|---|
| 1 | 0 | 29.979 |
| 1 | 1 | 42.397 |
| 2 | 0 | 59.958 |

Table 2.1: Cut off frequencies for the first three TE waveguide modes, for a PEC, air filled square cross-section waveguide with side length $a = 5$ mm.

#### 2.2.2.2 The TM Solution

As discussed above for TE modes, separation of variables (Equation 2.30) can be used to find a series of equations using full differentials from the 2D wave equation (Equation 2.29). The general solution is given by:

$$E_z(x, y) = (A \cos k_x x + B \sin k_x x)(C \cos k_y y + D \sin k_y y). \tag{2.44}$$

Now apply the boundary conditions, however this time they can be applied directly to $E_z$.

$$E_z(x, y) = 0 \begin{cases} x = 0 \\ x = a \end{cases}$$

$$E_z(x, y) = 0 \begin{cases} y = 0 \\ y = a \end{cases}$$

$$E_z(x, y, z) = B_{mn} \sin \frac{m\pi x}{a} \sin \frac{n\pi y}{a} e^{-jk_z z}. \tag{2.45}$$

By substituting Equations 2.45 into Equations 2.25 to 2.28 the transverse fields ($E_x$, $E_y$, $H_x$, and $H_y$) can be found.

$$E_x = \frac{-jk_z m\pi}{ak_c^2} B_{mn} \cos \frac{m\pi x}{a} \sin \frac{n\pi y}{a} e^{-jk_z z}, \tag{2.46}$$

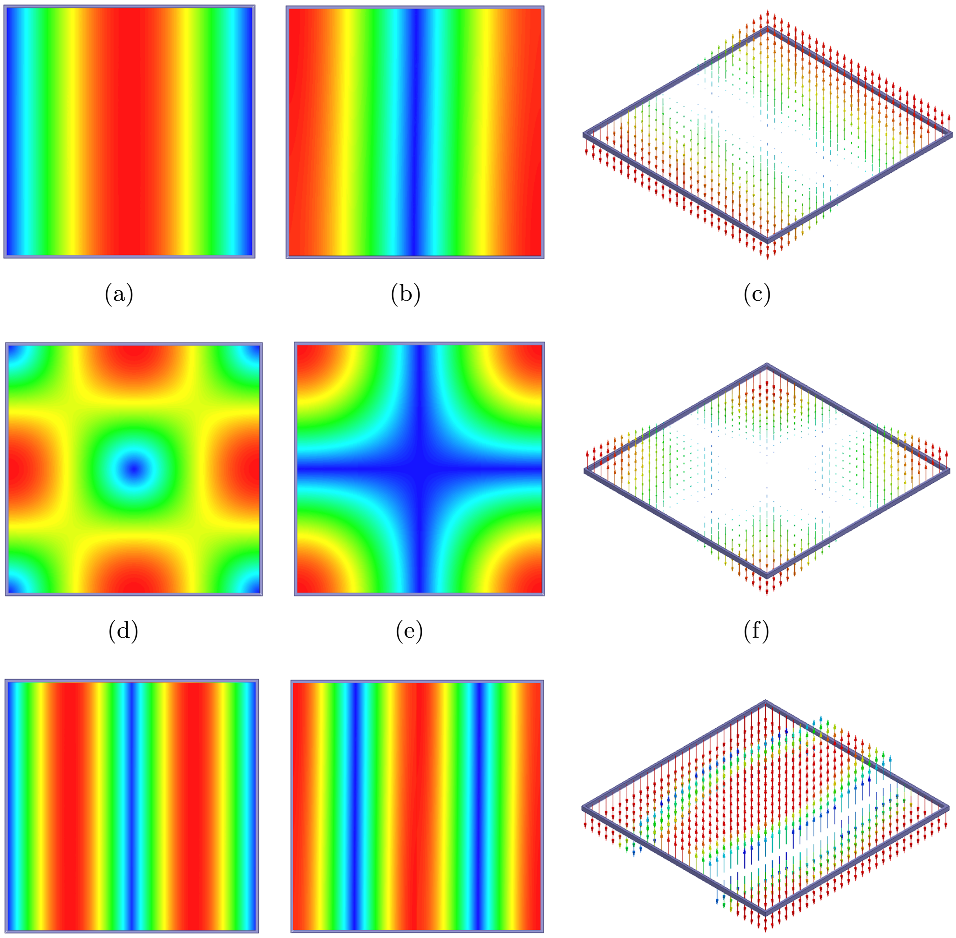

(a) (b) (c)

(d) (e) (f)

(g) (h) (i)

Figure 2.2: The first three TE waveguide modes supported in an air filled, square cross-sectional waveguide with PEC walls. Figures (a–c), (d–f), (g–i) correspond to the $TE_{10}$, $TE_{11}$, and $TE_{20}$ waveguide modes respectively plotted over a 2D sheet. Figures (a, d, g) are time averaged **E**, (b, e, h) are time averaged **H**, and (c, f, i) are vector **H** at the phase corresponding to the maximum field enhancement. Red/large arrows indicate a high **E** or **H**, blue a low **E** or **H**.

$$E_y = \frac{-jk_z n\pi}{ak_c^2} B_{mn} \sin\frac{m\pi x}{a} \cos\frac{n\pi y}{a} e^{-jk_z z}, \tag{2.47}$$

$$H_x = \frac{j\omega\varepsilon n\pi}{ak_c^2} B_{mn} \cos\frac{m\pi x}{a} \sin\frac{n\pi y}{a} e^{-jk_z z}, \tag{2.48}$$

$$H_y = \frac{-j\omega\varepsilon m\pi}{ak_c^2} B_{mn} \cos\frac{m\pi x}{a} \sin\frac{n\pi y}{a} e^{-jk_z z}, \tag{2.49}$$

The propagation constant is given by Equation 2.50:

$$k_z = \sqrt{k_0^2 - k_c^2} = \sqrt{k_0^2 - (m\pi/a)^2 - (n\pi/a)^2}. \tag{2.50}$$

The propagation constant ($k_z$) is real when $k_0$ is greater than the cut–off wave number. Each mode supported by the square waveguide has a cut–off frequency given by:

$$f_c = \frac{1}{2\pi\sqrt{\varepsilon\mu}} \sqrt{(m\pi/a)^2 + (n\pi/a)^2}. \tag{2.51}$$

This has the same form as the cut–off frequency for the TE waveguide modes, however here if either $m = 0$, or $n = 0$ then $\bar{E} = \bar{H} = 0$ (the transverse field components). Physically this is due to the boundary conditions of the structure, the magnetic field cannot be constant across the waveguide as there are no magnetic monopoles. Therefore the first allowed TM mode in this waveguide structure is the TM$_{11}$. The cut–off frequency for the first three TM waveguide modes supported by this structure are shown in table 2.2 and the corresponding field profiles are shown in Figure 2.3.

| $m$ | $n$ | Frequency (GHz) |
|---|---|---|
| 1 | 1 | 42.397 |
| 2 | 1 | 67.0356 |
| 2 | 2 | 84.794 |

Table 2.2: Cut off frequencies for the first three TM waveguide modes, for an PEC, air filled square cross section waveguide with side length $a = 5$ mm.

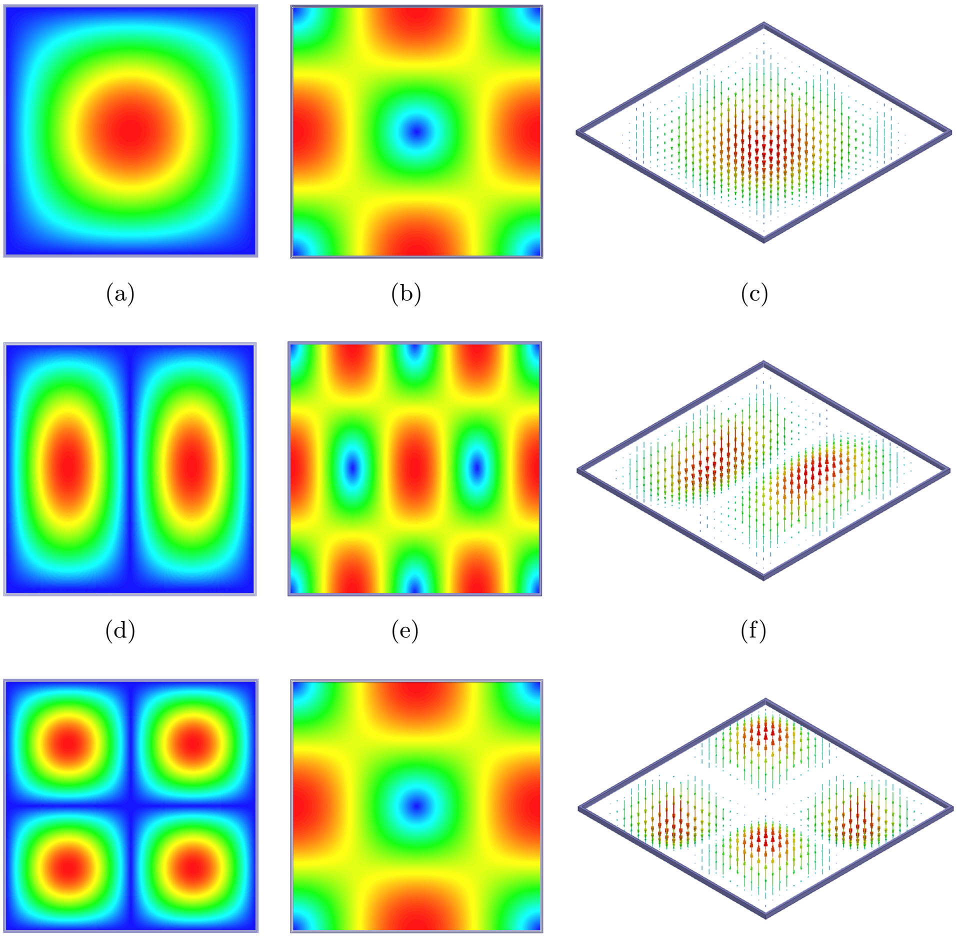

(a) (b) (c)

(d) (e) (f)

(g) (h) (i)

Figure 2.3: The first three TM waveguide modes supported an air filled, square cross-sectional waveguide with PEC walls. Figures (a - c), (d - f), (g - i) correspond to the $TM_{11}$, $TM_{21}$, and $TM_{22}$ waveguide modes respectively plotted over a 2D sheet. Figures (a, d, g) plot time averaged **E**, (b, e, h) plot time averaged **H**, and (c, f, i) plot vector **E** at the phase corresponding to the maximum field enhancement. Red/large arrows indicates a high **E** or **H**, blue a low **E** or **H**.

## 2.3 Microwave Response When the Incident Wavelength is Comparable to the Pitch

When the wavelength of radiation incident on an object is comparable to the pitch, propagating diffracted orders are expected. In the experimental section of this thesis, subwavelength holes are arranged in a square array with a subwavelength pitch of near–PEC metal, forming the metallic mesh. In this section an array with subwavelength holes and a pitch comparable to the wavelength of the incident radiation will be considered. Assumptions made in classical diffraction theory break down when propagating modes are not allowed in the subwavelength holes and evanescently decaying fields dominate (below the cut–off frequency). A thorough review of classical diffraction theory and its failings in this regime is provided by Bouwkamp [12]. Bethe proposed modelling a single aperture in a infinitely thin PEC sheet as a magnetic dipole [4]. Equation 2.52 below is the expression for Bethe's transmission for a single cylindrical hole, of radius $r$, and is only valid for normal incidence, where no propagating mode occur ($r \lesssim 0.3\lambda_{inc}$, but must be $r \leq 0.5\lambda_{inc}$, where $\lambda_{inc}$ is the incident wavelength).

$$T = \frac{64}{27\pi^2}(kr)^4 \propto \left(\frac{r}{\lambda_{inc}}\right)^4. \tag{2.52}$$

Finite thickness sheets were considered by Roberts in 1987 [13] who showed that the fields inside the holes decay near exponentially.

This theory was more recently adapted for arrays of subwavelength holes by Garcia de Abajo *et al.* [14] and Gordon [15]. Garcia de Abajo and colleagues considered the overall polarisation current of an array of infinitely thin PEC circular discs that was derived by considering the dipole coupling between discs. Using Babinet's principle (defined below), the response from an array of circular discs yields the response of the complimentary hole array.

**Babinet's Principle** states that transmission through structure '$a$' ($T_a$) will be equal to $(1 - T_b)$ where $T_b$ is the transmission through the complimentary structure '$b$', when the polarisation is rotated by 90°. Babinet's principle is limited to systems that use infinitely thin PEC screens (2D) with no absorption [16].

Gordon derived an analytical expression for the transmission given in Equation 2.53 by considering the Fourier expansions of the **E** and **H** fields and solving the field distribution for the magnetic polarisation current excited around the apertures. The agreement between these methods is good, and by considering Gordon's method it is

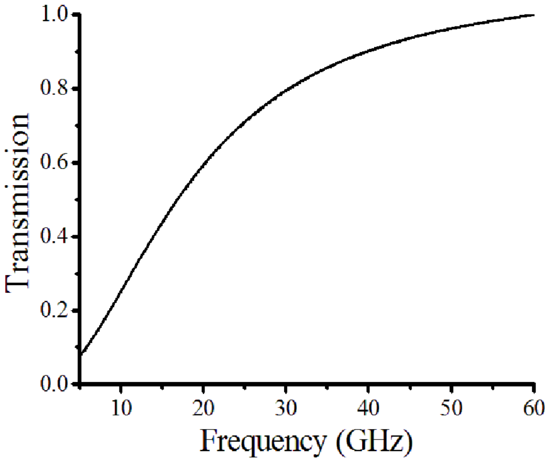

Figure 2.4: Transmission as a function of frequency, for an infinitely thin PEC metallic mesh of hole size $a = 4.85$ mm and pitch $d = 5$ mm.

revealed that in the small aperture limit (when $\lambda_{inc} > d$, where $d$ is the pitch of the hole array) it is the lowest order TM evanescent mode that dictates the transmission.

$$T = \left[1 + \left(\frac{d^2}{2\pi k}\left[\frac{\pi}{2\alpha_m} - \frac{4\pi k}{d^2\sqrt{\frac{\lambda_{inc}^2}{d^2} - 1}}\right]\right)\right]^{-2}. \tag{2.53}$$

Here $k$ is the incident wave vector ($k = \frac{2\pi}{\lambda}$), and $\alpha_m$ is a constant that depends on the hole shape; for a square hole of side length $a$, the constant $\alpha_m = \frac{\pi a^3}{16}$. Figure 2.4 shows the transmission response for a square hole of side length 4.85 mm, in a square array with a pitch $d = 5$ mm using Equation 2.53.

### 2.3.1 Surface Waves

In the following section surface wave mediated transmission is discussed, therefore the origin of surface waves on metallic structures will now be briefly considered.

As early as the beginning of the 20th century Zenneck [17] and Sommerfeld [18] had considered longitudinal propagating EM oscillations on the surfaces of conducting media [19]. In 1902 Wood reported the appearance of anomalous intensity dips in the spectra from visible light incident on a metallic grating [20]. Soon after Lord Rayleigh produced his theory of scattering from periodic structures [21]. However it was Fano in 1941 who connected these two works [22].

In the 1950s it was known that conduction electrons in metals behave like a plasma supporting collective oscillations termed ‘plasmons’. Longitudinal oscillations bound to the interface of a metal were proposed by Ritchie in 1957 [23] and were observed by Powell and Swan in 1959 [24] as an energy loss whilst investigating how the oxidation on the surface of aluminium and magnesium changes the reflection response. However an unified theory between these investigations was not realised until 1968 see ref [25]. The bound surface waves are formed when the semi-free nature of the conduction electrons in the metal layer are allowed to respond collectively, creating a wave with hybrid EM 'wave nature' and 'surface charge density oscillation' characteristics.

TM or p-polarised radiation described in section 2.2.1.1 has an electric field component normal to the interface that may excite surface charges. At the interface between a metal and an insulator the surface wave is supported when Equation 2.54 is satisfied [25], the wave is bound to the interface.

$$k_x = k_{sw} = k_0 \left( \frac{\varepsilon_1 \varepsilon_2}{\varepsilon_1 + \varepsilon_2} \right)^{\frac{1}{2}}. \tag{2.54}$$

Here $k_x$ is the wave vector in the $x$ direction, and $k_{sw}$ is the wave vector of the surface wave respectively. $k_0 = \frac{\omega}{c}$ is the free space wave number and $\varepsilon$ is the relative permittivity where subscripts 1 and 2 indicate the dielectric insulator superstrate and metallic substrate respectively as shown in Figure 2.5. In order to couple radiation to this surface oscillation extra momentum is required as $k_{sw} > k_o$. This can be imparted using grating or prism coupling (for explanations of these techniques see [26]).

In order to be 'bound' to the interface, certain conditions relating to the complex permittivity of the metal and dielectric media must be satisfied. $k_x$ must be real, and so the permittivity of the metal $\varepsilon_2 < 0$, and the wave vector in the $z$ direction (i.e. normal to the interface) $k_z$ must be imaginary, so $\varepsilon_1 + \varepsilon_2 < 0$ or put another way $|\varepsilon_2| > \varepsilon_1$ [27]. When the surface wave is bound it decays exponentially normal to the surface as shown in Equation 2.55:

$$k_{zm} = (\varepsilon_m k_0^2 - k_x^2)^{\frac{1}{2}}, \tag{2.55}$$

here subscript $m = 1$, or 2 refers to the medium being considered.

The dispersion relation (dependence of angular frequency $\omega$ on the parallel wave vector $k_{||}$) for such a wave using a Drude model for the electron gas of a metal is illustrated in Figure 2.5. At high frequencies the surface mode asymptotes toward the surface plasma frequency marked as $\omega_p/\sqrt{2}$ (general form $\omega_p/\sqrt{1+\varepsilon_1}$) where $\omega_p$ is defined by Equation 2.56 [25]:

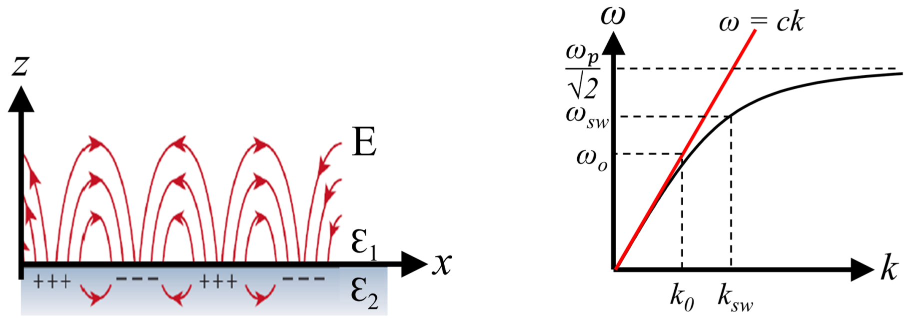

(a) (b)

Figure 2.5: (a) Schematic of the electric field vector for a bound surface wave at the interface between a metallic substrate (dark region) and dielectric superstate (white region) where the magnetic field is in and out of the page. (b) Sketched dispersion plot illustrating the nature of a surface mode as a function of angular frequency $\omega$ and in plane momentum $k$, parallel to the interface at which the surface wave propagates using a Drude model.

$$\omega_p = \sqrt{\frac{ne^2}{m\varepsilon_0}}, \tag{2.56}$$

where $n$ is the electron density, $e$ is the electron charge, $m$ is the electron mass, and $\varepsilon_0$ is the permittivity of free space. For most metals the plasma frequency lies in the ultraviolet part of the EM spectrum.

The permittivity of the metal $\varepsilon_2$ is approximated by the Drude model for a free electron gas that is frequency dependent (Equation 2.57 [28]), where $\gamma$ is the damping constant (inverse of the scattering time $\tau$). In Equations 2.58 and 2.59 the Drude permittivity is separated into its real and imaginary component parts. This assumes no decay (i.e. an infinite relaxation time $\tau \rightarrow \infty$) and no inter-band transitions occur ($\gamma \rightarrow 0$). Figure 2.6 shows the real and imaginary parts of the permittivity for aluminium where $\omega_p = 2.3 \times 10^{16}$ Hz, and $\gamma = 1.44 \times 10^{14}$ Hz. Here the negative real part of the permittivity increases with wavelength. For visible frequencies both the real and imaginary parts of the permittivity are small, both increase (negative real part and positive imaginary part) through the THz frequencies to stabilise at $\sim 10^4$ for the negative real part, and increasing through $\sim 10^9$ for the imaginary part at microwave frequencies.

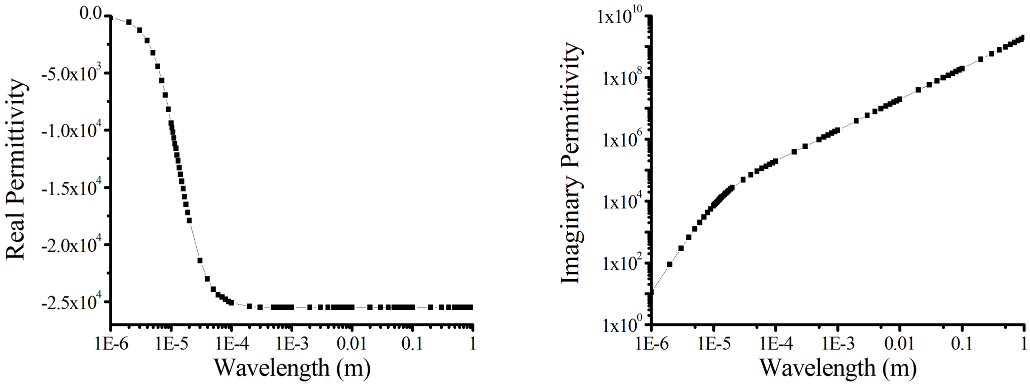

(a) (b)

Figure 2.6: Real and imaginary part of the permittivity of Aluminium using the Drude model, where $\omega_p = 2.3 \times 10^{16}$ Hz, and $\gamma = 1.44 \times 10^{14}$ Hz.

$$\varepsilon = 1 - \frac{\omega_p^2}{\omega^2 + i\gamma\omega}, \tag{2.57}$$

$$\varepsilon' = 1 - \frac{\omega_p^2}{\omega^2 + \gamma^2}, \tag{2.58}$$

$$\varepsilon'' = \frac{\omega_p^2 \gamma}{\omega(\omega^2 + \gamma^2)}. \tag{2.59}$$

At this point it is also useful to define the real and imaginary parts of the conductivity in terms of the permittivity of the metal as:

$$\sigma' = \omega \varepsilon_0 \varepsilon'', \tag{2.60}$$

$$\sigma'' = \omega \varepsilon_0 (\varepsilon' - 1). \tag{2.61}$$

The real part of the frequency dependent conductivity of a metal is proportional to the permittivity. Figure 2.7 shows the real and imaginary parts of the conductivity for aluminium, above a wavelength of 0.1 mm the real and imaginary parts of the conductivity are large (positive) and almost zero respectively. This shows that for wavelengths in the microwave regime the assumption that metals act as near PEC is valid for aluminium. At visible wavelengths a large minimum is seen in the imaginary

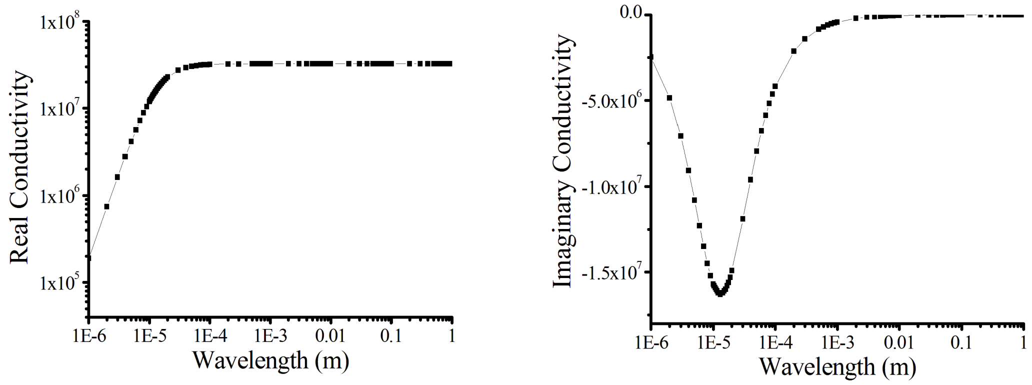

(a) (b)

Figure 2.7: Real and imaginary part of the conductivity of Aluminium using the Drude model permittivity.

conductivity and this correspond to a gradual increase in the real part. This allows EM fields to penetrate into the metal at these high frequencies.

The penetration depth is a measure of the distance into a medium at which the intensity of an EM wave reduces to $1/e$ of its initial value at the interface. It is defined by Equation 2.62 below. The form of the penetration depth is shown as a function of wavelength in Figure 2.8 for an EM wave at the interface between air and aluminium. This should not be confused with the skin depth ($\delta_s$) which is a measure of distance into the media at which the *electric field* (or magnetic field) reduces to $1/e$ of its initial value which is defined in Equation 2.63 where $\mu_0$ is the permeability of the free space. This is also referred to as the decay length.

$$\delta_m = \frac{1}{2k_z}, \tag{2.62}$$

$$\delta_s = \sqrt{\frac{2}{\omega\mu_0\sigma}} \approx \frac{1}{k_z}. \tag{2.63}$$

In the optical regime, close to the plasma frequency, the surface wave is strongly bound to the interface, decaying within $\sim 10$ nm ($\sim \frac{\lambda}{60}$) into the metal and $\sim 100$ nm ($\sim \frac{\lambda}{6}$) into the dielectric due to the negative real part and small positive imaginary part of the metal permittivity. As $\omega_{sw} \to \omega_p/\sqrt{2}$ the mode becomes more confined and the decay length into the media decreases. In this region, the surface wave is referred to as the "surface plasmon" (SP).

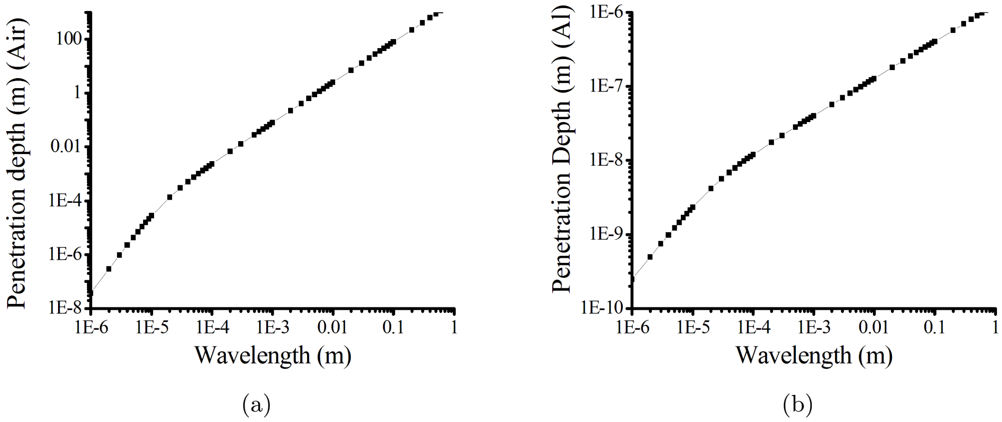

Figure 2.8: Penetration depth as a function of wavelength for an EM wave at an air–aluminium interface, where (a) is the response in air and (b) is the response in aluminium.

### 2.3.2 Enhanced Optical Transmission

As stated in section 2.3, Bethe proposed that the transmission through a single metal subwavelength hole varies as $T \propto (\frac{r}{\lambda_0})^4$. Gordon then adapted this for arrays of holes as in Equation 2.53. However, in 1998, Ebbesen *et al.* recorded enhanced optical transmission (EOT), transmission many orders of magnitude than previously proposed for an array of subwavelength holes in an optically thick film of silver close to the onset of diffraction [3]. The sharp transmission peak was several orders of magnitude larger for an array compared to the response of a single hole with the same area as the sum of all the holes in the array, where Bethe predicts a gradual increase in the transmission as the hole size tends towards the incident wavelength. Therefore many research groups theorised that it was a collective response caused by the array. Thio *et al.* showed the normalised energy integrated over the area of the hole was proportional to the number of scatters per unit area, not a function of the hole size as expected [29].

Later studies considered the transmission mechanism for an array of slits [30–32] and hole arrays [5, 33–36]. Ebbesen *et al.* conducted further experiments on choice of metal, hole size and depth [3]. Finally it was concluded that the transmission was enhanced by scattering (not necessarily periodic [37–40]) from the structure of the surface, as no EOT was seen in dielectric substrate hole arrays and the angular dependence followed that of a surface plasmon on a reflection grating. When phase matched, the constructive interference leads to three possible mechanisms for transmission [41]:

- Without supporting a surface plasmon, the EM field at the surface is enhanced but decays exponentially into the metal. Tunnelling may occur, however low transmission is recorded unless the metal is very thin.

- The scattered radiation allows the surface to support a single surface plasmon on one interface. Incident radiation couples to the SP mode, enhancing the EM fields at the interface, which allows the probability of transmission through tunnelling through the holes to increase.

- Scattered radiation from both interfaces couples into the SP mode on the upper and lower interfaces. The SPs tunnel through the holes coupling together to allow large transmission through the structure.

When not phase matched the transmission is as described in Equation 2.53. EOT has since found a vast rage of applications, in the bio-sensing and optoelectric research fields [42, 43].

### 2.3.3 Surface Waves in the Microwave Regime

In the low frequency regime, such as at microwave frequencies where the work in this thesis is conducted, metals act as near perfect conductors, as $|\varepsilon| \rightarrow \infty$. The conduction electrons are almost completely free to respond to any EM disturbances, so metals in the microwave regime are close to PEC; the EM field penetrates $< 1$ µm ($\sim \frac{\lambda}{100}$) into the metal and many 100s of wavelengths in the dielectric as shown in Figure 2.8. The dispersion of the surface wave is illustrated in Figure 2.9. The blue shaded region on the diagram shows the low frequency microwave regime where the response (black line) closely follows that of light line (red line) being “grazing photon-like”, and only loosely bound to the surface, usually referred to as a surface current due to the long propagation length.

The concept of structuring a PEC metallic surface in order to bind a surface wave to the interface in the microwave regime was extensively studied in the 1950s. Barlow and Cullen [19], produced a review paper discussing the various techniques that could be employed. However more recently, the concept was revisited to describe the effective parameters of “metamaterials” - materials with artificial subwavelength structure, discussed in section 2.4. Resonant elements such as $\frac{\lambda}{4}$ deep grooves were originally used to allow effective penetration into the metallic layer [44]. Frequency selective surfaces (FSSs) defined below, also employ resonant elements to produce selective reflection and transmission responses, however by designing suitable structures at the surface, these also allow a surface wave to bind to the interface. Since the 1950s FSSs have been used as filters [1, 2, 45–49], employing the large transmission peak that occurs close to the onset of diffraction. Ulrich [48] described this transmission peak as extraordinary

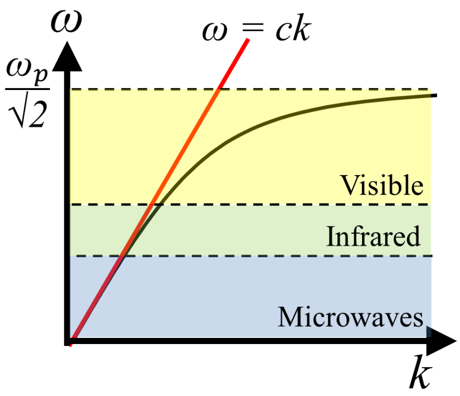

Figure 2.9: Sketched dispersion plot illustrating the nature of a surface mode as a function of angular frequency $\omega$ and in–plane momentum $k$, parallel to the interface at which the surface wave propagated.

transmission and attributed it to long distance in phase scattering from a periodic array of elements. This can be viewed as surface wave mediated transmission.

**Frequency Selective Surface** a periodic arrays of elements whose response to incident radiation varies with frequency. Predominately used as filters to transmit, reflect, or absorb at different frequencies [1].

Structures have been designed to exploit this diffraction and interference to produce EM fields that exhibit beaming and steering through surface patterning on PEC materials in the microwave regime. One example is the “bulls eye” structure that also illustrates the role of a regular structure to enhance the transmission. Here a single subwavelength hole (as in Bethe’s works [4]) is surrounded by a series of concentric circular grooves placed an equal distance apart. By coupling the incident radiation into surface waves on one or both structured interfaces, the EM fields at the hole are enhanced, then tunnelling through the hole and subsequent coupling of the upper and lower SP modes, dramatically enhances the transmission. The re-scattering from the concentric grooves on the lower surface can produce a directed beam but with or without the lower grooves the transmission may be many orders of magnitude greater than for the hole alone [50–52].

## 2.4 Microwave Response When the Incident Wavelength is Much Larger than the Hole Size

In the previous discussion transmission through a metallic mesh or hole array was considered when the incident radiation frequency was close to the diffraction edge. Here by structuring on a subwavelength scale the metallic mesh becomes a "plasmonic metamaterial". There is no agreed definition of a "metamaterial" [53], however here the definition below is used:

**Metamaterial** an arrangement of artificial subwavelength structural elements, designed to achieve advantageous and unusual electromagnetic properties.

There is much debate as to whether artificially engineered structures such as FSSs and Photonic Crystals (defined below) fit into this category. Traditionally both are created using constituent elements on the order of the wavelengths and therefore shall be excluded from this section of the discussion.

**Photonic Crystal** Multiple layers of alternative refractive index dielectric, that when illuminated with radiation of the order of the optical thickness of the layers responds with a series of highly transmitting and highly reflecting regions as a function of frequency. The spectral position of the transmission and reflection bands is entirely dependent upon the optical thickness of the layers [54].

### 2.4.1 Subwavelength Structuring of PEC Metals

Texturing a flat PEC surface with a subwavelength structure leads to the incident radiation experiencing an effective permittivity and effective permeability, these may be controlled almost independently by the choice of geometry of the subwavelength inclusions of the structure [55, 56]. When using holes below the cut–off frequency of the first supported waveguide mode, the transmission through a subwavelength hole is evanescent. Therefore a metallic mesh of subwavelength holes acts as an array of cut–off waveguides, where the transmission is dependent on the rate of evanescent decay.

#### 2.4.1.1 The Metallic Mesh as a Plasmonic Metal Analogy

Pendry *et al.* first considered a subwavelength square array of square holes as a metamaterial in 2004 [55]. Pendry and co-workers suggested the dielectric function of a subwavelength hole array is analogous to that of the Drude model used for plasmonic metals as discussed in section 2.3.1. By matching the **E** and **H** fields of the lowest order (cut–off) waveguide mode ($TE_{10}$ EM field profiles shown in Figure 2.2) in each subwavelength hole to the incident fields at the interface, the permittivity and permeability were found as a function of frequency, and from there the asymptotic limit for the dispersion of a bound surface mode as shown in Figure 2.9. This limit is identical to the form of the waveguide cut–off frequency of the hole (as shown in Equation 2.43 [55, 57]). This surface wave supported at the asymptotic limit in this and subsequent modelled works [14, 58] has become known as the "spoof surface plasmon".

The penetration depth of the EM fields into the media surrounding at the interface with a subwavelength hole array ($\delta_A$) and into the subwavelength holes of the metallic mesh ($\delta_{HA}$) can also be found using the general form for the penetration depth, Equation 2.64.

$$\delta_m = \frac{1}{2k_z} = \left(2 \times [\varepsilon_m k_0^2 - k_x^2]^{\frac{1}{2}}\right)^{-1}. \tag{2.64}$$

The EM fields in the surrounding media are only dependent on the evanescent diffracted orders determined by the pitch, $d$. Due to the subwavelength nature of the hole array being considered, only the first diffracted order, that occurs at $f = \frac{c}{d}$ will be considered, as this diffracted order will dominate the response. So the wave vector parallel to the interface becomes $k_x = \frac{2\pi}{d}$, and the permittivity of the medium $\varepsilon_m$ becomes the permittivity of air, represented for a general case by $\varepsilon_A$. Hence the penetration depth is described by Equation 2.65:

$$\delta_A = \left(2 \times \left[\varepsilon_A \left(\frac{\omega}{c}\right)^2 - \left(\frac{2\pi}{d}\right)^2\right]^{\frac{1}{2}}\right)^{-1}. \tag{2.65}$$

The penetration depth of the EM fields into the subwavelength PEC hole array are only dependent on the proximity to the cut–off frequency that is determined by the size of the holes, $a$. Inside each hole the EM fields are bounded by the metallic walls, and are therefore quantised. As the holes are cut off the first order waveguide mode will not propagate but will dominate the evanescent response so the wave vector inside the holes is $k_x = \frac{2\pi}{2a}$. The permittivity of the media, is now the dielectric filling the hole, here again this is considered as air ($\varepsilon_A$). So the penetration depth of the EM fields into the hole array is described by 2.66:

$$\delta_{HA} = \left(2 \times \left[\varepsilon_A \left(\frac{\omega}{c}\right)^2 - \left(\frac{\pi}{a}\right)^2\right]^{\frac{1}{2}}\right)^{-1}. \tag{2.66}$$

This is only valid when $d << \lambda_{inc}$. The penetration depth for air is shown in Figure 2.10 (a) and the effective penetration depth for the hole array is shown in Figure 2.10 (b) as a function of incident wavelength where the hole size and pitch of the hole

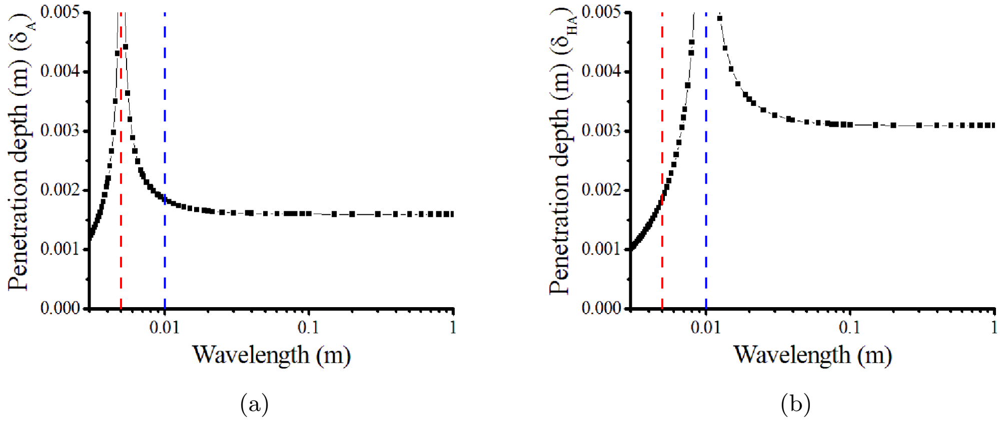

(a)

(b)

Figure 2.10: The effective penetration depth into (a) the surrounding media and (b) the subwavelength holes of the metallic mesh with pitch $d = 5$ mm, and hole size $a = 4.85$ mm. The red dashed line indicates the onset of diffraction, and the blue dashed line indicates the highest experimental frequency recorded for samples using this structure.

array are 4.85 mm and 5 mm respectively. Considering the highest frequency at which experimental data is recorded for structures using this metallic mesh pitch (30 GHz), the decay length (describing the amplitude of the EM fields) is $2 \times \delta_A \approx \frac{\lambda}{5}$, therefore the surface waves are not tightly bound to the interface in this region.

### 2.4.2 Enhanced Transmission Using Subwavelength Structured PEC Metals

Using structures such as slits, grooves or holes to enhance transmission on PEC metal was subsequently used to study enhanced transmission at microwave frequencies close to the onset of diffraction for structured PEC metals in the microwave regime.

The binding of a surface wave to a metallic structure in the microwave regime can be achieved by designing the surface geometry to mimic the response of a plasmonic metal. As described in section 2.3.1 the real part of the wave vector parallel to the interface must be real, leading to a negative effective permittivity of the metamaterial $\varepsilon_{2eff} < 0$, and the imaginary part of the wave vector perpendicular to the interface must be imaginary, so the magnitude of the effective permittivity (for the metamaterial) must be greater than that of the dielectric $|\varepsilon_{2eff}| > \varepsilon_1$. When these conditions are met a surface wave or spoof surface plasmon can propagate at the interface. But to be able to couple energy into this momentum of the incident wave must be enhanced as $k_{sw} > k_0$. This has been performed using grating and prism coupling and was first experimentally observed in 2005 by Hibbins *et al.* [59–61].

### 2.4.3 Transmission in the Subwavelength Regime

Being able to engineer the EM properties of a metamaterial such as a metallic mesh, to replicate the response of a plasmonic metal means structures that previously were not easy to investigate in the microwave regime due to the high conductivity of metal, can now be formed from metamaterials, allowing 'optical' experiments to be replicated at longer wavelengths in the microwave regime. One example of such a system used throughout this thesis is the simple Fabry–Pérot resonator. Formed of two highly reflecting metal mirrors, separated by distance $t_d$, this system supports transmission resonances, where each mode is defined by a quantisation between the mirrors at frequencies given approximately by Equation 2.67.

$$f_{FP} = \frac{c\, m}{2nt_d \cos\theta}, \tag{2.67}$$

where $c$ is the speed of light, $m$ is an integer, $n$ is the refractive index of the medium between the mirrors, and $\theta$ is the angle of incident radiation.

Originally studied in the optical regime the system requires two slightly transmitting metal mirrors. To function at microwave frequencies the mirrors would have to be $< 1$ µm thick. Whereas, by using a metallic mesh mirror, the mirror can be much thicker (on the order of millimeters) and the Finesse of the mirrors (defined as $\mathfrak{F} = \pi\sqrt{R}/(1-R)$ where R is the reflectivity of the mirror) can be tuned through a suitable choice of hole, pitch and thickness. Using a PEC metallic mesh also excludes any loss in the metallic region of the system, something that is not possible in the optical regime, meaning almost idealised systems can also be investigated. These systems are almost ideal because even at microwave frequency metals are not actually perfect conductors.

In this thesis the metallic mesh structures can be considered as plasmonic metamaterials, but with negligible loss. However, as these investigations are considered in the subwavelength regime, far from the onset of diffraction, the resonant transmission does not rely on the transmission mediated by the excitation of surfaces waves, spoof or otherwise. Although surface waves exist on the interfaces of the metallic meshes indicated by the penetration depth of the evanescent decay of the EM fields shown in Figure 2.10. The momentum requirement to couple to these surface waves is not satisfied. So the transmission observed occurs due to resonant tunnelling of the EM fields within the subwavelength holes, as will be shown throughout this thesis.

### 2.4.4 Metamaterials

This thesis only considers metamaterials in the form of metallic meshes (hole arrays) and metallic patch arrays. However there are many other forms of metamaterials. Many in the field of metamaterial research believe it was largely driven by four seminal papers many decades apart [62].

First in 1968, Veselago predicted simultaneous negative permittivity and negative permeability, leading to a negative refractive index. He claimed that radiation from a point source could be focused on the other side of a slab of negative index material [63].

The second was the experimental realisation of this negative index artificial material in 2000 by Smith *et al.* [64]. Here split ring resonators (SRRs) (introduced by Pendry *et al.* [65]) produced negative permeability. An array of SRRs was combined with an array of continuous wires which produce a negative permittivity below the cut–off frequency associated with the slits between the wires acting as waveguides [66]. By investigating the response of the structure in regions where only the permittivity or the permeability was negative, no transmission was recorded. However when both the permittivity and permeability were negative Smith *et al.* observed a clear band of frequencies where transmission occurred.

The third seminal paper followed the next year when Shelby *et al.* experimentally demonstrated negative refraction using the same combination of SRRs and continuous wires [67]. Here the structure was arranged into a prism, and a detector varied in incident angle to measure the angle of refraction. The negative index material exhibited refraction on the opposite side of the normal to the boundary when compared to positive index materials. The effective refractive index was also found using Snell's law.

The final paper that started the search for more exotic materials was the "perfect lens" [68]. Here it was theoretically shown that by using a slab of negative refractive index material the traditional classical diffraction limit of a lens could be broken, as the evanescent waves may be transmitted without loss, recreating a perfect image of the object.

From this point the research area grew covering artificial magnetism [69], high refractive index [70], cloaking [71–76], negative refractive index due to chirality (see Chapter 8) and for many more areas see [53, 77–79].

## 2.5 Concluding Remarks

As an introduction to the recent experimental results reported in this thesis, this chapter provides an overview of the advancement of understanding on the mechanisms by which metallic meshes or hole arrays transmit EM radiation. This began by considering each hole in the array as an isolated waveguide, and the quantisation of the modes that allow propagation described. Then by considering the regime where the incident radiation is of the order of the pitch of the structure, but the holes are subwavelength, transmission mediated by surface waves and enhanced optical transmission (or extraordinary transmission) was discussed. The last section discussed the subwavelength structure and advancements in metamaterial research stating that in the subwavelength regime surface waves are not bound to the metallic mesh below the cut–off frequency associated with the holes and the onset of diffraction. Therefore it is tunnelling alone that is responsible for the transmission and reflection responses recorded in the experimental results shown in Chapters 5, 6, 7, and 8.

# Chapter 3

# Techniques Used to Simulate Electromagnetic Responses of Mesh Metamaterials

## 3.1 Introduction

In this chapter the simulation methods used in this thesis are discussed. First a comparison is made between the modelling techniques: Finite Difference Time Domain (FDTD), Moment of Methods (MoM) and Finite Element Method (FEM). Followed by a discussion of FEM modelling with specific relevance to the problems studied in this work. A brief overview is given on LCR circuit theory and modal matching techniques that have been used by others authors in this field, but not by the author.

## 3.2 Comparison of FDTD, MoM, and FEM Modelling Techniques

A brief description of three full wave modelling and simulation techniques is presented, considering the strengths and weaknesses of each. The modelling techniques discussed are FDTD, MoM and FEM; each solves Maxwell's equations by applying different assumptions to simplify the modelled system.

### 3.2.1 Finite Difference Time Domain (FDTD)

FDTD is a volume based solver. The programme creates a 2D or 3D grid and solves the differential form of Maxwell's equations in the time domain (also known as the Central Difference Equations). The grid is usually rectangular, where each section is of a fixed size, comparable to the shortest wavelength in the range of interest. The EM fields propagate through the domains of the grid calculating the EM fields for the lowest frequency in the range of interest, a Fourier Transform is performed to give a broad band frequency response. The FDTD technique is best employed for enclosed volumes (of metallic and dielectric objects) and for investigating scatter in non-uniform media, due to the regular grid over that quantities are calculated. The volume based grid that segments the model means that the time taken to reach a solution is dependent on the size of each domain and the size of the overall model, and therefore model size should be kept as small as possible [80, 81].

### 3.2.2 Method of Moments (MoM)

The MoM technique solves a set of linear equations for the surface currents on predominantly air and metallic surface. Dielectric materials require more complex equations to describe surface currents and are not generally considered using this technique. The structure is divided into electrically small (compared to the operating wavelength) elements taking the form of wire segments or patches. The current amplitude is assumed to be constant over each element. The electric field is calculated for each frequency by performing a vector sum of the surface currents. This technique is generally used for long thin structures (such as wires), and structures where large distances must be modelled, such as antenna arrays [80, 82].

### 3.2.3 Finite Element Modelling (FEM)

The Finite Element Method (FEM) is a numerical modelling process that divides 2D or 3D space into smaller polyhedral (usually tetrahedral) shaped regions, referred to as the tetrahedral mesh as shown in Figure 3.1. FEM software packages use adaptive tetrahedral meshing to add more tetrahedra at points of interest, i.e. where the vector quantity being calculated varies most rapidly, allowing the tetrahedra size to vary over the model. This allows large aspect ratios to be considered in a single model. The software then forms a matrix by considering the nodes at the vertices or mid-points of each tetrahedron depending on whether the quantity being calculated acts tangential to the edges or normal to the edges (tangential to face) respectively. The EM field inside the tetrahedra is assumed to be constant and is interpolated from the nodes at the vertices and mid-points.

In this thesis the EM response of the subwavelength mesh based structures is modelled using Ansoft's HFSS [83], a FEM based software package. However similar FEM packages exist in this and other fields of research such as structural engineering, thermodynamics, fluid dynamics, mechanical systems and many more, to perform simulated

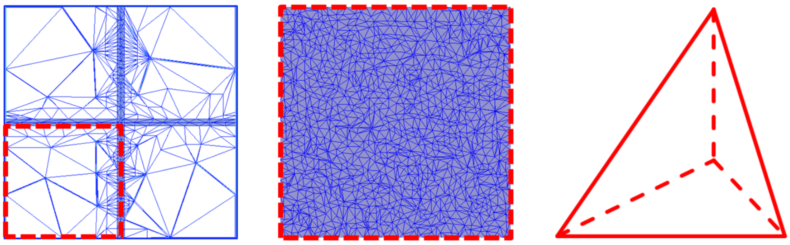
(a) (b) (c)

Figure 3.1: (a) cross section in the $xy$ plane showing initial tetrahedral mesh for one layer of metallic mesh unit cell, (b) red dotted area of subwavelength hole enlarged for final tetrahedral mesh, (c) red pyramidal tetrahedral element.

product development for projects such as stress and strain testing of gearing, temperature dependence of exhaust systems, and turbulent flow in hydraulic systems.

## 3.3 Ansoft's HFSS

Ansoft's High Frequency Structure Simulator (referred to as HFSS) [83], was originally intended for waveguide design and development, although now it considers a much larger range of problems. In order to analyse a system, the smallest possible 3D section is constructed using an integrated Computer Aided Design (CAD) interface. This is then divided using the tetrahedral mesh, within which the vector field quantities are calculated. As will be shown throughout this thesis, the choice of modelled structure is very important. All the structures considered here are formed of repeat periods infinite in the $xy$-plane normal to the incident microwave beam (propagating in the $z$ direction), represented by a single unit cell with repeat boundary conditions. This repeat unit cell is important when considering the complexity of the system compared to the finite computational power available.

### 3.3.1 CAD Modelling Tools

The integrated CAD package allows HFSS users to accurately represent the sample to be investigated as a 3D model. One, two and three dimensional simple objects such as points, lines, rectangular and oval sheets, as well as polyhedra, may be drawn and then operated on to build more complex structures. For example, the square metal mesh with square air–filled holes, considered throughout this thesis, is constructed from two united cuboids aligned to cross in the centre of a vacuum box representing a single unit cell and its surrounding media (air) see Figure 3.2. Other operations

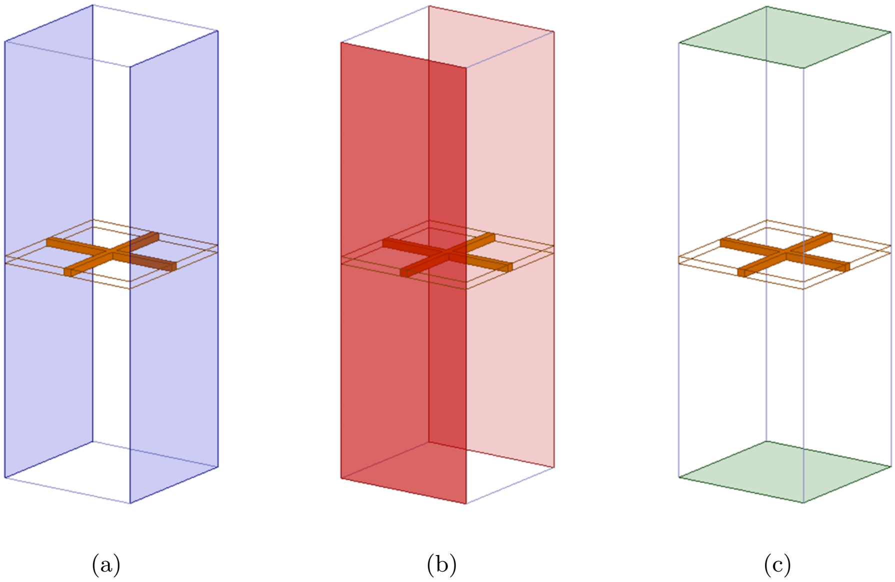
(a) (b) (c)

Figure 3.2: Simplified CAD model of the unit cell used to model a single metallic mesh. A metallic cross is placed at the centre of an air box. Highlighted faces shown the position of: (a) the first pair of master–slave boundary conditions, (b) the second pair of master–slave boundary conditions, and (c) the Floquet ports.

include subtract, rotate and duplicate along a line, all of which are used in the rotated arrays detailed in section 8.4.1, as well as mirror and intersect. All variables may also be assigned parameters (a variable name) either directly when drawing the objects or retrospectively. Parameters may be independent, or dependent upon one another, which allows for easy scaling of the structure. Parameters may also use conditional statements such as “IF” and “OR”.

### 3.3.2 Assigning Materials

HFSS hosts a large library of commercially available materials (dielectrics and metals) commonly used in the radio frequency and microwave regimes. Materials are allocated five parameters to describe their EM response; the relative permittivity ($\varepsilon = \varepsilon' + \varepsilon''$), the relative permeability ($\mu = \mu' + \mu''$), the dielectric loss tangent ($\tan\delta = \frac{\varepsilon''}{\varepsilon'}$), the magnetic loss tangent ($\tan\delta_{\mu} = \frac{\mu''}{\mu'}$), and the bulk conductivity ($\nabla \times (-1/j\omega\mu) = ((j\omega + \sigma)E)$) where $\omega$ is the angular frequency, $\sigma$ is the conductivity, and $E$ is the electric field. When allotting material parameters only two values are stated; for dielectrics these are the relative permittivity and dielectric loss tangent, and for metals these values are the relative permittivity and the conductivity. From these values the other three parameters can be calculated. User–defined materials may be added, allowing either fixed or frequency dependent values (interpolated between user specified points) as used in Chapters 5 and 6.

Real metals such as copper and aluminium are assumed to be perfectly electrically conducting (PEC) within the microwave frequency regime (see Figure 2.7). Real metals at these frequencies posses a large permittivity (negative real part $\sim 10^4$ and positive imaginary part $\sim 10^8$). When the metal thickness is greater than the skin depth (as defined in Equation 2.63), a surface boundary condition is applied, yielding a finite conductance. When the thickness of the metal is comparable to the skin depth, HFSS applies a conductivity boundary condition in the form of a layered impedance (see [84] 15-61).

### 3.3.3 Assigning Boundary Conditions

There are many boundary conditions that HFSS offers to the user such as perfect E, and perfect H symmetry planes that can be inserted into the model when the electric or magnetic field is perpendicular to the applied boundary respectively. This boundary does not translate or mirror incident field but replicates the EM response of the structure. The Absorbing Boundary Condition (ABC) can be applied to any surface but must be at least $\lambda/4$ from strongly radiating structures. This boundary is most effective when used at normal incidence, see Figure 3.3(a), but fails at higher angles of incidence as in Figure 3.3(c) due to the second order polynomial used to calculate the response of free space, this becomes inaccurate at high angles of incidence. Perfectly Matched Layers (PMLs) are another type of radiation absorbing boundary condition applied to the outer boundaries of the structure or surrounding media that create lossy anisotropic boxes perpendicular to the selected boundary. This boundary absorbs for incident angles of up to 70° as shown in Figures 3.3(b) and 3.3(d) due to the use of material tensors to calculate the response of at the boundary ([84] 15-58, Figure recreated from [85]).

In this thesis only one boundary condition is used, the master–slave (MS) boundary. This is a repeat boundary condition used to model periodic structures that are infinite (relative to the incident beam), in up to two dimensions, as a single unit cell. The master and slave conditions must be applied as a pair of boundaries, see Figures 3.2(a) and (b). The EM fields incident at the master boundary are applied at the slave boundary and must match in magnitude and direction (or opposite direction), implying identical tetrahedral meshes on the two faces. Large variation in the vector field near the boundary can cause errors unless the tetrahedral mesh is very dense. Therefore it is generally suggested that regions where large field gradients are expected, are placed away from the boundaries of the model. In this thesis two pairs of master–slave bound-

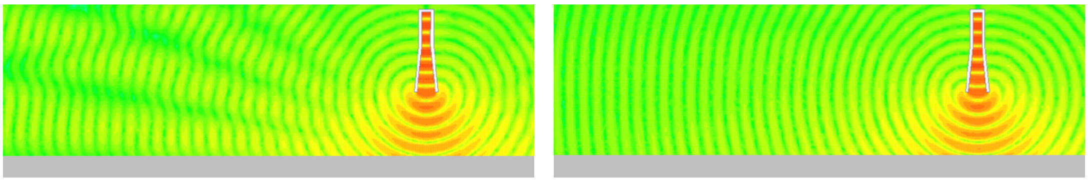

(a) ABC at $\theta = 0°$ (b) PML at $\theta = 0°$

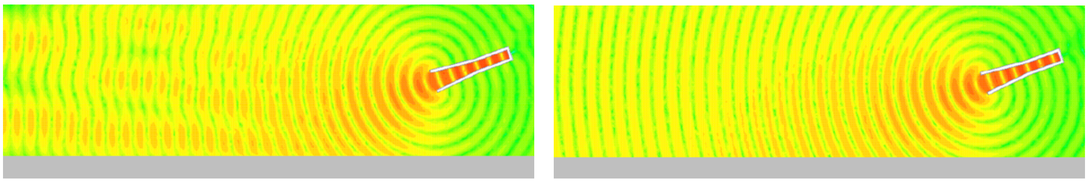

(c) ABC at $\theta = 70°$ (d) PML at $\theta = 70°$

Figure 3.3: HFSS electric field profile taken in the $xz$–plane showing the wave front emanating from a crudely modelled waveguide horn formed of PEC metal pates, changing the lower horizontal boundary condition and the incident angle theta. Recreated from Ansoft literature.

ary conditions are used as the arrays repeat in the $xy$-plane. However, any number of parallel faces can be used allowing the replication the response of any array with a tessellating unit cell.

### 3.3.4 Excitation Sources

There are many radiation sources that can be used to excite a structure: from lumped ports, used extensively to power antenna designs, to wave ports used to excite waveguide systems such as couplers and adaptors.

In preliminary modelling an incident plane wave defined either by Cartesian or spherical coordinates was used to illuminate the modelled structure. This required absorbing boundaries (ABCs or PMLs depending on angle of incidence) to be applied to all the outer faces of the model to avoid erroneous reflections as shown in Figure 3.3. This excitation method also requires a way of extracting the reflection and transmission properties of the structure. This is done using a macro script (written in Visual Basic) that calculates the transmission and reflection in the vacuum space above and below the structure by integrating over two planes (placed above and below the structure).

In this thesis only one method of excitation and detection is used, a Floquet port [86]. A set of modes are used to represent the EM fields on the port that resemble waveguide modes (as discussed in section 2.2), producing plane waves that are characterised by frequency, phase and the geometry of the port. With ports placed on the incident and exit faces of a model as shown in Figure 3.2 ($c$), radiation boundaries are not required. Both ports are defined by unit vectors that dictate the direction of the electric field of the modes. Both ports also facilitate the direct extraction of the reflection and transmission coefficients from the scattering matrix without the use of a script.

Floquet ports can only be used on the unit cell of periodic structures surrounded by master slave boundaries to allow for the periodic decomposition of the excited and detected modes that can be viewed individually. In this work floquet ports were used well below the onset of diffraction, therefore the $TE_{01}$ and $TM_{01}$ modes (shown in Figure 2.2 and 2.3) dominate the form of the EM response. In Chapter 8 the ability to emit radiation in one linear polarisation state and detect the orthogonal linear polarisation state is used to measure the polarisation conversion.

### 3.3.5 Tetrahedral Mesh

In order to achieve a realistic EM response from a modelled structure, the model must be split into smaller elements to be solved, as implied by the name finite element method. HFSS does this by creating an initial tetrahedral mesh, and then refining it. Here the various stages of this process will be briefly explained with relevance to the modelling undertaken in this thesis.

The initial tetrahedral mesh splits the CAD 3D model into smaller components depending on the size, geometry, and refractive index of the objects. For example, less tetrahedra will be placed in a large air space, as there is little change in the EM field character in this volume, and the density will increase when approaching the boundary with an object of dissimilar media. Then the "surface approximation" is applied, here curved "true" surfaces must be represented by faceted surfaces.

Once the initial tetrahedral mesh is defined, a series of refinements occur, some of which can be omitted. The first to be considered is the "Lambda refinement", that reduces the size of the tetrahedral elements (increasing density) with respect to the solution wavelength $\lambda_s$ according to the wavelength dependence of the material (zero order $\approx$ $0.1\ \lambda_s$, first order (default) $\approx$ $0.\dot{3}\ \lambda_s$, second order $\approx$ $0.667\ \lambda_s$).

"Mesh operations" can be applied to the tetrahedral mesh at any stage after the initial tetrahedral mesh is formed. These user–defined operations allow the user to apply prior knowledge and identify regions within the 3D model that are crucial to re-create the experimentally observed response. These may be applied to a 2D sheet or 3D volumes, and allow the user to specify the target side length of each tetrahedral element, but also limit the number used in an area or volume. As used to increase the density of the tetrahedra in the subwavelength holes of the metallic mesh to accurately represent the decay of the EM fields. This could dramatically reduce the number of tetrahedra input into the model by the adaptive pass process, discussed below, saving computational power, and time.

### 3.3.6 Solution and Adaptive Meshing

When the initial tetrahedral mesh is formed the accuracy of the solution is calculated at each port for verification. This is done by computing the electric field from the magnetic field using: $\nabla \times \mathbf{E} = -j\omega\mu\mathbf{H}$ and comparing this value with the incident value. The same is done for the magnetic field using $\nabla \times \mathbf{H} = \sigma\mathbf{E} + j\omega\mathbf{E}$. When these values are comparable the full 3D solution begins. As described earlier the tetrahedral mesh has nodes at each vertex and mid-point, a matrix stores the tangential and normal EM field components for each vertex and mid-point node respectively. It is the order of the solution that determines how many nodes are used per tetrahedron; zero order uses 4 nodes to calculate 8 unknowns (vertices only); first order (default) uses 10 nodes to calculate 20 unknowns, and second order 22 nodes to calculate 44 unknowns.

The 3D field solver transforms Maxwell's equations into matrix form and numerically calculates values for each unknown, interpolating the results within the volume of each tetrahedral element using the equation $\nabla \times (\frac{1}{\mu'}\nabla \times \mathbf{E}(x,y,z) - k_0^2\varepsilon'\mathbf{E}(x,y,z)) = 0$ (where $k_0 = \frac{2\pi}{\lambda}$ is the incident wave vector). From this the reflection and transmission coefficients can be calculated and the normalised power is found. This is expressed in the form of a scattering or S–matrix, where each element describes the modes being excited and detected at a specific port.

After this, adaptive passes may be used to further refine the tetrahedral mesh. Here HFSS considers the field gradient in each of the tetrahedral elements and inserts more tetrahedra where the gradient is highest, recalculates the scattering matrix and records the $\Delta S$ value. The $\Delta S$ value is the root mean square of the scattering matrix which measures the change in the magnitude of the scattering matrix between adaptive passes allowing the user to gauge if the tetrahedral mesh is converging on a solution. This process will cease when the user–defined limits are reached being either the maximum number of adaptive passes or $\Delta S$ becoming less than the user–defined target.

A frequency sweep can be used to calculate the response for a range of frequencies. Using the tetrahedral mesh optimised for the single solution frequency, the frequency sweep is only valid over a limited range. In this thesis (and suggested as good practice) the frequency ranges of the commercial waveguide bands, shown in table 4.1 are used as a guide to the span of a frequency sweep, where the solution frequency is placed above the centre of the frequency sweep to ensure validity at the smaller incident wavelengths.

#### 3.3.6.1 Tetrahedral Mesh Accuracy

In order to create a FEM model that accurately represents the response of the physical system the size of the tetrahedral element must reflect the changing EM field within that region. Generally, the larger the number of tetrahedra in the model, the finer the tetrahedral mesh, and the higher the accuracy. However the finer the tetrahedral mesh the more computationally expensive the model is to run, and so more time is required to reach a solution. Therefore it is clear that a balance is required. By comparing reduced frequency resolution spectra for a series of adaptive passes, the point at which the solution converges can be accurately predicted where the response is invariant as more tetrahedra are added to the model. This can be used as an alternative to monitoring the $\Delta S$ value that is only calculated at a single frequency.

### 3.3.7 Post Processing

After the analysis of the model has been performed and a solution calculated, post processing can take place. Firstly reports can be generated from user–defined expressions using the scattering data, or directly from the **E** and **H** fields. The main data extracted from these models is the transmission and reflection intensity coefficients as a function of frequency. This can be done using expressions 3.1 and 3.2 respectively:

$$T = (mag(S(FloquetPort1 : 1, FloquetPort2 : 1)))^2, \tag{3.1}$$

$$R = (mag(S(FloquetPort1 : 1, FloquetPort1 : 1)))^2, \tag{3.2}$$

where $FloquetPortA : B$ corresponds to Floquet port A, mode B. Here the wave is incident at Floquet Port 1, and detected at Floquet port 2 for transmission and Floquet port 1 for reflection. Mode B is the corresponding Floquet port mode being used, the first modes being $TE_{10}$ and the second $TM_{10}$. The $S$ preceding the floquet ports numbers indicates that it is the scattering matrix element.

By comparing the transmission and/or reflection response to that of the experimentally observed data, the model can be validated. The second main post processing element of the HFSS software allows the user to gain physical insight into the distribution of the **E** and **H** fields (and other quantities). The magnitude or vector fields can be graphically represented, for an example see the waveguide mode Figures 2.2 and 2.3. Incident, total or scattered (difference between the total and scattered fields) can be plotted over a plane or inside a volume and then animated in frequency, phase or any other user–defined variable of the model. These can be seen throughout this thesis. User–defined expressions can be formed of complex field quantities using the field calculator and applied to reports, as utilised in Figures 5.5, 6.4, and 7.5.

## 3.4 Thesis Specific Modelling

This thesis discusses a series of square metallic meshes with square holes that occupy $> 80\%$ of the unit cell, all of which are illuminated with radiation where the wavelength is much greater than the pitch and hole size, making the metallic mesh subwavelength. Therefore the EM fields within these holes decay evanescently from the interfaces with the surrounding media. In this thesis numerical modelling is used to gain insight into the origin and operation of modes and the transmission and reflection response of a system. Here the stacked metallic mesh–dielectric structure considered in Chapter 6 will be used to illustrate the problems encountered whilst modelling the response of this structure.

In order to accurately represent the very thin metallic mesh, the FEM model has undergone a series of iterations described below. Initially the unit cell was chosen with the hole placed in the centre surrounded by half the width of the metallic bars (between holes). The hole filling–fraction for the metallic mesh is 97% air, leaving large field gradients in close proximity to the boundaries of the structure. This configuration of a large hole surrounded by a narrow metallic bar led to a large number of tetrahedra in the region close master–slave boundary. In many cases the tetrahedral meshes on the faces of the master–slave boundaries were not identical, hence the model would not satisfy the repeat boundary condition and failed to solve. Therefore a new unit cell was chosen placing the edges of the subwavelength holes at the centre of the unit cell, forming a cross of metal in the centre of the unit cell. The frequency spectrum for this metallic mesh–dielectric stack initial model is shown in Figure 3.4 (blue line), and the modes are $\sim 1.5$ GHz higher in frequency than the experimentally observed results (black circles). Using measured frequency dependent permittivity and dielectric loss tangents of the dielectric reduced this to 0.5 GHz for high frequencies and $\sim 1.5$ GHz for low frequencies, Figure 3.4 (green line). From here the tetrahedral mesh of the FEM model was refined by increasing the resolution to better represent the evanescent decay of the EM fields within the holes. Firstly this was done by introducing more tetrahedral elements using a mesh operation. Then it was further refined by physically splitting the boxes of air (filling the holes) into a $5 \times 5$ array in the $xy$-plane, and crucially 10 layers in the $z$-direction (propagation and decay direction). Once the evanescent decay of the EM field inside the subwavelength holes was properly represented, adaptive passes where performed until convergence was achieved. From this the fit to the experimental data shown in Figure 3.4 (red line) was achieved.

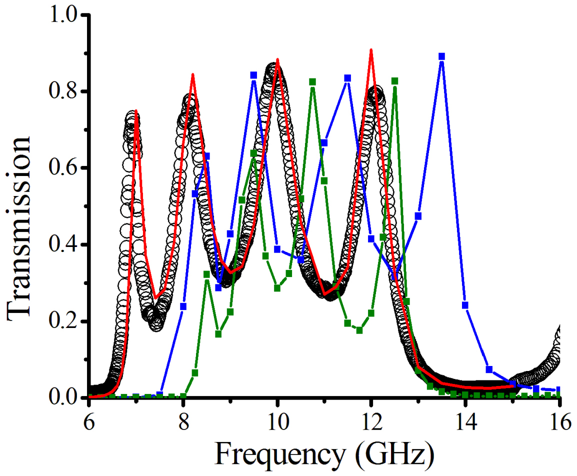

Figure 3.4: Transmission response for the metallic mesh–dielectric stack considered in Chapter 6, black circles represent the experimentally recorded data, the blue, green and red lines represent the response from the initial tetrahedral mesh, using experimentally measured permittivity results and using tetrahedral mesh operations and division of air spaces.

## 3.5 Comparison with LCR Circuits

Simple mesh based structures such as those considered in Chapters 5, 6, and 7 comprising alternating metal grids and dielectric regions can be represented using circuit theory models. A direct comparison between the work considered in Chapter 6 is presented in [87] where the experimental and numerical results are compared to a series of parallel plate waveguides, both dielectric and air–filled, separated by “diaphragm discontinuities”. Using only the propagation constant (wave vector), and characteristic impedance ($Z_0 = \sqrt{\frac{\mu}{\varepsilon}}$) for air and dielectric filled regions and an expression for the impedance of the grating (dominated by the inductance) good comparison is shown. An equivalent circuit is considered by splitting the structure into electrically small elements and considering the EM coupling and phase delay as inductive (L), capacitive (C) and resistive (R) components. This method is restricted to certain geometries. Features that occur in the experimental sample such as rounding of square holes and filleting of deposited or etched metals cannot be replicated. Certain structures such as the rotated array considered in Chapter 8 using FEM cannot be modelled using LCR circuit theory. But the main advantage of this process over FEM modelling is the fraction of the computing power required to calculate the transmission response, allowing the user to gain physical insight into the dependence of the response on parameters such as repeat pitch, hole size etc. for all frequencies (to DC) where the components are considered to be electrically small and so is similar to the MoM techniques described earlier.

## 3.6 Modal Expansion

Further analytical modelling has also been performed on the simple metallic mesh structures using analytical modal expansion of the **E** and **H** fields matched over various regions of the structure. Taylor *et al.* have extensively studied subwavelength hole arrays using a modal matching technique [88, 89]. The modal matching method is described below for an infinite array of subwavelength square holes in a thin PEC.

- Express the electric fields in the vacuum regions above and below the hole array as 2D Fourier-Floquet expansions of the diffracted orders.
- Within the metallic hole array the electric fields are present only in the holes, where they can be described as cavity modes.
- The magnetic fields are then calculated for each region using Maxwell's equations.
- The tangential boundary conditions imposed are: the electric field must be continuous at each interface across the entire unit cell, whilst the magnetic field must be continuous across the aperture.
- Applying these boundary conditions and utilising the orthogonality condition of the eigen modes resulting in pairs of coupled equations in terms of the unknown amplitude coefficients.
- Solve these equations to obtain the analytical expressions for the transmission and reflection through the structure.

Taylor and others [55–57, 89] consider only the first order cavity mode, as it is a good approximation for the regime where the pitch and hole size are subwavelength. Again this method is restricted by the geometry of the hole array, but it is much faster than using the FEM modelling technique.

## 3.7 Concluding Remarks

In this chapter simulation of the EM response of mesh based metamaterial structures has been considered, with the focus dedicated to FEM modelling. Specific attention was paid to effective FEM modelling of the metallic mesh as it forms the basis of this thesis. FDTD, MoM, LCR circuit theory and modal matching techniques were briefly discussed as an alternative to FEM.

# Chapter 4

# Techniques Used to Measure Electromagnetic Responses of Mesh Metamaterials

## 4.1 Introduction

In order to conduct experimental investigations into the transmission and reflection properties of the structures investigated in this thesis, a system that produces a collimated plane wave of radiation is used. This experimental arrangement is described in this chapter. The first of two spherical mirrors with a waveguide horn antenna placed at its focus creates a beam of microwave radiation with near-planar wave fronts, that is directed onto the sample. The second mirror focuses the resultant beam (transmitted or reflected) into a second waveguide horn antenna where a crystal detector converts the microwave radiation into an electrical signal that can be interpreted by the analyser. This equipment is not housed in an anechoic chamber, but in a large laboratory surrounded by free space. The nearest reflecting boundaries are $> 50 \times \lambda$ from the equipment (for the longest operating wavelength, $\lambda$).

## 4.2 Apparatus

### 4.2.1 Waveguide Horns

The emitting waveguide horn is connected to a directional waveguide coupler that in turn is connected to a waveguide–coaxial adaptor and waveguide–crystal detector as shown in Figure 4.1 (a). Microwave radiation is fed through the first waveguide–coaxial adaptor by a combined source and sweep oscillator (*Agilent PSG CW Signal Generator*

| Frequency Band | WG | Minimum Frequency | Maximum Frequency |
|---|---|---|---|
| | 14$*$ | 5.38 GHz | 8.18 GHz |
| | 15 | 6.58 GHz | 10.00 GHz |
| X | 16$*$ | 8.20 GHz | 12.50 GHz |
| Ku | 17 | 9.84 GHz | 15.00 GHz |
| | 18$*$ | 11.90 GHz | 18.00 GHz |
| | 19 | 14.50 GHz | 22.00 GHz |
| K | 20$*$ | 17.60 GHz | 26.70 GHz |
| | 21 | 21.70 GHz | 33.00 GHz |
| Ka | 22$*$ | 26.40 GHz | 40.10 GHz |

Table 4.1: British waveguide bands spanning the range 5 – 40 GHz. *indicates these frequency ranges were used experimentally.

*E8247C*, 250 kHz $\leq \nu \leq$ 40 GHz), and the horn that emits the microwave signal. The upper frequency limit is fixed by the source at 40 GHz, however this may be extended to 112 GHz with external waveguide multipliers (such as *Agilent Millimeter Wave Source Modules, 83558A* and *83556A*). The frequency range is split into the European waveguide bands listed in the table 4.1 [90] and the apparatus described below (table 4.2) must be optimised for each waveguide band. The directional waveguide coupler removes a proportion of the microwave signal (10% of the transmitted radiation) and the waveguide–crystal detector transmits an electrical signal to the scalar network analyser (SNA) (*Agilent 8757D*) as a *reference* signal. The source, considered at the horn is approximated as a point source and placed at the focus of a spherical mirror, producing a near collimated plane wave.

The detecting waveguide horn is also connected to a waveguide–crystal detector, as shown in Figure 4.1(b). The microwave signal collected by the waveguide horn is converted into an electrical signal by the crystal detector and transmitted to the SNA as the *detected* signal.

The horns are rectangular in cross section, supporting an electric field vector parallel to the short axis, making the radiation emitted or detected linearly polarised and polarisation selective. Both the emitter and detector horns are housed in mounts that can be rotated in order to produce transverse electric (TE or s-polarised) or transverse magnetic (TM or p-polarised) beams with respect to the sample (see section 2.2.1.1). Although optimised for use within the stated frequency bands it is often found through careful investigation that the operational range can be extended, this is dependent upon the combination of components being used and varies for each item.

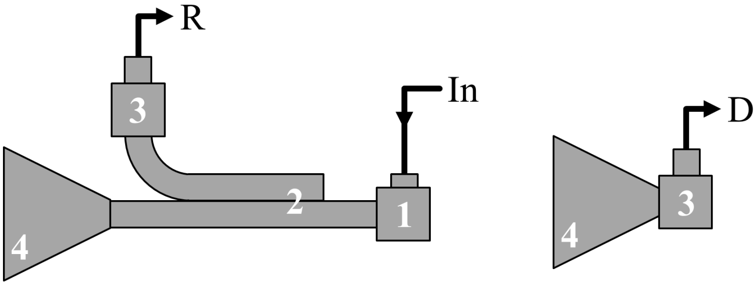

(a) (b)

Figure 4.1: Waveguide horn assembly for emitter (a) and detector (b). The numbered areas correspond to the waveguide components; (1) waveguide–coaxial adaptor, (2) directional coupler, (3) waveguide–coaxial adaptor with integrated crystal detector, known as a waveguide–crystal detector, and (4) the horn. The labels $In$, $R$, and $D$ correspond to the input signal from the source, the reference signal (output) and the detected signal (output).

| WG | Horn (Gain 16.5 dB) | Directional Coupler (10 dB) | Waveguide–coaxial adaptor | Waveguide–crystal detector |
|---|---|---|---|---|
| 14 | Narda 644 | x | HP J218A | HP J424C |
| 16 | Narda 640 | HP X752C | HP X218A | HP X424C |
| 18 | Narda 639 | HP P752C | HP P218A | HP P424C |
| 20 | Narda 638 | HP K752C | Flann 20093 TF30 | HP K424C |
| 22 | Narda 637 | HP R752C | Flann 22093 TF30 | HP R424C |

Table 4.2: Make and Model of the horn, directional coupler, waveguide–coaxial adaptor (without and with the integrated crystal detector), where HP denotes the manufacturer Hewlett Packard. Note: the WG14 emitting waveguide horn assembly does not use a directional coupler due to size restrictions.

### 4.2.2 Collimating Mirrors

The collimating mirrors are made in pairs and have a physical radius of 22 cm. They are formed by machining a spherical dish into thin cylindrical discs (4 cm thick). For more details see [91] pages $136-137$. A spherical shape was used for ease of fabrication, although a parabolic distribution would produce a more collimated beam due to the absence of spherical aberration. Two experimental arrangements are available: one using mirrors machined with a radius of curvature of 2 m to give a focal length of 1 m, (used in Chapters 6, 5, and 8), and another with mirrors of radius of curvature of 4 m, to give a focal length 2 m (used in Chapter 7). These mirrors are mounted on wooden frames that allow the mirrors to be adjusted in height, tilt and a small amount of twist. These frames are held in wooden parallel tracks for easier alignment. The same equipment can be reconfigured for transmission or reflection experiments.

### 4.2.3 Aperture

An aperture can be placed before the sample to reduce the beam width. This is constructed from a combination of square pyramidal and planar graded carbon loaded foam which is a good microwave absorber, that is arranged to form a hole of width less than the size of the sample. This is necessary when samples are smaller than or comparable to the size of the microwave beam spot to prevent direct transmission around the edges of the sample, and is normally used at low microwave frequencies due to the large wavelength compared to the finite size of the sample.

## 4.3 Experimental Arrangement for Transmission Measurements

A schematic of the experimental arrangement for transmission measurements is shown in Figure 4.2 (a). For transmission measurements the centre of the mirrors are placed at the same height as the centre of the sample that is orientated and fixed perpendicular to the wooden bench top on which the setup is placed. The sample may be mounted on a rotating table (driven by a computer controlled stepper motor) to change the incident angle $\theta$ (not considered here, but shown in Figure 4.2). However to change the azimuth angle $\phi$ the sample must be rotated by hand and secured in a holder. The waveguide horns are positioned at the focal point of the mirrors that are tilted such that the resultant microwave beam propagates parallel to the wooden bench through the absorbing aperture (if used) onto the sample. Ideally the horns would be placed at the same height as the mirrors however the size of the horns relative to the microwave

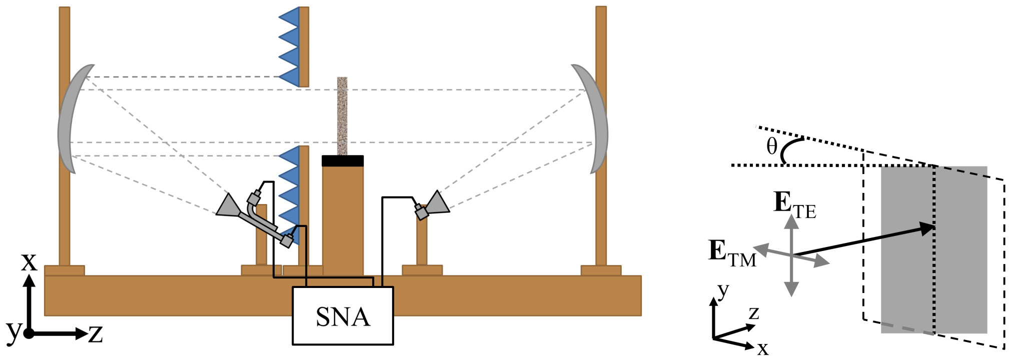

(a)

(b)

Figure 4.2: (a) Schematic showing the experimental arrangement for transmission at normal incidence using a planar or stacked sample where the emitter is on the left, and the detector on the right. (b) Diagram showing the direction of the electric field vector to define TE and TM polarised radiation when the sample is rotated by $\theta$.

beam width dictates that the horns must be moved off axis.

The proportion of the microwave beam that is transmitted through the sample is collected by a second spherical mirror that focuses the microwave beam into a second horn fitted with a waveguide–crystal detector that produces an electrical signal measured by the SNA.

When the sample is positioned normal to the incident beam the polarisation labels TE and TM polarised are degenerate. However, when the sample is rotated in $\theta$, the polarisation must be defined. This is shown in Figure 4.2 (b) where the electric field vector for TE and TM polarised radiation are orientated vertically ($y$ direction) and horizontally ($x$ direction) respectively, where the propagation direction is in $z$.

In Chapter 8 the polarisation conserved and polarisation converted transmission responses are investigated at normal incidence. As the TE and TM polarisation labels of the beam are degenerate at normal incidence, the orientation of the electric field vector is then defined in terms of $x$ and $y$. So the polarisation conserved transmission is denoted as $T_{xx}$ and $T_{yy}$ and the polarisation converted transmission denoted as $T_{xy}$ and $T_{yx}$. For all other normal incidence measurements the electric field was orientated in the $x$ direction unless otherwise stated.

## 4.4 Experimental Arrangement for Reflection Measurements

A schematic of the experimental arrangement for reflection measurements is shown in Figure 4.3 for small and large angles of incidence ($\theta$). Here the same apparatus used for the transmission measurements is repositioned and aligned to allow reflection measurements to be recorded. For reflection measurements the sample is placed parallel to the bench top. Placing a rotating table under the sample allows for variation in the azimuth angle $\phi$ (shown in Figure 4.3 (c)). The position of the mirrors determines the angle of incidence $\theta$ that is measured from the normal of the sample as shown in Figure 4.3 (c). For small angles of incidence the mirror frames are placed close to the sample with the mirrors positioned near the top of the frames whilst maintaining the correct focal length to the emitter/detector waveguide horns. When using large samples at small angles of incidence, the position of the horns may be interchanged allowing a crossing of the beams to maintain the correct focal length as shown in Figure 4.3 (a). For large angles of incidence the beams are not crossed and the mirrors placed much further from the sample in the $x$ direction, see Figure 4.3 (b). As for the transmission experiment the second collimating mirror focuses the resultant beam into the detecting waveguide horn fitted with a waveguide–crystal detector allowing an electrical signal to be recorded by the SNA.

Using this method the normal incidence ($\theta = 0°$) reflection response cannot be measured. Therefore even at small angles of incidence it is important to consider the polarisation of the incident beam. Here the TM radiation has the electric field orientated in the $xz$ plane perpendicular to the plane of incidence, if the beam was at $\theta = 0°$ (normal incidence) the electric field would be in the $x$ direction. TE radiation has the electric field vector orientated in the $y$ direction, as shown in Figure 4.3 (d).

## 4.5 Recording Measurements

The *Agilent 8757D* SNA measures and displays the received reference and transmitted signals using a logarithmic decibel (dB) scale. The *reference* signal is measured at the emitter using the directional coupler discussed in section 4.2.1. The *detected* signal pertains to the signal received by the detecting waveguide horn assembly when using either the reflection or transmission experimental setup. The SNA normalises the *detected* signal using the *reference* signal that allows for any fluctuation of power from the source.

All measurements recorded using both of these experimental arrangements are also normalised using a reference sample, referred to as the *free space sample*. For transmis-

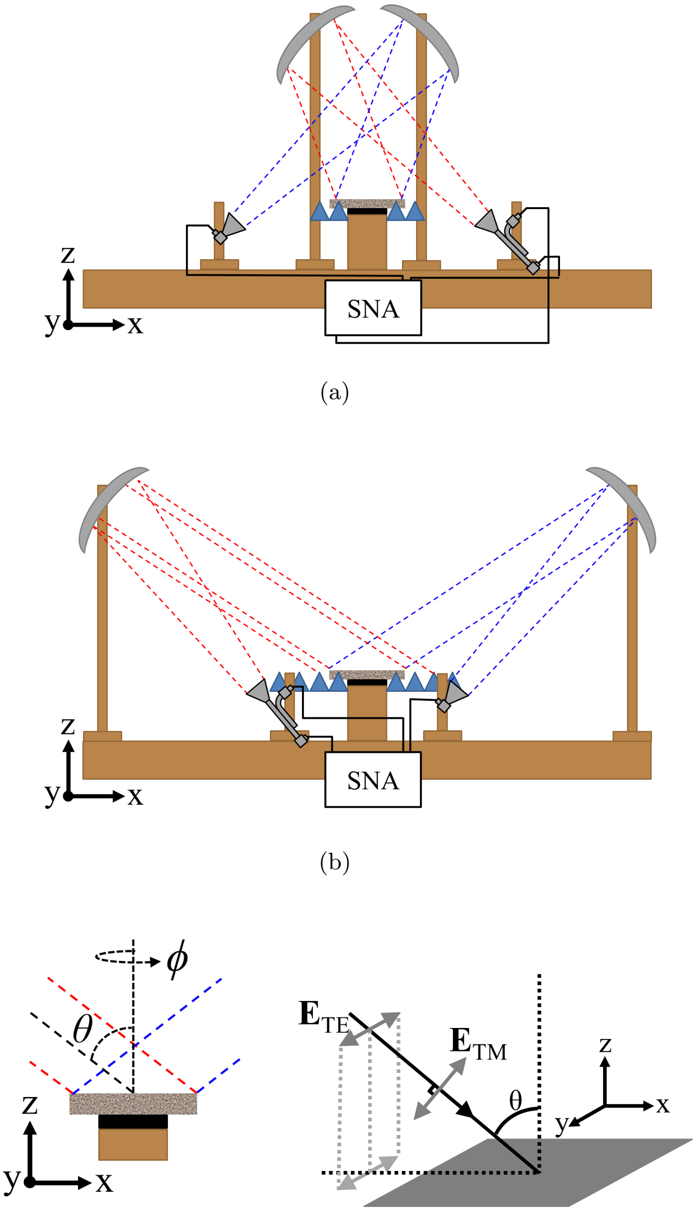

(a)

(b)

(c)

(d)

Figure 4.3: (a) and (b) Schematics showing the experimental arrangement for reflection at small and large angle of incidence $\theta$, where red and blue dashed lines indicate the extent of the incident and reflected beam respectively. (c) Diagram showing the definition of $\theta$ and $\phi$ for a stacked or planar sample. (d) Diagram showing the direction of the electric field vector to define TE and TM polarised radiation.

sion a *free space sample* (i.e. no sample in setup) is used to record 100% transmission, any less than 100% shows the loss in the system. For reflection measurements a flat metallic plate is used (assumed to be infinite), simulating 100% reflection. This normalisation process removes the influence of any loss in the system in cables, waveguide apparatus, and absorption around the apeture so as to document only the transmission or reflection properties of the experimental sample.

Therefore in order to obtain the absolute normalised transmission and reflection coefficient (T and R respectively), shown in all experimental chapters, Equation 4.1 and 4.2 are used:

$$T = 10^{\Delta t/10}, \tag{4.1}$$

$$R = 10^{\Delta r/10}, \tag{4.2}$$

where $\Delta t$ and $\Delta r$ are the difference in the normalised detected signals recorded by the SNA for the *free space sample* and experimental sample.

## 4.6 Other Apparatus

The experimental apparatus detailed above may be combined with two alternative peices of equipment: broad band dual polarised horns (section 4.6.1) and the Vector Network Analyser (section 4.6.2).

### 4.6.1 Broadband Dual Polarised Horns

The broad band dual polarised horns (BB horns) (*Flann DP241-AC*) offer two main advantages over standard gain waveguide horns: the extremely wide operational frequency range and the ability to access orthogonal polarisation orientations without the need for rotation of the horn or housing.

The BB horns are specified to operate in the frequency range $18-50$ GHz ([90] page 93), however through careful investigation it has been shown that this range can be extended down to 8 GHz for these particular units. When used in conjunction with the *Agilent 8757D* SNA, the *Agilent PSG Signal Generator* and a coaxial crystal detector (*Kytar Zero Bias Schottky Detector 303AK*) this is limited to 40 GHz. However this range covers 4 waveguide frequency bands (WG 16, 18, 20 and 22) saving vast amounts of time in the setup and alignment of the experimental apparatus and also leading to continuity in the experimental data between waveguide banded data sets.

The BB horns are comprised of a square waveguide horn antenna and waveguide–coaxial adaptors built as a single combined and optimised unit. When using the waveguide standard gain horns with a waveguide–coaxial adaptor the unit must be rotated by 90° to change the polarisation. Using the BB horns no rotation is needed; the coaxial cable and coaxial crystal detector are simply removed from one coaxial port and attached to the other again saving time and improving accuracy by reducing the amount of re–alignment after every adjustment.

There are some disadvantages when using these BB horns. The main disadvantage is the compromise of performance. Standard gain horns and waveguide–coaxial adaptors are individually optimised for a set frequency band (detailed in table 4.1). The return loss is a measure of the amount of signal reflected within the device back to the incident port (for more information see [6]). Equation 4.3 shows the calculation for return loss in terms of incident power ($P_i$) and reflected power ($P_r$), measured in dB.

$$RL = 10\log_{10}\left(\frac{P_i}{P_r}\right). \tag{4.3}$$

This is one of the main parameters used to test primarily passive microwave components. The waveguide–coaxial adaptor has a maximum return loss of −30 dB, the waveguide standard gain horns (20 dB gain model) −20.8 dB ([90] page 89), whereas the BB horns have a maximum return loss of −7.4 dB. A small negative return loss in dB indicates a large loss in the system that reduces the proportion of signal that may be transmitted or detected by the horn, thus requiring more power.

The second main disadvantage is that the BB horn assembly cannot be connected to a waveguide coupler, so a reference cannot be taken at the source waveguide horn antenna when using the SNA. Although the measurements are normalised to a *free space sample*, this does not account for fluctuations in power from the source.

### 4.6.2 Vector Network Analyser

Until this point the experimental setup has been described in conjunction with the *Agilent 8757D* SNA and *Agilent PSG Signal Generator E8247C* that measures only the amplitude of the electrical signals. The *VectorStar MS4640A* Vector Network Analyser (VNA) measures both amplitude and phase (as used in Chapter 8). Here the coupler providing the *reference* signal and crystal detectors are incorporated in the assembly of the instrument and therefore no external coupler or crystal detectors are required.

The VNA is comprised of a source module, a test set module and an analyser module. The source module defines the operational frequency range of the unit, here being 70 kHz to 70 GHz, offering the potential to operate below 5 GHz with different emitters (such as stripped coaxial probes as used in [92]) and above 40 GHz without the use of external multipliers. In order to span this frequency range of nearly 20 octaves, this VNA essentially combines two VNAs, one operates from 70 kHz to 2.5 GHz, and the second from 2.5 GHz to 70 GHz, using a doubler module to cover the ranges 5 to 20 GHz, followed by a switched doubler module to cover the range 20 to 38 GHz, and finally a quadrupler module to cover the final range above 38 GHz [93]. The source for both units is a varactor-tuned voltage controlled oscillator [94], which is an electronic harmonic oscillator controlled by the voltage input using the varactor diode to control the capacitance of the resonant circuit, allowing the device to produce a range of frequencies. In order to perform phase measurements this internal sweep oscillator is connected to a phase detector to ensure the source remains “phase locked” (or phase matched).

The test set module includes the internal couplers that reference the signal at the ports (connection from the VNA to the device/structure under test). The intermediate frequency (IF) conversion is also performed here. This down-converts the *reference* or *detected* signals into the pass band of the lower IF. Reducing the IF will increase the sensitivity of both the amplitude and phase of the measurement by reducing the bandwidth of the signal. Finally the analyser module receives and interprets the IF signal for amplitude and phase detection, using two tuned receivers; one mixer based (low frequency), the second sampler based (high frequency) [94].

To obtain accurate amplitude and phase measurements the electrical length of the system must be calibrated. There are many types of calibration, for example three of the most commonly used are: SOLT (short, open, load, through), LRL (line, reflect, line), and LRM (line, reflect, match). When used in conjunction with the transmission setup (as used in Chapter 8), the system was calibrated to the end of coaxial cables (where they connect to the waveguide–coaxial adaptors) using a SOLT calibration. This was followed by the *free space sample* normalisation described in section 4.5. With suitable adaptations to the experimental equipment a more accurate calibration could be performed using the LRL calibration where the transmission response through the system measured using no sample (line 1), followed by a flat metal sheet (reflect - 100% reflection, 0% transmission), and finally (line 2) by offsetting the second mirror and horn by $\frac{\lambda}{4}$ (where $\lambda$ is the central wavelength of the frequency band used). Although this calilbration would be valid for a much narrower frequency band (compared to the SOLT calibration on the coaxial cable that spans DC to the coaxial cut off frequency), the waveguide horn response would be included, allowing for more accurate results in phase and amplitude measurements.

The *Anritsu VectorStar MS4640A* offers a much more flexible user interface compared to the *Agilent 8757D* that allows many types of signal manipulation and plotting, however the signal measured here is still processed using the same Equation 4.1 or 4.2 to find the normalised transmission or reflection response for the measured structure as a function of frequency.

## 4.7 Concluding Remarks

In this chapter the experimental apparatus, its operation and arrangement have been discussed for transmission and reflection measurements. First individual elements of the experimental setup were discussed, followed by an explanation of the combination used to measure the transmission and reflection properties of planar or stacked samples. Finally the SNA and VNA operation are discussed in combination with the broad band horns that offer a larger operational frequency range.

# Chapter 5

# Metamaterial Tunnel Barrier Gives A Broad Band of Microwave Transmission

## 5.1 Introduction

In this chapter a subwavelength metallic mesh clad with two layers of low loss dielectric is shown to produce a band of near total microwave transmission over a broad frequency range. The metallic mesh is considered as a tunnel barrier and the response is shown to be analogous to that of a plasmonic metal in the visible regime, with no loss. Upon applying the two dielectric layers on either side of the metallic mesh, two modes arise due to the hyperbolic form of the electromagnetic (EM) field within the subwavelength holes of the metallic mesh. The modes of the whole system are shown to originate from the zeroth–order and first–order Fabry–Pérot modes of the system. The overlap of these modes constructively interferes to give the broad band of transmission. By considering the gradient of the EM fields at the dielectric–metallic mesh interface, almost independent control of each mode is achieved through a suitable choice of geometric parameters.

## 5.2 Background

The microwave response of metallic meshes has been extensively studied since the mid 20th century. Such regular arrays of holes have been optimised for use as frequency selective surfaces (FSS) and band pass filters based upon the transmission peak that occurs near the hole cut–off frequency [1, 2, 45, 95, 96] (see section 2.3.1). Below this cut–off frequency the metallic meshes essentially behave as imperfect mirrors with evanescently decaying EM fields in the holes, as predicted by Bethe [4], and for this reason have historically attracted little interest. However, Ebbesen *et al.*'s observation in the visible regime of enhanced optical transmission (EOT) via tunnelling of the EM fields associated with surface waves (surface plasmon polaritons) through perforated metal films [3] has changed this view (see section 2.3.2). Ebbesen *et al.*'s work helped to ignite interest in the field of patterned and perforated metal structures, that were part of the reinvention of "metamaterials"(see section 2.4.4).

The metallic mesh considered in this study was explored in the non–diffracting regime, i.e. the periodicity of the metallic mesh and therefore the size of the holes are subwavelength, supporting no propagating orders. Recently much work has been conducted on subwavelength metallic meshes demonstrating narrow band resonant EOT for wavelengths near the diffraction edge [97, 98]. Both Dragila *et al.* and Ortuno *et al.* studied the dielectric clad metallic mesh structures in this regime and observed surface wave induced transparency [99, 100]. However, the broad band enhanced transmission observed here cannot be attributed to the excitation of diffractively coupled surface waves due to the very subwavelength nature of the structures considered.

The EM fields in the subwavelength holes decay near–exponentially, that is analogous in character to the fields in a plasmonic metal with a Drude–like dispersion in the visible domain, but here the imaginary effective permittivity is close to zero as discussed in section 2.4.1.1. Hooper *et al.* recently considered a plasmonic metal clad in thin dielectric in the optical regime [101] and noted the parallel between this system and a quantum mechanical tunnel barrier.

A quantum mechanical tunnel barrier must have a potential greater than zero (see Figure 5.1), that is equivalent optically to the square of the wave vector in the incident dielectric medium $-n^2k_0^2 > 0$ with the total energy equivalent to $-k_z^2 = -n_m^2k_0^2\sin^2\theta_m$, (where $n$ is the refractive index, $k_0 = 2\pi/\lambda$ the free space wave vector, $k_z$ is the wave vector in the direction of propagation, $\theta$ is the incident angle and the subscript $m$ relates to the incident medium). The potential is greater than zero if the material that is to act as the tunnel barrier has a purely imaginary or large negative real refractive index. Hooper *et al.* state that ordinary dielectrics correspond to a material with a negative potential, and so only act as tunnel barriers when $k_z$ in the incident medium is less than that in the dielectric. This occurs when $\theta_m < \theta_c$ ($\theta_c$ is the critical angle) at which point total internal reflection occurs. Here materials with an effective negative real permittivity are utilised. Figure 5.1 shows the EM equivalent of a the potential diagram in quantum mechanics for the three layer structure (5 interface) considered in this chapter. The black line indicates the potential for a dielectric cladding of refractive index greater than the semi-infinite incident medium. The tunnel barrier of a dielectric

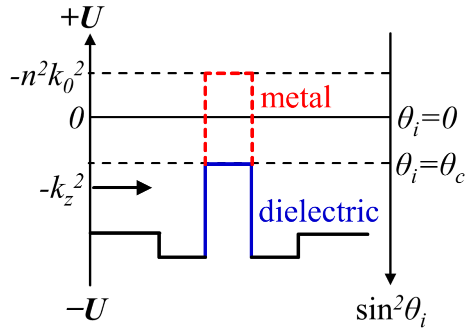

Figure 5.1: The EM equivalent of the potential diagram in quantum mechanics. The blue line indicates the height of the potential for a dielectric at the critical angle, the red dashed line indicates the potential for a lossless metal, and the black line indicates a dielectric cladding.

when the incident EM radiation is at the critical angle is shown by the solid blue line, and the tunnel barrier response of a lossless metal is shown by the dotted red line, that is equivalent to the structure studied here.

Hooper *et al.* showed that the second and third order Fabry–Pérot modes [102] of the dielectric (either side of the metallic mesh) merged into a composite mode as the tunnel barrier thickness increased. The authors employed an idealised analytical system with the optical plasmonic metal represented as a large negative real permittivity with no loss, to gain insight into the nature of these modes. It is not possible to fabricate this idealised structure in the visible regime due to the inherent loss of optical plasmonic metals (such as silver) as well as fabrication and experimental restrictions. Here this is overcome by employing a subwavelength metallic mesh as a plasmonic–like metamaterial in the microwave regime with a large negative real part of the effective permittivity. This produces a zero loss tunnel barrier that can be easily experimentally realised, enabling a detailed investigation into the lower frequency Fabry–Pérot type modes for normal incidence radiation.

Similar structures for transmission through tunnel barriers have been considered where a metallic mesh has been surrounded by layers of metamaterials. Zhou *et al.* used a resonant “H” shaped metallic mesh that was represented as an effective medium [103], with a high permittivity ($\varepsilon_r = 4$). These metamaterial layers allow the EM wave to tunnel through the effective negative permittivity metallic mesh producing two resonant peaks that exhibit transmittance, due to enhanced tunnelling over a frequency range of approximately 1 GHz. Zhou *et al.* also investigated the effect of changing the air gaps between the layers of the structure to show tuning of the two individual modes observed.

In addition Hou *et al.* undertook a study where subwavelength split ring resonators (SRRs) were fabricated around foam balls and held in an array orientated normal to the metallic mesh [104]. When subwavelength SRRs are arranged as an array, the combined response exhibits a large negative permeability over a narrow frequency range [64]. Further, when the SRR arrays are positioned either side of a subwavelength metallic mesh (that exhibits a negative permittivity) a narrow transmittance peak is observed due to a negative refractive index (negative permittivity and negative permeability). Two further narrow peaks are observed at higher frequencies as in this regime the SRR arrays no longer have negative permeability but act as high permittivity dielectric layers that facilitate the EM wave tunnelling through the metallic mesh.

Of direct relevance to this study is an analytical and numerical investigation by Lomakin and Michielssen in 2005 that provides a very thorough discussion of enhanced transmission through a subwavelength metallic mesh sandwiched between two dielectric plates [105]. It is shown that resonant modes can be supported by the metallic mesh coupled to standing waves in the dielectric layers. Two regimes are explored, referred to as the “single resonance” and “double resonance” regimes. In the single resonance regime the incident wave couples to a resonant mode in a single dielectric layer (top or bottom), enhancing the EM fields at a single interface, allowing tunnelling. The resultant resonant transmission feature is very narrow in frequency and does not give 100% transmission. In the double resonance regime, two resonant modes exhibiting 100% transmission are observed where the incident wave couples to standing wave–like solutions in both dielectric layers, this time enhancing the fields on both dielectric–metallic mesh interfaces, allowing strong transmission. This study went on to show the affect of varing the parameters in the system, demonstrating that both regimes may be supported for symmetric as well as asymmetric dielectric cladding, and more importantly exploring the transition from infinitesimally thin to very thick perforated metal plates: for very thin plates the higher frequency mode is much narrower, whereas for very thick plates only one mode is observed with reduced magnitude. This study is in excellent agreement with the numerical and experimental results presented in this chapter.

Here the lowest two Fabry–Pérot modes studied in the aforementioned numerical and analytical work were observed experimentally. In particular a thorough explanation of the lowest frequency mode is presented and its origin as the zeroth–order Fabry–Pérot mode explored. By demonstrating that the metallic mesh may be considered as a metamaterial with a large negative real effective permittivity with no loss it is shown that the zeroth–order and first–order Fabry–Pérot modes can be brought together by manipulation of the sample geometry to result in a broad transmitting band.

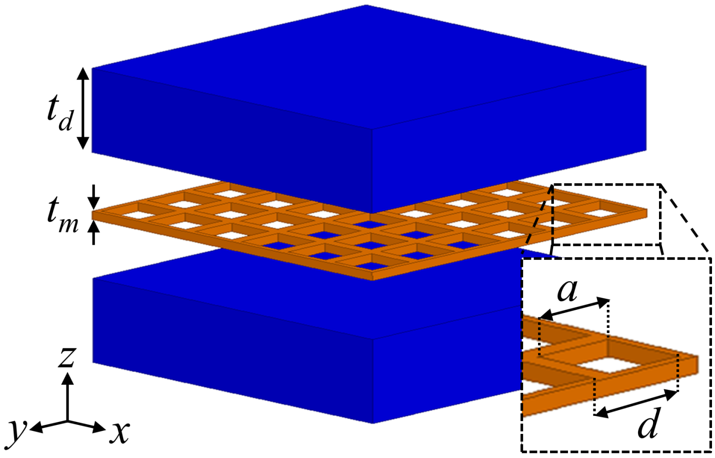

Figure 5.2: Exploded schematic of the experimental sample metallic mesh (orange) of thickness $t_m = 18$ µm, between two low loss dielectric layer (blue) $t_d = 3.175$ mm thick. The copper subwavelength mesh has pitch $d = 5.00$ mm, and hole width $a = 4.85$ mm.

## 5.3 Experimental Measurement

In order to investigate the lowest order modes of this system in the microwave regime the experiment was performed using the three layer sample, an exploded schematic of which is shown in Figure 5.2. A hole array (referred to as the metallic mesh) is chemically etched from a copper clad printed circuit board (PCB) [106]. The resultant copper mesh is 18 µm (± 0.5 µm) thick and comprises of square air filled holes of width $a = 4.85$ mm (± 0.02 mm) and pitch $d = 5$ mm (± 0.02 mm). An identical copper clad PCB is fully etched and placed so as to sandwich the metallic mesh and bolted into place in a wooden frame to prevent air gaps between the two layers. The PCB is Nelco NX9255 of thickness $t_d = 3.175$ mm (± 0.03 mm). The relative permittivity and dielectric loss tangent were experimentally measured to be $2.96 \leq \varepsilon \leq 3.08$ and $0.001 \leq \tan\delta \leq 0.009$ respectively, using the process detailed below (section 5.4.1). The experimental sample was considered as infinite in the $xy$–plane since the area is much greater than the finite size of the microwave beam spot.

### 5.3.1 Transmission Measurements

A collimated beam of microwave radiation was used to investigate the transmission response of this sample. The experimental arrangement, described in Chapter 4 consists of a waveguide standard gain horn antenna placed at the focus of a spherical mirror, that produces near parallel wave fronts perpendicular to the direction of propagation,

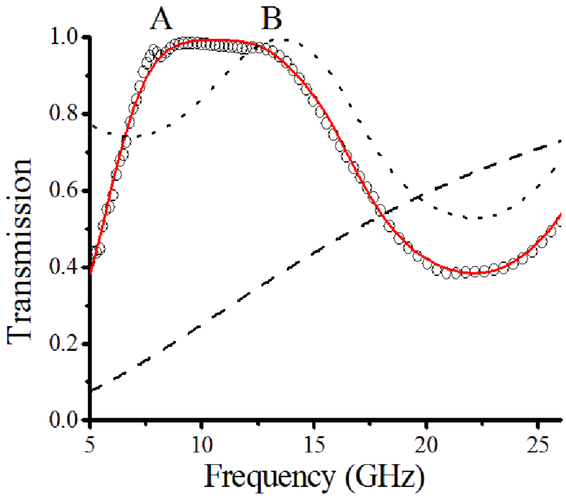

Figure 5.3: Experimentally measured (black circles), and numerically modelled (red continuous line) normal incidence transmittance for the dielectric–clad subwavelength metallic mesh shown in Figure 5.2. The black dashed line is the numerically modelled response of the unclad subwavelength metallic mesh in free space and the black dotted line is the modelled response of the sample without the metallic mesh layer. Points A and B represent the approximate position of the maxima of the two resonant features that combine to give the broad transmission band.

and a similar mirror collects radiation transmitted through the sample (placed between the mirrors) focusing it into a detector. The transmitted radiation is converted into an electrical signal that may be interpreted by the scalar network analyser (SNA).

## 5.4 Experimental Results

The experimentally measured normal incidence transmittance of this sample is shown in Figure 5.3 (black circles), together with a best fit from a finite element method (FEM) numerical model (continuous red line). To fit the experimental data a dielectric thickness of 3.15 mm was used consistent with the experimental average thickness of 3.175 mm ± 0.030 mm. A band of near–complete transmission is observed over the frequency range 7 – 15 GHz. This structure exhibits greater than 300% transmission enhancement when compared to the FEM modelled response of a single freestanding metallic mesh with no dielectric cladding (Figure 5.3 - dashed line).

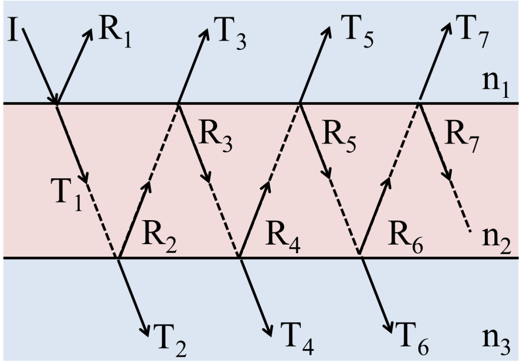

Figure 5.4: Schematic of an EM wave propagating in a three layer system, where $I$ is the incident wave, $R$ and $T$ are the reflection and transmission coefficients at each interface, and $n_m$ is the refractive index in medium $m$ (where $m = 1, 2$, or 3).

### 5.4.1 Measuring the Properties of the Dielectric

After initial FEM modelling failed to fit the experimentally obtained spectra using frequency independent permittivity and dielectric loss tangent values of $\varepsilon = 2.59$ and $\tan\delta = 0.0018$ (specified by the manufacturer at 10 GHz), the complex permittivity was experimentally quantified more accurately by obtaining the complex transmission through one, two and three blank PCBs using a vector network analyser (VNA) between 5 GHz and 26 GHz. The resultant transmission values were then entered into a numerical fitting code, written by Dr. Hendry (University of Exeter). This numerical fitting routine solves the three layer (two interface) Fresnel equations (shown below) using a predefined range of the real and imaginary parts of the refractive index ($n$ and $k$). For a derivation of the Fresnel equations for single and recursive interfaces see [107].

$$t_{n_u,n_v} = \frac{2\sqrt{n_u n_v}}{n_u + n_v}, \tag{5.1}$$

$$r_{n_v,n_u} = \frac{n_v - n_u}{n_u + n_v}, \tag{5.2}$$

where $t_{n_u,n_v}$ is the transmission amplitude, $r_{n_v,n_u}$ is the reflection amplitude, $n_v, n_u$ are either $n_1, n_2$ or $n_2, n_3$ as shown schematically in Figure 5.4. In this instance $n_1 = n_3 = 1$ (air), and $n_2 = n + ik$ is the refractive index of the dielectric in question. By entering limits for the values of $n$ and $k$ and the resolution required, the complex transmission amplitude is calculated using the equations below for each combination of $n$ and $k$.

$$t_{1,3} = \frac{t_{n_1,n_2} t_{n_2,n_3} e^{\beta}}{1 + r_{n_2,n_1} r_{n_3,n_2} e^{\beta}}, \tag{5.3}$$

$$\beta = i2\pi k_0 n_2 l, \tag{5.4}$$

where $l$ is the sample thickness. At this point Equation 5.3 is compared to the corresponding parts of the experimentally measured data. The difference between the two is calculated and the result with the smallest difference chosen for each frequency. This was repeated for a single layer of thickness $l = t_d = 3.175$ mm, two layers bolted together of thickness $l = 2 \times t_d = 6.35$ mm, and three layers bolted together of thickness $l = 3 \times t_d = 9.525$ mm and the results averaged.

It was found that the relative permittivity varied from $\varepsilon = 2.96$ to $\varepsilon = 3.08$ and the dielectric loss tangent ($\tan\delta = \varepsilon''/\varepsilon'$) remained at $\sim 0.001$ for frequencies $5 - 15$ GHz, followed by a large increase, peaking at $\tan\delta = 0.009$ at 23 GHz. Using these values a much improved numerically modelled response is shown in Figure 5.3 (continuous red line).

## 5.5 Analysis Using the Numerical Model

Numerical modelling helps to gives physical insight into the origins of the broad highly transmitting region, showing it to be comprised of two modes with their overlap summing to give a transmissivity much higher than that of an isolated metallic mesh (dashed line in Figure 5.3). A low frequency mode is centred about point A in Figure 5.3 and a higher frequency mode is centred about point B. Since the frequencies of both modes are below the cut–off frequency of the holes, the EM field within the metallic mesh is evanescent.

Point B defines the upper edge of the highly transmitting band, the electric field at this frequency is plotted in Figure 5.5 for a line taken through the centre of a subwavelength hole in the propagation direction. This mode is essentially the first–order (half wavelength) Fabry–Pérot mode of the dielectric block. This is unsurprising as for a block of dielectric 6.35 mm thick with no metallic mesh, Fabry–Pérot type modes [102] (see section 2.4.2) were expected and duly observed (Figure 5.3 – dotted line) with the first–order mode occurring at 13.5 GHz, just above point B. The addition of a very thin subwavelength metallic mesh has almost no influence on this mode as the evanescent decay of the EM fields within the metallic mesh couple between the front and back faces where the electric field forms an asymmetric mode with a hyperbolic sine (*sinh*) character about the centre of the structure that passes through zero at the centre of the holes (in $z$). The hyperbolic form of the EM fields within the subwavelength holes was first described by Gadsdon *et al.* in [108] for a finite stack composed of metal–dielectric unit cells in the visible regime where the thickness of the dielectric was greater than twice the evanescent decay length. The authors considered analytical expressions for the EM fields for all the modes. Here comparisons can be drawn with the high frequency band edge modes where the character in the metal regions is shown to be *sinh*–like. The form of the electric field within the subwavelength holes of the metallic mesh couples to the standing waves in the dielectric, forming an asymmetric mode in the overall structure (relative to the centre of the structure in $z$).

However, it is mode A, the low frequency edge of the enhanced transmission band, that is of most interest. In the same way as we have considered mode B to be a modification of the first–order Fabry–Pérot mode, mode A can be considered as a perturbation of the zeroth–order Fabry–Pérot mode. Without the metallic mesh acting as a tunnel barrier, the zeroth–order Fabry–Pérot mode of the dielectric is supported at an infinite wavelength with a uniform EM field profile across the dielectric cavity. However, when the metallic mesh, acting as a tunnel barrier, is introduced the standing waves in the dielectric couple via the evanescent fields supported in the metallic mesh, and give rise to a symmetric mode of the whole system and a hyperbolic cosine–like (*cosh*–like) electric field distribution. Gadsdon *et al.* predicted the *cosh*-like electric field profile within the metal layer of the analytical representation of the metal–dielectric stack in the visible regime for the lowest frequency mode of the transmitting band. Figure 5.3 illustrates the numerically modelled electric field profile of mode A, plotted along a line through the centre of one metallic mesh hole: here the *cosh*–like function extends far beyond the confines of the metallic mesh (represented by a vertical black dashed line) due to the slow gradient across the metallic mesh–dielectric boundaries. The thickness of the metallic mesh, the pitch and hole filling fraction, dictate the fields and their gradients at the metallic mesh–dielectric interface. The matching condition at this interface therefore defines the mode's apparent wavelength in the dielectric, that is much greater than twice the overall sample thickness (i.e., the naïve Fabry–Pérot wavelength), and therefore its resonant frequency. As expected, mode A is highly sensitive to these three metallic mesh parameters and this allows for a substantial degree of freedom in dictating the low frequency edge of the transmission band.

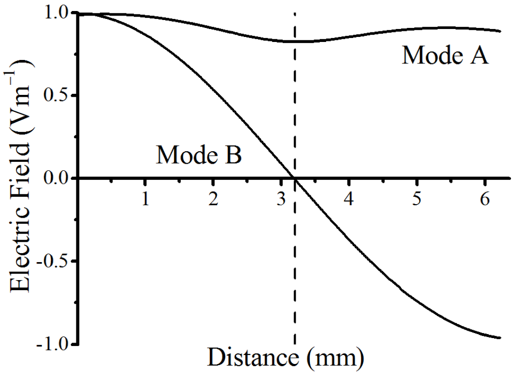

Figure 5.5: Electric field profile for the two modes labelled as A and B in Figure 5.3 plotted along a line in the $z$ direction that passes through the centre of a hole in the subwavelength metallic mesh. Mode A was plotted at 7.42 GHz and mode B was plotted at 12.06 GHz.

### 5.5.1 The Affect on the Transmission Response When Varying the Metallic Mesh Parameters

In Figure 5.6 the transmissivity arising from these two modes is plotted as a function of frequency and metallic mesh thickness using recursive Fresnel equations for a five layer system; the semi-infinite incident medium (air), the dielectric superstrate, the metallic mesh, the dielectric substrate and the semi-infinite exit medium. Such a modelling code was implemented by Dr. Hooper (University of Exeter), using an effective permittivity for the metallic mesh. In this arrangement the metallic mesh can be represented as an effective medium because pitch and hole size associated with the metallic mesh are much smaller than the wavelength of the incident radiation ($\sim \frac{\lambda}{2.4}$). The effective parameters of the metallic mesh were obtained for each thickness using a combination of modal matching and effective medium theory developed by Dr. Taylor (University of Exeter) [88]. The reflection and transmission amplitudes ($r$ and $t$ respectively) were found using a modal matching technique as a function of frequency and the metallic mesh dimensions (assumes the metal is PEC). These values were then used to calculate an effective impedance ($Z_{eff}$) and effective refractive index ($n_{eff}$) of the metallic mesh layer using the relationships in [109]: Equations 5.5 and 5.6 respectively. From the effective impedance and refractive index, the effective permittivity ($\varepsilon_{eff}$) and permeability ($\mu_{eff}$) can be found using Equations 5.7 and 5.8 (only valid for normal incidence). These effective parameters reveal a large negative effective permittivity at low frequencies that follows a Drude–like dispersion (see section 2.4.1.1) with an imaginary permittivity equal to zero (as expected). The permeability was found to have a real part equal to unity and a imaginary part equal to zero. The frequency dependent effective permittivity values obtained for each metallic mesh thickness were used in Figure 5.6 ($t_m = 1\ \mu\text{m} - 2000\ \mu\text{m}$) and are shown for a range of metallic mesh thicknesses in Figure 5.7.

$$Z_{eff} = \frac{\sqrt{1 + 2r + r^2 - t^2}}{\sqrt{1 - 2r + r^2 - t^2}}, \tag{5.5}$$

$$n_{eff} = \frac{ct_m}{2\pi f} \sin^{-1}\left(\frac{2iZ_{eff}}{Z_{eff} - 1}\frac{r}{t}\right), \tag{5.6}$$

$$\varepsilon_{eff} = \frac{n_{eff}}{Z_{eff}}, \tag{5.7}$$

$$\mu_{eff} = n_{eff} \cdot Z_{eff}. \tag{5.8}$$

For a real plasmonic metal in the visible regime the permittivity does not change with thickness. Here Figure 5.7 shows the effective permittivity does vary with thickness for the metallic mesh. Effective medium theory considers only the reflection and transmission coefficients for each metallic mesh thickness and assigns an effective permittivity (and permeability) to a 2D sheet. It does not account for the evanescent decay inside the layer, and so as the thickness increases, the electric field gradient of the metallic mesh reduces, so reducing the magnitude of the effective permittivity.

Consider reference [101] in which the variation of the tunnel barrier thickness corresponds to variation in the real thickness of the real optical metal. Here variation of the effective tunnel barrier thickness that corresponds to a change of the coupling through the metallic mesh, can be achieved by either changing the real thickness of the metallic mesh (Figure 5.6) and/or the filling fraction of the hole with respect to the pitch (Figure 5.10). Both Figures show that the higher frequency mode B is only weakly frequency dependent upon changes in the metallic mesh thickness. This is because the electric field within the subwavelength holes of the metallic mesh is near zero for this mode, as shown in Figure 5.5. However for the low frequency mode A, the high regions of electric field are concentrated within the subwavelength holes of the metallic mesh.

As the thickness of the metallic mesh increases (Figure 5.6), mode B decreases in frequency as the amplitude of the hyperbolic fields inside the subwavelength holes of the metallic mesh decreases. The gradient of the EM fields at the metallic mesh–dielectric interface shallows supporting a longer effective wavelength. For clarity see Figure 5.9 lower left and right panels where an exaggerated schematic illustrates the form of the electric fields when changing the thickness of the metallic mesh. On the other hand, mode A increases in frequency as the amplitude of the *cosh*-like form of the electric

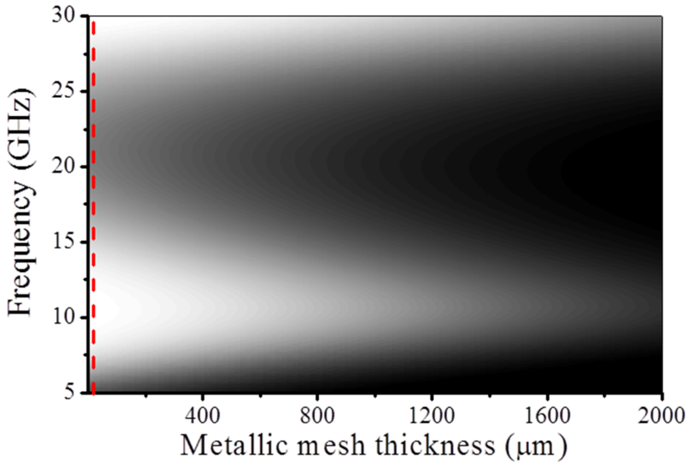

Figure 5.6: Transmission as a function of frequency and tunnel barrier thickness for the dielectric clad metallic mesh where the dielectric has a thickness $t_d = 3.175$ mm, and a relative permittivity $\varepsilon_r \sim 3$ and the metallic mesh is represented by frequency and thickness dependent effective permittivity (shown in Figure 5.7) following a Drude–like character with no loss. Note: Black 0%, White 100% transmission.

fields in the metallic mesh decreases. The shallowing of the gradient at the metallic mesh–dielectric interface leads to a decrease in the effective wavelength of the resonant mode. As the metallic mesh thickness increases, the modes converge, narrowing the transmission band with decreasing intensity, again see Figure 5.9. The response of the sample thickness experimentally studied is indicated by the vertical red dashed line close to the origin in Figure 5.6.

In a similar way by changing the size of the holes in the subwavelength metallic mesh the amplitude of the evanescent fields can be varied, and the transmission band width tuned. Figure 5.10 shows the FEM modelled transmission response as the hole width is increased while the pitch stays constant. Decreasing the hole size increases the frequency of the waveguide cut off, allowing a shorter decay length at these frequencies; mode A rises in frequency towards mode B, that also reduces in frequency a small amount, overall reducing the transmission bandwidth.

### 5.5.2 The Affect on the Transmission Response When Varying the Properties of the Dielectric

It is also instructive to establish how the highly transmitting region varies with dielectric parameters. Increasing the permittivity of the dielectric layers whilst reducing the

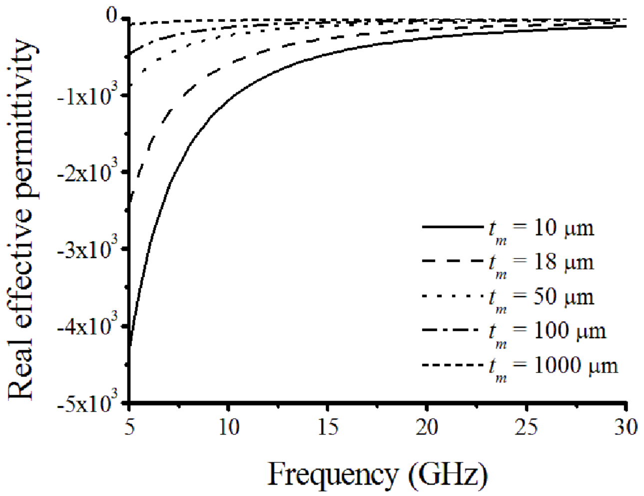

Figure 5.7: A selection of frequency dependent effective real permittivities for varied metallic mesh thicknesses.

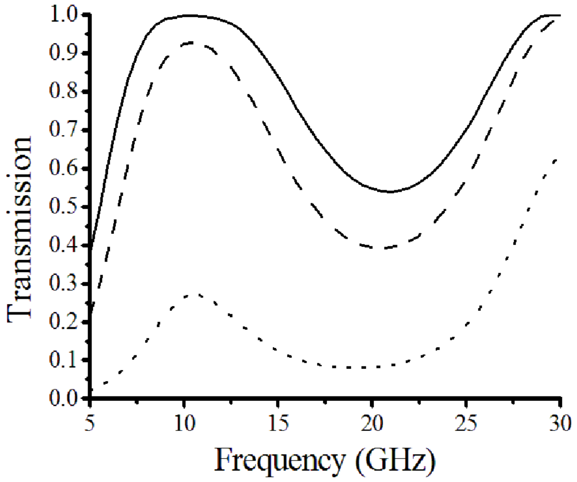

Figure 5.8: Transmission line plots as a function of frequency extracted from Figure 5.6 corresponding to metallic mesh thicknesses of $t_m$ = 10 μm (solid line), $t_m$ = 400 μm (dashed line) and $t_m$ = 2000 μm (dotted line).

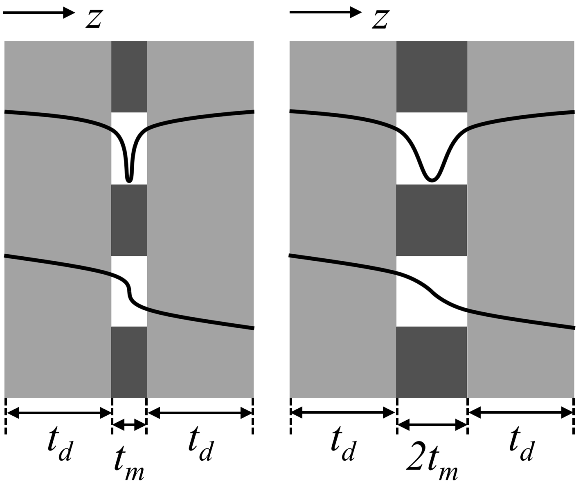

Figure 5.9: Exaggerated schematic showing the electric field profiles (black) for the low and high frequency resonant modes (top and bottom respectively), for the dielectric clad (light grey) metallic mesh (dark grey) of two thickness $t_m$ and $2 \times t_m$ (left and right respectively).

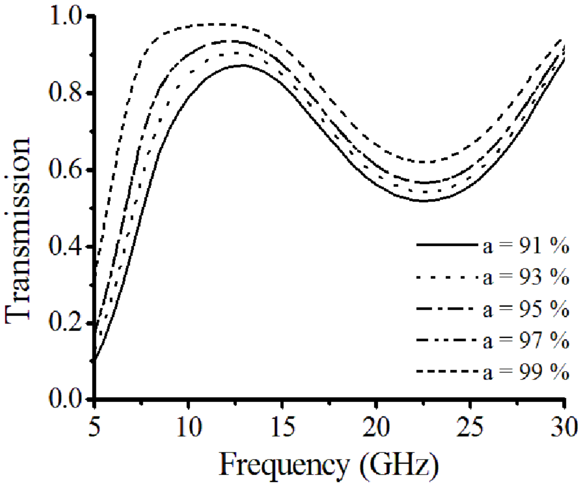

Figure 5.10: FEM modelled normal incidence transmittance for the metallic mesh clad in dielectric, the pitch is fixed at $d = 5$ mm, and the hole side is varied. The metallic mesh thickness is $t_m = 18$ µm and dielectric thickness is $t_d = 3.175$ mm.

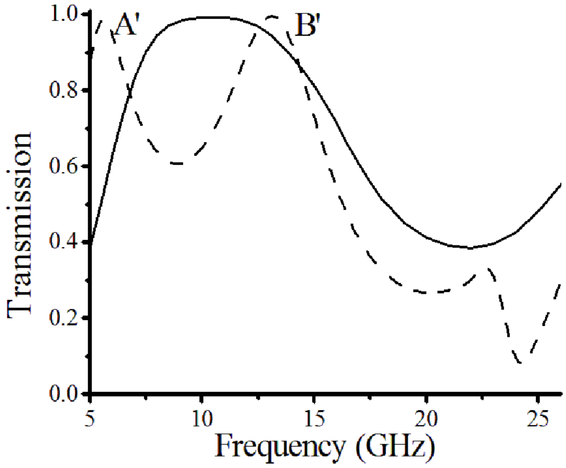

Figure 5.11: FEM modelled normal incidence transmittance for the metallic mesh clad in dielectric where the metallic mesh parameters and optical length of the dielectric layers are kept constant, two frequency dependent refractive indicies are used in combination with dielectric thicknesses of $t_d = 3.175$ mm (solid line) and $t_d = 1.8$ mm (dashed line).

thickness, the optical length $(n \cdot t_d)$ is kept constant, modes A' and B' may be clearly separated as shown in Figure 5.11. Here the optical length was found using the measured frequency dependent permittivity values used in the numerical model (Figure 6.3 continuous red line). The thickness of the dielectric layers was reduced to $t_d = 1.8$ mm (from $t_d = 3.175$ mm) and the frequency dependent permittivity and dielectric loss tangent values adjusted accordingly $9.19 \leq \varepsilon \leq 9.59$. The separation of the resonant transmission peaks arises from the increased reflectivity at the air–dielectric boundary, giving sharper modes so mode B tends towards the perfect Fabry–Pérot limit. The low frequency mode A reduces in frequency due to the increase in the field gradient at the metallic mesh–dielectric interface, supporting a longer effective wavelength.

By decreasing the dielectric thickness $(t_d)$ alone whilst maintaining a constant refractive index, the band width may be increased whilst maintaining a high level of transmission. This effect is shown in Figure 5.12 where as the thickness decreases, mode A increases only slightly in frequency as the response of this mode is dominated by the gradient at the metallic mesh–dielectric boundary and therefore the reduction in the thickness of the dielectric only weakly perturbs it. By contrast, mode B is almost entirely dependent upon the partial standing waves in the dielectric layers. As the thickness of the dielectric decreases this mode shifts to much higher frequencies. Both modes broaden as the reflectivity at the air–dielectric boundary reduces with in-

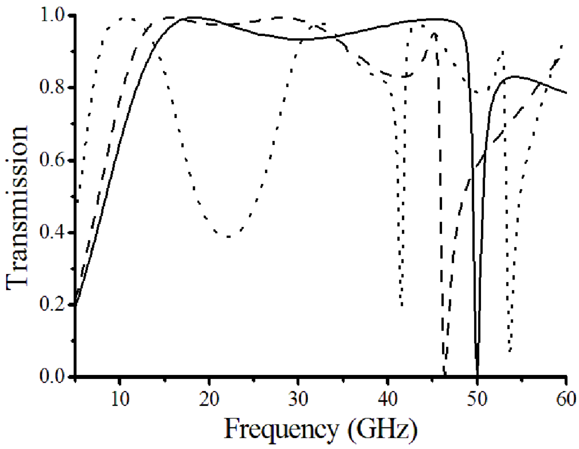

Figure 5.12: FEM modelled normal incidence transmittance for the metallic mesh clad in dielectric of varying thickness: $t_d = 3.15$ mm (dotted line); $t_d = 1.5$ mm (dashed line) and $t_d = 1$ mm (continuous line).

creasing frequency. Through a suitable choice of parameters a pass band with a width $> 20$ GHz, with a transmission of almost 100% may be experimentally realised in this three layer system. The upper bound of this pass band is largely limited by the onset of diffraction that is determined by the pitch of the metallic mesh.

## 5.6 Concluding Remarks

The transmission response of a structure composed of a subwavelength metallic mesh symmetrically clad in dielectric layers has been experimentally measured and explained using a combination of numerical and analytical modelling. The experimentally observed broad, highly transmitting band was shown to be due to the superposition of two non interacting modes. Both modes originate from Fabry–Pérot modes of the dielectric cladding. Below the cut off frequency of the subwavelength holes the metallic mesh may be considered as analogous to a metamaterial with a frequency dependent effective permittivity similar in character to a plasmonic visible metal with a Drude–like dispersion. However, in this structure there is no loss so the imaginary part of the effective permittivity is zero, and therefore this structure may act as an ideal tunnel barrier. The electrical field profile for Mode B reveals a small modification to the first–order (half wavelength) Fabry–Pérot mode in the dielectric, through the introduction of the metallic mesh the evanescent fields that couple between the front and back faces of the metallic mesh to form an asymmetric *sinh*–like mode. Mode A, more surprisingly, reveals a symmetric (*cosh*–like in the metallic holes) mode that is derived from the zeroth–order Fabry–Pérot mode of the dielectric. Without the metallic mesh this mode would exist at infinite wavelength; by introducing a tunnel barrier the EM fields within the structure are quantised. The corresponding wavelength is much greater than twice the thickness of the structure. Analytical modelling shows an increase in the resonant frequency of mode A as the metallic mesh thickness increases. The combination of these two modes gives a transmission pass band with a transmission coefficient almost equal to 1 for the frequency range $7 - 15$ GHz. By suitable optimization of parameters this near unity transmission band could be maintained over 50% of the frequency band ($>$ 20 GHz) below diffraction.

# Chapter 6

# Microwave Transmissivity of a Metamaterial–Dielectric Stack

## 6.1 Introduction

In this chapter a series of subwavelength metallic meshes are considered as metamaterial layers with an individual microwave response analogous to that of a plasmonic metal in the visible regime, however these metamaterial layers exhibit no loss. By stacking these layers between thick dielectric slabs the analogy is extended to the response of a metal–dielectric stack in the visible regime. Experimental transmission data is recorded and compared to a numerical model that is used to plot the electric field profiles for each resonant transmission mode and the frequency of each is shown to depend on the combination of *cosh*-like and *sinh*-like form of the electric field in the metamaterial layers. The frequency of the lowest frequency resonant mode is shown to be predominantly dependent on the metallic mesh properties, not the number of unit cells in the stack. Finally "cladding" - dielectric that is half the thickness of the dielectric cavities is applied to the top and bottom of the stack, and the numerically modelled transmission band pass is smoothed from discrete peaks to a series of broad transmission peaks creating a continuous highly transmitting band.

## 6.2 Background

Multilayer metal–dielectric structures have been extensively studied at visible frequencies since the beginning of the 20th century. Geffcken in 1939 [110] fabricated metal–dielectric thin film stacks that exhibited transmission features that were significantly narrower than those previously observed in conventional dielectric–dielectric multilayer arrangements, due to the reflectivity of the metal layers [54]. The spectral response of metal–dielectric stacks in the visible regime comprises a series of band gaps where the reflectivity is high (and the transmissivity is low), separated by a series of peaks of high transmissivity. The transmission peaks observed in the visible response of a metal–dielectric stack correspond to near-standing-wave resonances within each dielectric cavity, that couple together via exponential fields within the metal film. Near the high frequency band edge of the first transmission band, the electric fields are predominantly confined to the dielectric and pass through zero in the metal region. In contrast, at the low frequency band edge a significant proportion of the field enhancement occurs inside the metal regions [68, 111, 112].

Gadsdon *et al.* [108] considered alternating layers of metal and dielectric films in the visible regime, and showed through analytical manipulation that the metal film acts as a tunnel barrier with the electric fields within the metal films taking either a hyperbolic sine (*sinh*)–like or hyperbolic cosine (*cosh*)–like form. More recently a structure consisting of many stacked periods of a metal–dielectric unit cell demonstrated resonant transmission many order of magnitude greater than that of a single metal layer of equivalent thickness [113].

An equivalent study of the metal–dielectric stack in the microwave regime is possible using metallic meshes as a plasmonic metamaterial layer with a Drude-like permittivity but exhibiting no loss as previously discussed. The metamaterial layer consists of a non-diffracting square metallic mesh of air filled square holes. At wavelengths greater than the size of the holes, the electromagnetic (EM) fields are evanescent within the holes with a decay length that is primarily dictated by the metamaterial geometry. Consequently the metallic mesh exhibits a large effective permittivity dominated by the negative real part that is equivalent to a thin continuous layer with a pure imaginary refractive index (such as a plasmonic metal in the visible regime) [3, 114–116].

The transmission resonances observed in the experimental results presented in this chapter should not be confused with the enhanced optical transmission (EOT) phenomena first recorded by Ebbesen *et al.* [3], that relies on the excitation on diffractively coupled surface plasmons. A wealth of work shortly followed demonstrating Ebbesen *et al.*'s EOT for stacked structures in both the optical regime [117–125] and the microwave regime [41, 126–136]. Subsequently these structures were also shown to exhibit a negative refractive index in this EOT regime where the wavelength is comparable to the pitch $\lambda \approx d$.

One such structure that exhibits a negative refractive index over a specific frequency range is the "double fishnet" structure, an exploded schematic of which is shown in Figure 6.1. The structure consists of alternating thin layers of subwavelength metallic mesh and dielectric, that are stacked such that neighbouring metallic mesh layers are separated by dielectric of thickness less than twice the evanescent decay length of the

EM fields. The EM response of this structure possesses a frequency region close to the onset of diffraction where both the effective permittivity and effective permeability are negative simultaneously. When the incident electric field is orientated parallel (and the magnetic field perpendicular) to the narrow metal strips, the structure supports surface plasmons (or spoof surface plasmons for a PEC mesh) enhancing the transmission through the meshes (EOT). Different elements of the structure are responsible for creating the effective negative permeability and negative permittivity. The broad metallic strips provide the negative permeability; the incident magnetic field perpendicular to the strips induces anti-parallel currents in neighbouring layers. The response will be dia- or para-magnetic depending on whether the incident wavelength is shorter or longer than the magnetic resonance of the coupled strips [137]. This has also been described as the gap (spoof) surface plasmon, as the metallic meshes support anti-parallel (spoof) surface plasmons that couple between metallic meshes causing the negative effective permeability [135]. The negative permittivity is determined by the size of the holes (width $a_x$ and $a_y$) and pitch ($d_x$ and $d_y$). For a PEC mesh the effective permittivity is determined by the proximity to the cut–off frequency associated with the holes, when the incident wavelength is larger than the holes the effective permittivity is dominated by the negative real part as explained previously. However for metals in the optical regime, it is the proximity to the surface plasmon resonance that determines the form of the permittivity [135]. Originally designed as two metallic meshes separated by a single dielectric in the optical regime the theoretical analysis and experimental response both showed a tunable frequency range where a negative refractive index was supported [122–125]. This work was then replicated in the microwave regime in a stacked form [127, 138]. The response of this structure bears similarities to the work considered in this chapter. However the frequency range used in the present study is far below the onset of diffraction at 60 GHz, and hence these surface plasmon modes, "spoof" or otherwise, cannot play a role. Also the dielectric spacing between metallic meshes considered here is much larger than twice the evanescent decay length. Therefore the metallic meshes are not placed close enough for the evanescently diffracted fields to interact, as shown in section 6.8.

Here by measuring the transmission through a metallic mesh–dielectric stack and fitting a numerical model to these results, the electric field profiles may then be extracted for each resonant mode showing the *sinh* or *cosh*-like nature of the fields inside the subwavelength holes of the metallic mesh. These couple to a *cosine*-like half wavelength mode in the dielectric regions for the first transmission band pass. The parameters that allow tuning of the transmission response are discussed and particular attention paid to the lower frequency band edge. With the possibility of shifting the resonant frequency of the lowest frequency mode to a corresponding wavelength larger than the

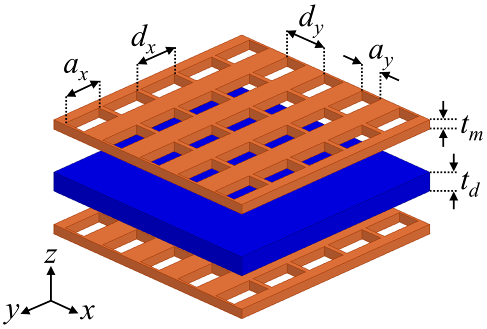

Figure 6.1: Exploded schematic of the double fishnet structure, where $d_x$ and $d_y$ are pitches in the $x$ and $y$ direction, here set to be equal. The hole widths $a_x$ and $a_y$ are unequal. The thickness and the metallic mesh $t_m$ and separating dielectric $t_d$ are of the same order of magnitude. (not to scale)

physical length of the whole structure by changing only the metallic mesh parameters and not the number of unit cells (as expected for a dielectric–dielectric stack).

## 6.3 Experimental Measurement

The experimental sample shown in Figure 6.2 is comprised of eight copper clad printed circuit board (PCB) layers. The copper is removed from three of these substrates, the remaining five being etched to leave a copper square mesh of thickness $t_m = 18$ μm (± 0.5 μm) with periodicity $d = 5$ mm (± 0.02 mm) and hole side length $a = 4.85$ mm (± 0.02 mm). The PCB substrate is a commercially available dielectric (Nelco NX9255) of thickness $\frac{1}{2}t_d = 3.175$ mm (± 0.03 mm) (stacked in pairs with metallic meshes either side $t_d = 6.35$ mm), with experimentally measured frequency dependent permittivity and dielectric loss tangent $2.96 \leq \varepsilon \leq 3.08$ and $0.001 \leq \tan\delta \leq 0.009$ as described in section 5.4.1. For the purposes of this discussion a unit cell is considered as a dielectric cavity bounded by metallic meshes either side. However, strictly this structure is composed of 4 unit cells, each containing single a metallic mesh and a single dielectric cavity, plus an extra metallic mesh.

The sample is considered as infinite in the $xy$–plane since the sample area is much greater than the finite size of the microwave beam spot. In order to experimentally investigate the EM transmission response of this sample, a collimated plane wave of microwave radiation (5 GHz $\leq \nu \leq$ 30 GHz) is directed onto the $xy$–plane of the sample at normal incidence as described in Chapter 4.

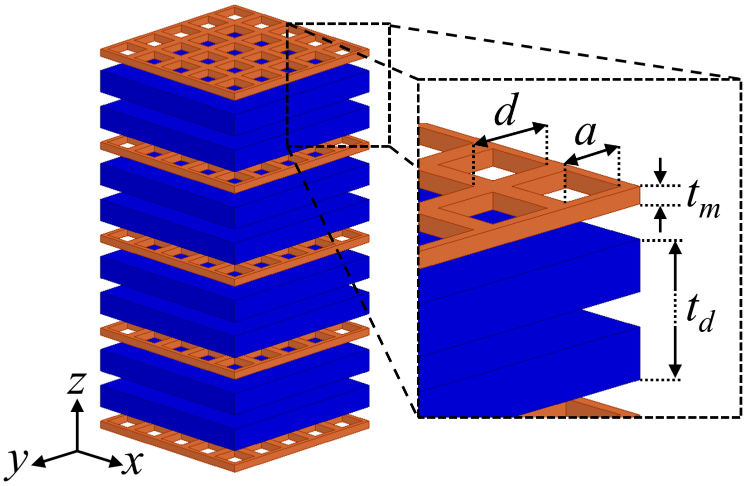

Figure 6.2: Exploded schematic of the metamaterial–dielectric experimental sample, blue regions represent the low loss dielectric Nelco NX9255 of total thickness $t_d$ = 6.35 mm and orange layers represent the metallic mesh of square air filled holes of pitch $d = 5$ mm, hole size $a = 4.85$ mm, and thickness $t_m = 18$ µm. (not to scale)

## 6.4 Experimental Results

The experimental transmission spectrum (Figure 6.3, black circles) shows the first two transmitting band pass regions. Each transmission band is comprised of a set of $N$ resonant modes, where $N$ is equal to the number of unit cells in the sample. In what follows, discussion is limited to the first transmission band since this is sufficient to fully understand the structure's fundamental behaviour. The resonances in bands at higher frequencies simply correspond to higher order modes in the dielectric cavities (i.e. a full wavelength), retaining similar field distributions within the subwavelength holes of the metallic mesh. The experimental transmission maxima relating to the four resonant modes in the first transmission band are labelled A through D (Figure 6.3).

To obtain an accurate prediction of the microwave response of the stack using FEM modelling shown in Figure 6.3, an adequate representation of the fields within the subwavelength holes of the thin metallic mesh layers was essential. This was achieved by increasing the density of the tetrahedral mesh employed in the model in these regions until convergence was obtained, see section 3.4 for more details. The parameters used in the model are as described in section 6.3.

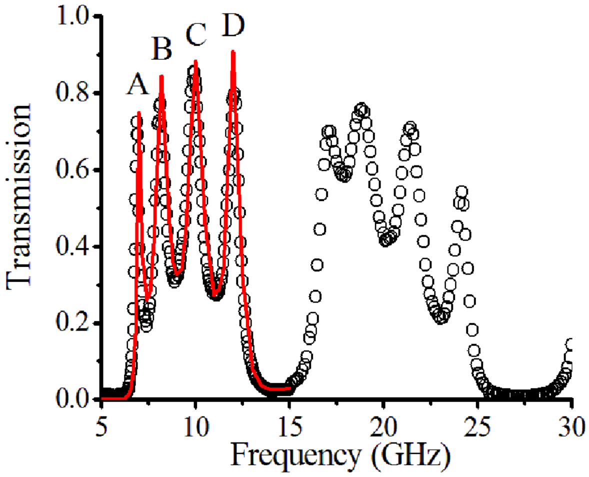

Figure 6.3: Experimental transmission response (black circles) illustrating the first two pass bands separated by band gaps. Numerically modelled data are also shown (red line) for the first pass band (5 – 15 GHz).

## 6.5 Analysis Using the Numerical Model

Figure 6.4 illustrates the FEM modelled time-averaged electric field distributions along a line running in the $z$-direction passing through the centre of the holes in the metallic mesh. The transmission resonances observed (Figure 6.3) occur when *sine* or *cosine*-like standing-waves in the dielectric layers (relative to the centre of each layer) couple via evanescent fields within the subwavelength holes of the metallic meshes. The form of the fields in the dielectric layers depends on the pass band. The fundamental pass band supports a $m\lambda/2$ resonance where $m = 1$, corresponding to a half a wavelength in each cavity. The second band pass, $m = 2$, supports a full wavelength resonance in each cavity, and so on for increasing band pass regions.

By considering the metallic mesh as a plasmonic metamaterial with an effective permittivity dominated by the large negative real part, these layers act as tunnel barriers [101, 139]. The electric fields within the metal films take either a hyperbolic sine (*sinh*) or hyperbolic cosine (*cosh*) form [108]. However here the hyperbolic fields extend outside the metallic mesh layer due to the shallow gradient of the evanescent field decay across the metallic mesh–dielectric interfaces. The hyperbolic parts of the field distribution do not occur symmetrically in the second and fourth metallic mesh layers due to edge effects caused by the boundary condition at the top and bottom of the stack with free space. This is also responsible for the appearance of a half wavelength resonance corresponding to the length of the entire structure superimposed onto the

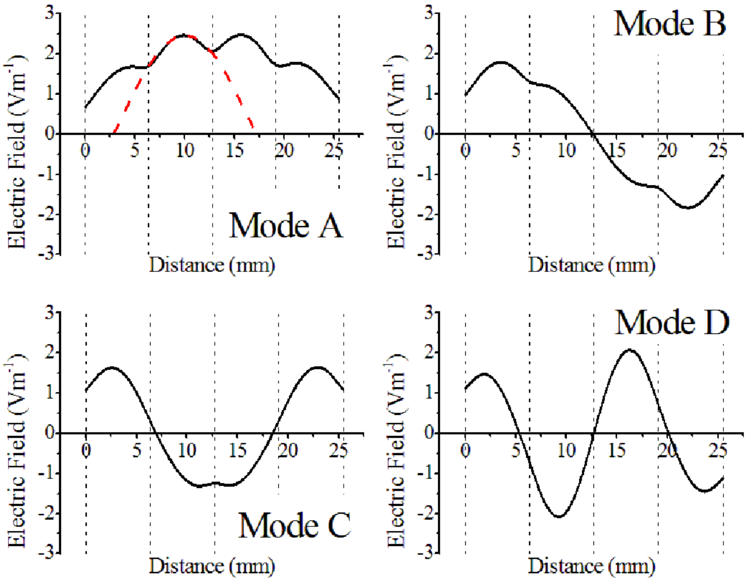

Figure 6.4: Series of four graphs, labelled mode A through mode D, representing the time-averaged electric field along a line plotted in the $z$-direction through the centre of a hole for the four transmission maxima from Figure 6.3.

electric field profile for the mode A (Figure 6.4 - top left), this effect would decrease if more unit cells where added to the stack.

The highest frequency mode (D, 12.11 GHz) approximately defines the upper band edge (Figure 6.3), with an electric field profile in the subwavelength holes of the metallic mesh layers that are *sinh*-like in character, where each passes through zero. Therefore the fields in adjacent dielectric cavities oscillate out of phase, with the majority of the cavity oscillation being excluded from the metallic mesh region (bottom right panel of Figure 6.4). Hence the highest frequency mode (D) is associated with the half-wavelength Fabry–Pérot condition (see section 2.4.2) for a single etalon, although slightly reduced in frequency due to the reduced reflectance of the metallic mesh layers.

However, it is the lowest frequency mode (mode A, 6.93 GHz) that is the most interesting, the field solution is shown in the top left panel of Figure 6.4. On resonance the electric fields in the dielectric cavities (between metallic meshes) oscillate in phase with each other, since the evanescent fields within the subwavelength holes of the metallic mesh take a *cosh*-like form. The wavelength of the mode within the dielectric cavity is much longer than simply twice the dielectric thickness because the *cosh*-like electric field removes a significant proportion of the cavity oscillation from the dielectric. This could also be described in terms of phase where the majority of a $\pi$ phase cycle, is compressed into the subwavelength holes of the metallic meshes. The effective half wavelength supported in each cavity is shown by the dashed red line, and is almost twice that shown in the profile of mode D.

The electric field profiles for modes B and C are composed of *cosine*-like profiles in the dielectric regions coupled by a combination of *cosh*-like and *sinh*-like field profiles in the subwavelength holes of the metallic mesh layers. The form of the EM fields in the metallic mesh layer determines whether the EM fields in neighbouring dielectric cavities couple in phase or out of phase with one another, thus determining the effective resonant wavelength. Mode B, (top right in Figure 6.4) supports two *cosh*-like and one *sinh*-like profiles in the metallic mesh regions, giving a longer effective wavelength than mode C that supports supports two *sinh*-like and one *cosh*-like profiles (bottom left in Figure 6.4). Due to the mixed character of the electric fields in the metallic mesh layers, for clarity, this discussion will focus on the resonant modes that occur at the transmission pass band edges.

## 6.6 Changing the Number of Unit Cells in the Stack

The numerically modelled transmission response of the structure when increasing the number of unit cells from $N = 4$ to $N = 10$ is shown in Figure 6.5. For ease of modelling frequency independent values were used for the permittivity and dielectric loss tangent being $\varepsilon = 3$ and $\tan\delta = 0.008$ respectively.

In the transmission response of the $N = 10$ structure, 10 transmission peaks are recorded, all have a reduced Full–Width–Half–Maximum (FWHM) compared to the response of the $N = 4$ structure. This occurs due to the decreasing the influence of the incident and exit faces on the resonant mode EM field profile. A stack with $N = \infty$ would have an infinite number of modes creating a square transmission band pass region, where the transmission intensity would be determined by the loss of the system. Here frequency resolution of the model limits the recorded transmission of these modes as well as the loss in the dielectric cavities. The lowest frequency mode (A) does not significantly change in frequency with the increase in the number of unit cells in the stack. For an all–dielectric stack the lowest frequency mode would have an approximate wavelength twice the optical length of the overall structure and would linearly depend on the number of repeat unit cells, however here it is the properties not the number of unit cells and in particular the geometry of the metallic mesh that dictate the frequency of the lower transmitting band edge. The small shift in frequency observed here is due to the edge effect imposing a small half wavelength resonant form over the whole structure as shown in Figure 6.4 - top left, however, this reduces as more unit cells are added to the structure.

The highest frequency mode appears to be the most affected by the addition of extra unit cells. The resonant electric field profile tends to that of a perfect half

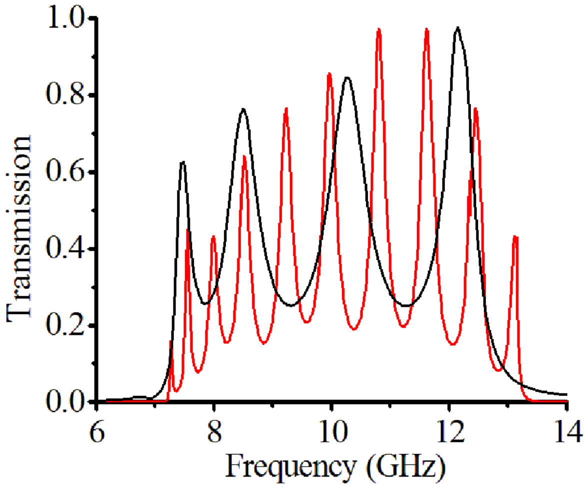

Figure 6.5: Transmission spectra for the first pass band region of two structures: the four unit cell stack (black line) and the ten unit cell stack (red line). Frequency independent permittivity $\varepsilon = 3$ and dielectric loss tangent $\tan\delta = 0.0018$ values used.

wavelength resonance in each dielectric cavity, the half wavelength mode supported between two metallic mesh mirrors separated by 6.35 mm of dielectric. The apparent shift in frequency observed in the $N = 10$ structures response corresponds to a better definition of the high frequency band edge not a significant shift in the frequency of the modes.

The overall effect of the addition of extra cavities is only to increase the number of modes within the bandwidth; the width of the transmission band is largely governed by the geometry of the unit cell as shown below.

## 6.7 Tuning the Frequency of the Transmitting Band Edges

As with the single metallic mesh layer clad in dielectric considered in Chapter 5, the upper and lower band pass edges may be controlled almost independently though a suitable choice of parameters. The low frequency modes are controlled predominantly by the metallic mesh geometry, and the high frequency modes are controlled predominantly by the properties of the dielectric. This effect is much more pronounced in this structure when compared to the dielectric clad single metallic mesh structure (Chapter 5), as the modes are well defined due to the increased reflectivity of the outer boundaries here (metallic mesh, previously dielectric), leading to the small FWHM.

To provide further clarity to the following discussion, first the influence of changing the electric field gradient at the metallic mesh–dielectric boundary on the effective wavelength will be considered. Following this the geometric changes that lead to the change in electric field gradient will be discussed.

When the gradient of the electric field at the boundary shallows, the transmission peak corresponding to mode A increases in frequency. This is due to the *cosh*-like form of the electric field becoming shallower, and therefore the electric field in the dielectric cavity has a decreased amplitude, leading to a shorter effective wavelength. By contrast the transmission peak corresponding to the higher frequency mode D, increases in frequency. As the gradient of the electric field shallows the half wavelength *cosine*-like form of the electric field in the dielectric region tends to the form of the transmission response of a PEC bounded half wavelength Fabry–Pérot cavity.

Conversely when the electric field gradient at the metallic mesh–dielectric boundary increases the hyperbolic form of the electric field in the metallic mesh layer for the lower frequency mode A, has a sharper and therefore deeper *cosh*-like form that allows a much longer effective wavelength be be supported overall. On the other hand mode D, supports a shorter effective wavelength as the sharper *sinh*-like mode decreases with the reflectivity of the metallic mesh.

### 6.7.1 Variation in the Metallic Mesh Parameters

The low frequency pass band edge is predominantly dependent on the geometry of the metallic mesh. Figure 6.6 shows the modelled response (using frequency independent permittivity and dielectric loss tangent values of $\varepsilon = 3$ and $\tan\delta = 0.008$ respectively) when changing the pitch and hole size. Varying these parameters affects the reflectivity of the metallic mesh. This has a small influence on the frequency at which the higher frequency modes occur, as the response of the metallic meshes tends towards that of a PEC, mode D increases in frequency towards the ideal half wavelength Fabry–Pérot limit. The electric field profile for mode A are highly dependent on these metallic mesh parameters.

By changing the pitch, the penetration depth (discussed in section 2.4.1.1) of the EM fields in the subwavelength holes can be varied. The transmission response of such a system is shown in Figure 6.6 for pitch $d = 5$ mm and $d = 4$ mm (solid and dashed lines respectively); reducing the pitch increases the diffraction edge that in turn reduced the decay length at this frequency. The evanescent field in the subwavelength holes couple to form a shallower *cosh*-like electric field profile, shortening the effective resonant wavelength of this mode. This has the affect of increasing the reflectivity of the metallic mesh layers.

By changing the size of the holes, the amplitude of the EM fields is varied. In Figure 6.6 (solid and dotted lines) the hole size is increased from $a = 4.85$ mm to $a = 4.9$ mm.

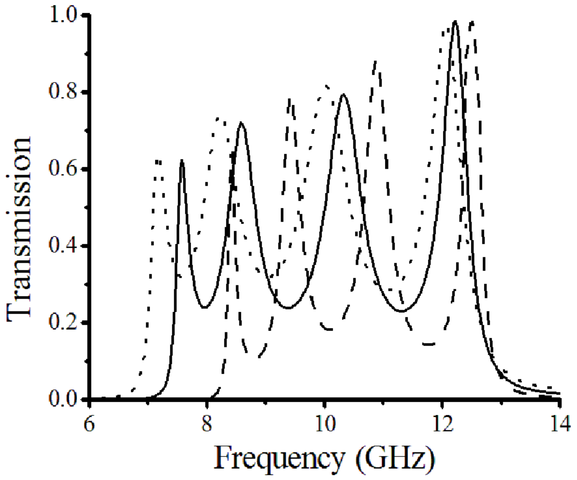

Figure 6.6: Modelled transmission response for the metallic mesh–dielectric stack using frequency independent permittivity and dielectric loss tangent $\varepsilon = 3$, $\tan\delta = 0.008$, other parameters as in section 6.3 (solid line), the dashed line represents the response when the pitch is reduced to $d = 4$ mm (previously $d = 5$ mm), and the dotted line represents the response when the hole width in the metallic mesh is increased to $a = 4.9$ mm (previously $a = 4.85$ mm).

Increasing the amplitude of the fields allows a sharper gradient at the metallic mesh–dielectric interface, (decreasing the reflectivity) and so supporting a longer effective wavelength for the whole structure.

The simplest way to tune only the low frequency pass band edge is to change the thickness of the metallic mesh. As in Chapter 5 the metallic mesh can be considered as a tunnel barrier, by changing the thickness of this barrier the form of the *cosh*-like electric field profile can be varied almost independently of the higher frequency modes where the *sinh*-like fields are small and pass through zero see section 5.5.1 for more detail. The transmission response of a system where this is considered is shown for an increase of $t_m = 18$ µm to $t_m = 100$ µm in Figure 6.7 (solid and dashed lines), with the gradient at the interface decreasing leading to a shorter effective wavelength overall.

### 6.7.2 Variation of the Properties of the Dielectric Cavity

The high frequency band edge is controlled by the properties of the dielectric cavities, where the electric field amplitude is the greatest. Figure 6.7 shows the transmission response when reducing the dielectric thickness from $t_d = 6.35$ mm to $t_d = 5$ mm. The high frequency band edge increases in frequency by almost 3 GHz, however the low frequency band edge is also increased, mode A increases by $\sim 1$ GHz. The response

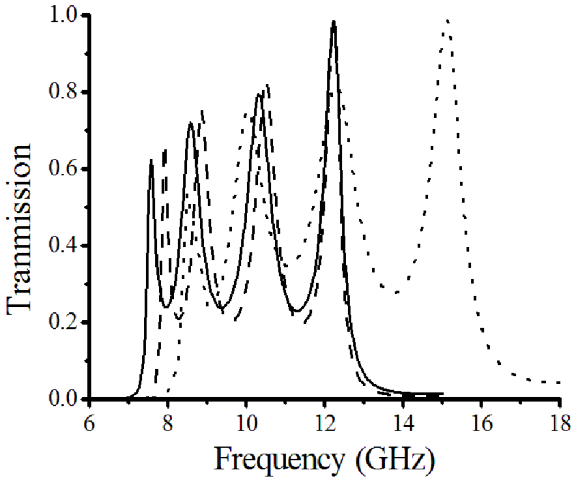

Figure 6.7: Modelled transmission response for the metallic mesh–dielectric stack using frequency independent permittivity and dielectric loss tangent $\varepsilon = 3$, $\tan\delta = 0.008$, other parameters as in section 6.3 (solid line), the dashed line represents the response when the metallic mesh thickness is increased to $t_m = 100$ μm (previously $t_m = 18$ μm) and the dotted line represents the response when the dielectric thickness is reduced to $t_d = 5$ mm (previously $t_d = 6.35$ mm).

of mode D is expected as the behaviour of this mode is similar to that of a first order Fabry–Pérot mode, the frequency of which can be tuned by varying the optical length of the cavity defined as the refractive index multiplied by the physical length. However mode A is also dependent on the optical length of the dielectric cavity, causing a shift in the resonant frequency of the lower band edge, but as the majority of the electric field is contained within the metallic mesh, the observed change in frequency is less dependent on the dielectric properties.

## 6.8 Alignment of the Metallic Meshes

Until this point the numerically modelled response of this structure assumes that the metallic meshes are all aligned in the $xy$–plane. It is now shown that translational misalignment of the meshes does not perturb the microwave response of the experimentally considered sample. Since the penetration depth of the near fields (evanescent diffracted orders) associated with each subwavelength metallic mesh layer is approximately 1 mm or less at these frequencies (as shown in section 2.4.1.1, Figure 2.10), i.e. much smaller than the spacing of the metamaterial layers ($t_d = 6.35$ mm), they do not directly interact. Of course if the thickness of the dielectric layer is reduced, or the periodicity of the array increased such that the diffracted evanescent fields interact, then transverse mesh displacement may indeed perturb the response, as shown by Taylor *et al.* in [88] for a two layer PEC metallic mesh, and in Figures 6.9 and 6.10.

The transmission response is shown for a structure where the pitch has been increased from $d = 5$ mm to $d = 10$ mm corresponding to decay lengths for the diffracted evanescent fields of 0.807 mm and 1.688 mm respectively at 10 GHz. The dielectric thickness was reduced from $t_d = 6.35$ mm to $t_d = 1$ mm, frequency invariant permittivity and dielectric loss tangent values $\varepsilon = 3$ and $\tan\delta = 0.0018$ were used, all other parameters are as in the experimental sample.

The stacked metallic mesh layers are first considered aligned (i.e. the centre of each subwavelength hole is aligned in the $z$ direction) as in Figure 6.2. The transmission response is shown as black lines in Figures 6.9 and 6.10. This is compared with the transmission response of a stack where the metallic mesh in layers $2, 3, 4$, and 5 are given a translation displacement as shown in Figure 6.8. The translation is the same for both dielectric thickness samples. The first metallic mesh (layer 1 in Figure 6.8) undergoes no displacement, the second metallic mesh is displaced by $x = -4$ mm, the third by $y = -6$ mm, the fourth by $x = y = -6$ mm, and finally the fifth mesh by $x = 4$ mm, $y = -1$ mm.

Figure 6.9 shows the transmission response for the aligned and misaligned stacks with a pitch of $d = 10$ mm is invariant until $\sim$ 17 GHz. Here the decay length of the diffracted fields outside the holes close to $\frac{1}{2}t_d$. Therefore the response under translation changes with the interaction of the evanescent fields. Note, the diffraction edge here occurs at 30 GHz.

To illustrate this point further the dielectric spacing between the metallic meshes is reduced to $t_d = 1$ mm and the transmission response again is considered for an aligned and a misaligned stack (Figure 6.10). The transmission response here is drastically different. Here the evanescent fields interact allowing a series of strong transmission modes that are dependent upon the alignment of the metallic meshes showing four strong transmission peaks when aligned, that are split into two bands of much weaker transmission peaks when misaligned.

## 6.9 The Transmission Response of the Stacked Dielectric–Metallic Mesh–Dielectric Unit Cell

Thus far the unit cell considered has resembled a single Fabry–Pérot etalon with two metallic meshes acting as partial mirrors separated by dielectric. Now consider stacking the inverse structure, where the unit cell comprises of a metallic mesh clad in dielectric of thickness $\frac{1}{2}t_d$, as investigated for a single unit cell in Chapter 5.

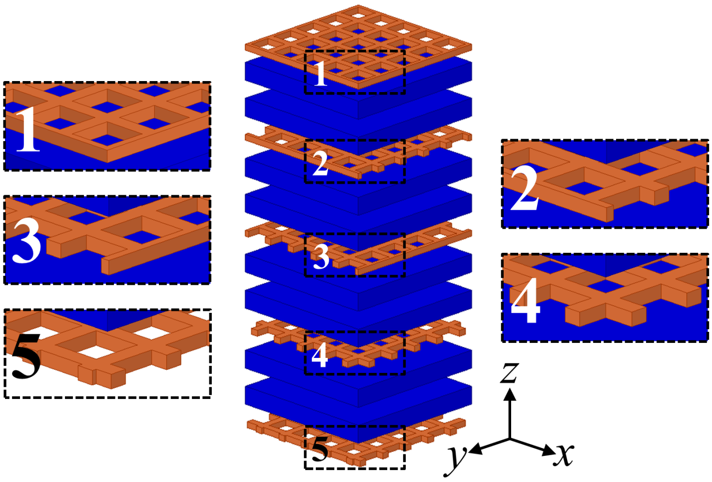

Figure 6.8: Exploded schematic of the numerically modelled metallic mesh–dielectric stack, showing misalignment of the metallic mesh layers, all parameters as in Figure 6.2 unless otherwise stated. (not to scale)

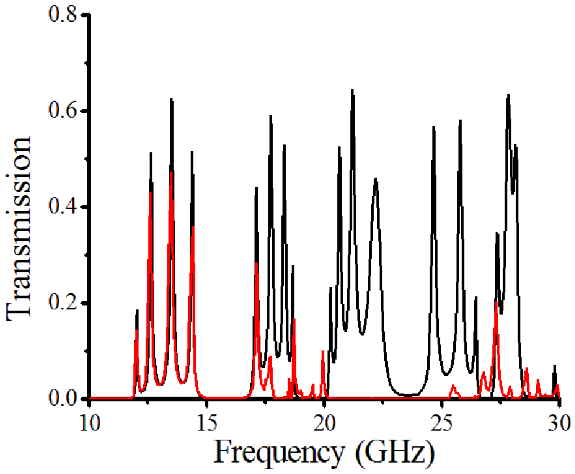

Figure 6.9: Numerically modelled transmission spectra for the first transmission band, when the metallic mesh layers of the metallic mesh–dielectric stack are aligned (solid black line) and misaligned (solid red line) in the $xy$–plane as shown in Figure 6.8, where the pitch is $d = 10$mm and the dielectric thickness is $t_d = 6.35$mm.

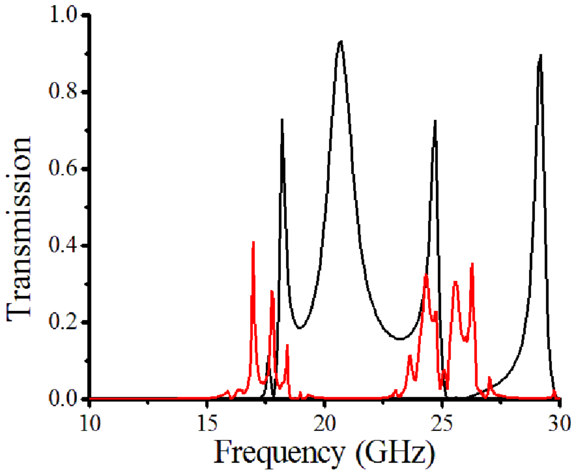

Figure 6.10: Numerically modelled transmission spectra for the first transmission band, when the metallic mesh layers of the metallic mesh–dielectric stack are aligned (solid black line) and misaligned (solid red line) in the $xy$–plane as shown in Figure 6.8 where the pitch is $d = 10$mm and the dielectric thickness is $t_d = 1$mm.

The modelled sample from Figure 6.2 is now clad in dielectric of thickness $\frac{1}{2}t_d = 3.175$ mm as shown in Figure 6.11. It is clear from the modelled transmission response shown in Figure 6.12 that the band pass region observed in Figure 6.3 (solid red line, here Figure 6.12 - solid black line) now transmits across the entire frequency range of the pass band - the discrete transmission peaks have merged together (Figure 6.12 - solid red line). This is due to the change in reflectivity of the overall structure. By decreasing the refractive index contrast at the outer boundaries of the structure, the reflection coefficient also decreases, and the previous experimentally observed transmission peaks broaden in frequency. Decreasing the reflectivity leads to a shallower gradient at the metallic mesh–dielectric boundary causing mode A to increase, and mode B to decrease in frequency, however this is countered by the broadening of the transmission peaks. Also, decreasing the overall reflection of the structure increases the transmission, this is particularly noticeable in the band gap regions.

Although a flat transmission band is not fully observed here, through optimisation of the parameters the band pass could be smoothed and increased in width by changing the optical length of the cladding as shown in Chapter 5. This technique, also known as impedance matching, has been extensively used in Frequency Selective Surface (FSS) work and is discussed in detail in ref [1, 140].

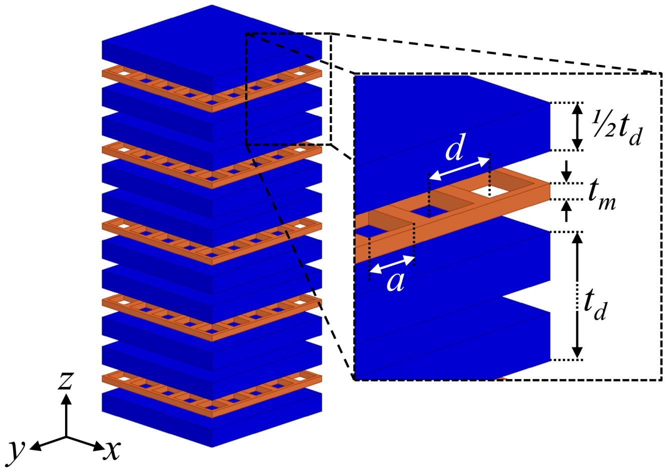

Figure 6.11: Exploded schematic of the numerically modelled clad metamaterial–dielectric stack, as before blue regions represent the low loss dielectric Nelco NX9255 of total thickness $t_d = 6.35$ mm and orange layers represent the metallic mesh of square air filled holes of pitch $d = 5$ m, hole size $a = 4.85$ mm, and thickness $t_m = 18$ µm, here the dielectric cladding added to the top and bottom of the stack is of thickness $\frac{1}{2}t_d = 3.175$ mm. (not to scale)

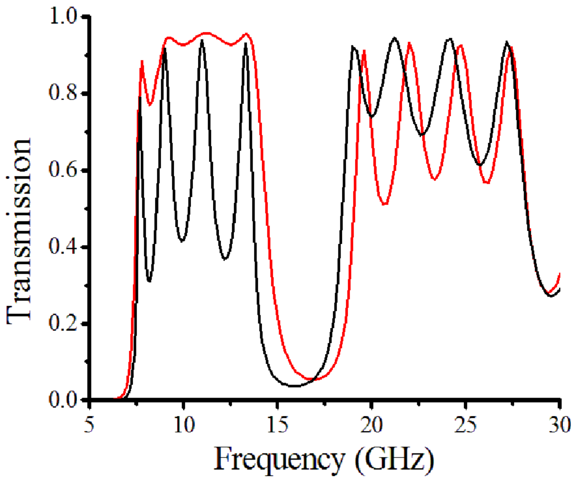

Figure 6.12: Transmission spectra for the first and second pass band region of two structures: the original metallic mesh–dielectric stack (black line) and stack clad in dielectric of thickness $\frac{1}{2}t_d$ (red line). Modelled using a frequency independent permittivity $\varepsilon = 3$ and dielectric loss tangent $\tan\delta = 0.0018$.

## 6.10 Concluding Remarks

Novel experimental observations of the transmission bands in the microwave response of a metallic mesh–dielectric multilayer stack have been presented. As the metallic mesh has an effective permittivity dominated by the negative real part, the frequency of the transmission band edges are mainly determined by the form of the evanescent field distribution in these metamaterial layers, that can take either a hyperbolic cosine or hyperbolic sine form. For the hyperbolic sine case, the fields within the subwavelength holes of the metallic mesh are small and pass through zero and the electric field in adjacent dielectric cavities oscillate out of phase. Therefore the high frequency band edge is in close agreement with that expected for a single Fabry–Pérot etalon of the thickness of the dielectric, and has a very weak dependence on the overall length of the structure. However when the fields in the subwavelength holes of the metallic mesh are of hyperbolic cosine form a significant proportion of the cavity oscillation is removed from the dielectric and each dielectric cavity supports a standing wave of wavelength much longer than its optical length. Furthermore, the frequency of the lower band edge is almost completely independent of the number of unit cells but is highly tunable by appropriate design of the geometrical properties of the metallic mesh. Therefore it is possible that when the thickness of the metallic meshes are reduced, the resonant wavelength of the low frequency mode will become larger than the thickness of the entire structure.

# Chapter 7

# Microwave Reflectivity of an Alternating Metamaterial Stack

## 7.1 Introduction

In this chapter the microwave response of a metamaterial–dielectric stack is experimentally and numerically investigated. The metamaterial layers are formed of dissimilar metallic meshes that alternate through the stack. By varying the thickness of the metallic meshes in the stack, the reflection band stop region can be significantly altered, with the creation of band gaps and a defect mode. Here the reflection response of a stack composed of a half integer number of unit cells is used to show this phenomenon. An analogy is drawn between quantum mechanical tunnel barrier systems and this metamaterial–dielectric stack, with a view to discussing the defect mode as a topological state.

## 7.2 Background

Much work described in previous chapters has considered metal–dielectric stacks, and metallic mesh–dielectric stacks in both the optical and microwave regimes. Here the unit cell of the experimentally investigated structure contains two dissimilar metallic meshes separated by dielectric. Most experimental and numerical studies using dissimilar patterned metallic structures have used electrically connected and disconnected structures in alternating layers, such as that described in Chapter 5 (see Hou *et. al.* [104] and others [141–144]). Here two dissimilar but electrically connected metallic structures are considered in each unit cell.

In the mid-1990's the electromagnetic (EM) response of the "wood pile" or "layer-by-layer" photonic band gap structure was investigated. Originally this structure,

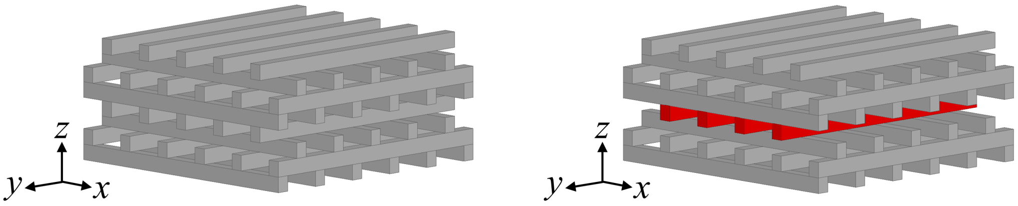

(a) (b)

Figure 7.1: Schematic of the "wood pile" or "layer-by-layer" structure. Metallic rods are placed parallel to one another and rods in neighbouring layers are at 90° to one another. The lower structure contains the defect layer (indicated in red) where a single rod is removed from the structure.

shown in Figure 7.1, was constructed of dielectric rods, as in [145–147], and later using metallic rods [148–151]. More interesting to this discussion was the introduction of "defect" layers in alternating layers of the stacks. In reference [152], Ozbay *et al.* used layers of square-cross sectional rods arranged parallel to one another in the plane and at 90° to neighbouring layers. The "defect" layers contained fewer rods leading to an $ABCB$ structure, described as a "tetragonal crystal" (compared to the "face-centred-tetragonal crystal" with no defects). (Note these metallic rods were closely spaced and therefore do not support the same electric field profiles as shown in the experimental measurements of this chapter). A defect mode is shown to occur in the "metallicity" gap, or band gap that extends from DC to the cut–off frequency associated with the gaps between the rods acting as waveguides. Below the cut off frequency the defect mode occurs when the exponentially decaying EM fields in the stack couple together to allow transmission. Later it was shown that the frequency and quality factor of the defect mode is dependent upon the filling fraction and layer separation [153], where the quality factor is defined as the ratio of the resonant frequency divided by the Full-Width-Half-Maximum (FWHM).

McCalmont *et al.* were one of the first groups to use subwavelength square metallic meshes instead of rods [154]. Three metallic meshes were closely spaced with low loss dielectric, such that no Fabry–Pérot modes were observed within the experimental frequency range. In this study defects were introduced to the second layer by removing square sections of the metallic mesh. The quality factor of the defect modes was shown to be a function of the "defect radius", that is equivalent to the filling fraction of the metallic mesh.

In this chapter the form and evolution of the "defect mode" is explored. Instead of changing the filling fraction by removing rods or sections of the mesh, the thickness of the metallic meshes in the stack are varied. Both methods dictate the evanescent decay length of the EM fields through the subwavelength holes of the metallic meshes. The reflection response is experimentally recorded for an alternating metamaterial–dielectric stack, the results of which are used to validate the numerical model that provides insight into the form of the electric fields inside the structure and the origin of the defect mode that occurs in the band gap region. The exponential decaying electric field profile is shown be a surface state. Using a half integer number of unit cells means that this structure is symmetric about its midpoint which becomes important when the EM response is discussed in terms of topology in section 7.8.

## 7.3 Experimental Sample and Setup

The experimental sample consists of a stack of 3.5 unit cells, each composed of three layers labelled $A$, $B$, and $C$, arranged in the order: $ACBC$. Layers $A$ and $B$ correspond to metallic meshes of thickness 0.55 mm $\pm$ 0.1 mm and 2.4 mm $\pm$ 0.3 mm respectively. These metallic meshes are formed by stamping square holes through solid aluminium plates (this metal is assumed to be a perfect electrical conductor (PEC) at microwave frequencies). Both metallic meshes have a square pitch of $d = 7.6$ mm $\pm$ 0.2 mm and a hole size $a = 6$ mm $\pm$ 0.2 mm. The thicker metallic mesh $B$ is constructed from two metallic meshes each 1.2 mm thick, held together with a thin layer of epoxy, leading to a larger error associated with the thickness parameter.

An exploded schematic of the experimental sample is shown in Figure 7.2. When illuminated with microwave radiation between 12 and 20 GHz the metallic meshes act as a series of below cut–off waveguides, supporting only evanescently decaying diffracted fields in the subwavelength holes as described in section 2.4.1.1. Layer $C$ is a dielectric spacer layer that separates layers $A$ and $B$. In the experimental sample the metallic meshes are free standing and metallic spacers used around the edge of the sample to maintain an air spacing of 7.5 mm with an associated error of ± 0.1 mm at the spacers, and estimated ± 0.5 mm across the metallic mesh due to bowing.

The experimental configuration is designed to illustrate the splitting of a band stop region and the formation of a defect mode. In this instance the sample was investigated in reflection, as transmission samples exhibited significant bowing that worsened with increasing numbers of metallic mesh layers. This caused large variations in the dielectric separation between the metallic meshes ($t_d = 7.5$ mm $\pm 2$ mm across the sample). This problem also occurs in reflection but to a much lesser extent. The experimental and numerical results in the previous Chapter 6 show the transmission band pass regions containing a series of highly transmitting peaks, where the structure supports resonant modes allowing large transmission and almost zero reflection. Here the inverse of the

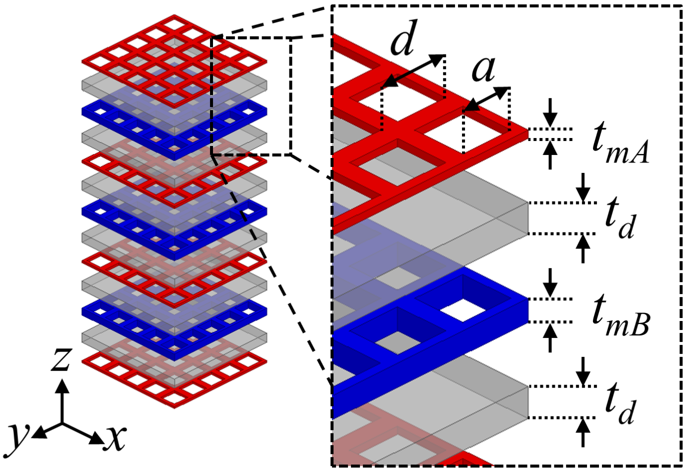

Figure 7.2: Exploded schematic of the experimental sample. An enlarged section shows the dimensions of the structure where the pitch $d = 7.6$ mm, hole size $a = 6$ mm, and dielectric thickness (air) $t_d = 7.5$ mm. The dissimilar metallic meshes, $A$ and $B$, are shown in red and blue of thickness $t_{mA} = 0.55$ mm and $t_{mB} = 2.4$ mm respectively.

transmission band pass regions, the reflection band stop regions are measured that contain a series of minima which will be investigated.

In order to measure the reflection response of this sample a collimated plane wave of TE (or s-polarised) radiation was incident on the sample surface at $\theta = 10^\circ$ (relative to the normal). As for the transmission experiments discussed in previous chapters, the collimated beam was produced using a waveguide horn placed at the focus of a spherical mirror. The reflected beam was collected using a secondary mirror with a detector horn at its focal point. Due to the transmission properties associated of the sample, it was placed 50 cm above sheets of pyramidal absorber to reduce reflection from the bench on which the reflection setup is mounted. For details of the reflection setup see section 4.4. The normalised signal is recorded (via a scalar network analyser) and shown later in Figure 7.4.

## 7.4 The Response of a Metallic Mesh–Dielectric Stack with Identical Thickness Metallic Meshes

As way of an introduction to understand the results consider the response of a stack containing unit cells where layer $A$ is identical to layer $B$ (i.e. thickness, pitch, hole size). If the stack contains $N = 3.5$ $ACBC$ unit cells, which is equivalent to $N = 7$ $AC$ unit cells. The numerically modelled reflection response of this structure is shown

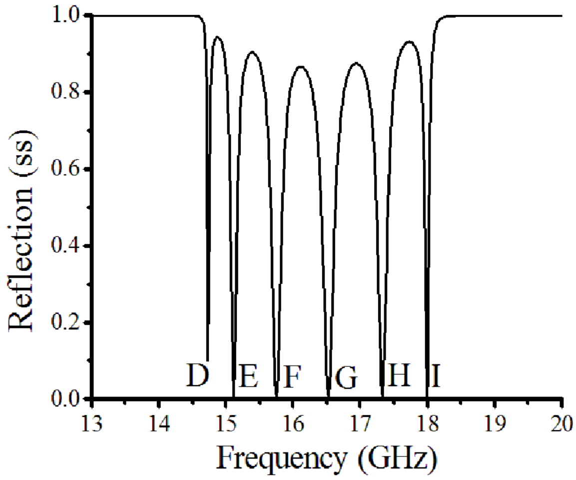

Figure 7.3: The numerically modelled reflection response for TE polarised radiation incident at $\theta = 10°$ of a $N = 3.5$ $ACBC$ unit cell stack where layers $A$ are identical to layers $B$. The parameters used in the model where: pitch $d = 7.6$ mm, hole size $a = 6$ mm, dielectric thickness (air) $t_d = 7.5$ mm and the thickness of both metallic meshes $t_{mA} = t_{mB} = 1.5$ mm.

in Figure 7.3 where the stop band comprises of six reflection minima. This model uses all the parameters stated in section 7.3 except the metallic mesh thickness, here both metallic mesh layers $A$ and $B$ are of thickness $t_{mA} = t_{mB} = 1.5$ mm. The reflection minima are referred to by letter where $D$ corresponds to the lowest frequency reflection minimum, and $I$ is the highest frequency reflection minimum as shown in Figure 7.3.

As described in Chapter 6 the effective wavelength of each resonant mode is dictated by the form of the electric fields in the metallic mesh layers. The lowest frequency resonant mode, mode $D$, supports an electric field profile that is hyperbolic cosine or *cosh*-like in this region, together with the half wavelength-like profiles that couple in phase via the evanescent field in the subwavelength holes of the metallic mesh. Consequently this mode has a long effective wavelength and is highly dependent on the geometry of the metallic mesh. The highest frequency resonant mode, referred to as mode $I$, supports a *sinh*-like mode in the metallic meshes, passing through zero, therefore adjacent dielectric cavities couple via the evanescent electric fields in the metallic mesh to oscillate out of phase with one another. The highest frequency resonant mode resembles the first order half-wavelength Fabry-Pérot mode of each dielectric cavity, and so the response is dominated by the properties of the dielectric cavity with the metallic mesh changing only the reflectivity of the cavity walls [108, 155].

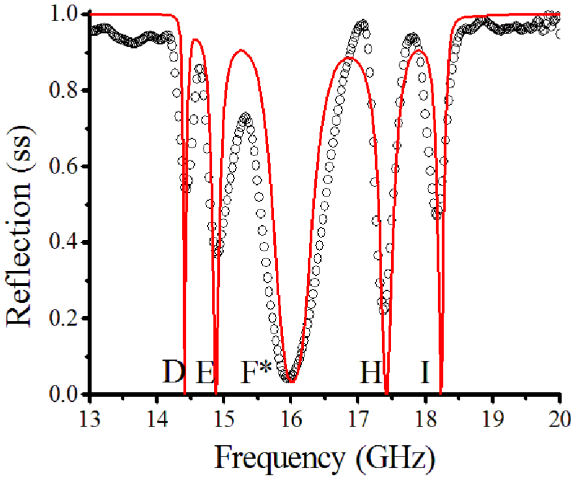

Figure 7.4: The experimentally recorded (black circles) and numerically modelled (red line) reflection response at $\theta = 10°$ of a $N = 3.5$ $ACBC$ unit cell stack where layers $A$ is not identical to layer $B$.

## 7.5 The Reflection Response of Alternating Dissimilar Thickness Metallic Mesh–Dielectric Stack

When the thickness of metallic meshes $A$ and $B$ are not equal to one another the response changes, opening a band gap at the centre of the stop band and in certain cases forming a defect mode. Figure 7.4 shows the experimentally recorded reflection response (black circles) for TE (s) polarised radiation at $\theta = 10°$. Five reflection minima are recorded, two minima ($D$, $E$, and $H$, $I$) occurring either side of a broader minimum which occurs at 16.01 GHz, labelled $F*$. The numerically modelled response (red line) was produced using an FEM model with parameters: pitch $d = 7.6$ mm, hole size $a = 6.15$ mm, dielectric thickness (air) $t_d = 7.5$ mm, metallic mesh $A$ thickness $t_{mA} = 0.8$ mm and metallic mesh $B$ thickness $t_{mB} = 2.0$ mm as defined in Figure 7.2.

It is clear that not all the parameters used to produce this numerical fit to the experimentally recorded results are within the tolerances measured from the experimental sample. Those that vary from the measured parameters are the hole size and the metallic mesh thicknesses. Increasing the hole size has the affect of increasing the bandwidth of the stop band, by reducing the frequency position of the lower frequency reflection minima, and to a lesser extent increasing the frequency position of the higher frequency modes, by changing the reflectivity of the metallic mesh mirrors bounding each resonant cavity as discussed in section 6.7.1. The number of reflection minima in each stop band is determined by the difference between the parameters of the alternating metallic meshes, as will be shown below. However, in this numerical fit the values used for the thickness of the metallic mesh layers $A$ and $B$ were outside the thickness tolerances of the metallic mesh.

Although it is still unknown why the modelled parameters for the metallic meshes are outside the tolerances measured, two suggestions are discussed that may be responsible. The first is the variation in spacing between the metallic meshes across the sample. This variation would change the Fabry–Pérot like mode between the metallic meshes, making both metallic meshes appear thicker, moving the whole band pass up in frequency. This increase in the effective thickness is observed for metallic mesh $A$, however, the modelled metallic mesh $B$ parameter decreases in thickness.

Secondly, the construction of metallic mesh $B$ from two thinner metallic meshes held together with epoxy is discussed. While every care was taken to perfectly align the metallic meshes using location pins to hold the metallic meshes in the correct position during construction, a small offset between would create smaller holes. Reducing the hole size has the same affect as decreasing the thickness of the metallic mesh, therefore this could be partly responsible. However, the main suggested cause of the decreasing in effective thickness is the layer of epoxy. As with the misalignment, every care was taken to apply as thin as layer as possible. However it is known that when the electric field inside a metallic bounded cavity becomes high, some absorption is observed into the metal. Here instead of the metallic mesh allowing fields to penetrate the surface, the layer of epoxy may be acting as an absorber, making the metallic mesh appear much thinner than it's physical size.

The FWHM of each reflection minimum is also greater in the experimental results when compared to the response predicted by the numerical model. This broadening is due to the imperfection in the wave fronts of the radiation incident on the sample. As discussed in Chapter 4, the collimating mirrors are spherical as opposed to being parabolic forming a collimated plane wave from a source, that may lead to spherical aberration. However, here it is the nature of the source, that is assumed to be a point source, that is responsible. In reality the waveguide horn emits a more Gaussian beam profile causing a small divergence in the resultant beam. This leads to a range of angles $\theta = 10^\circ \pm 2^\circ$ impinging on and being detected from the sample. This is known as beam spread, and manifests itself as an increase in the FWHM of the experimentally observed reflection minima.

Using the numerical model it is interesting to plot the electric fields along a line through the alternating metallic mesh and dielectric layers of the stack in the propagation (z) direction at the resonant frequencies. These electric field profiles are shown in Figure 7.5. Modes $D$, $E$, $H$, and $I$ are as expected considering the work discussed in Chapter 6. It is mode $F*$, the broad defect mode, that is the most interesting. The

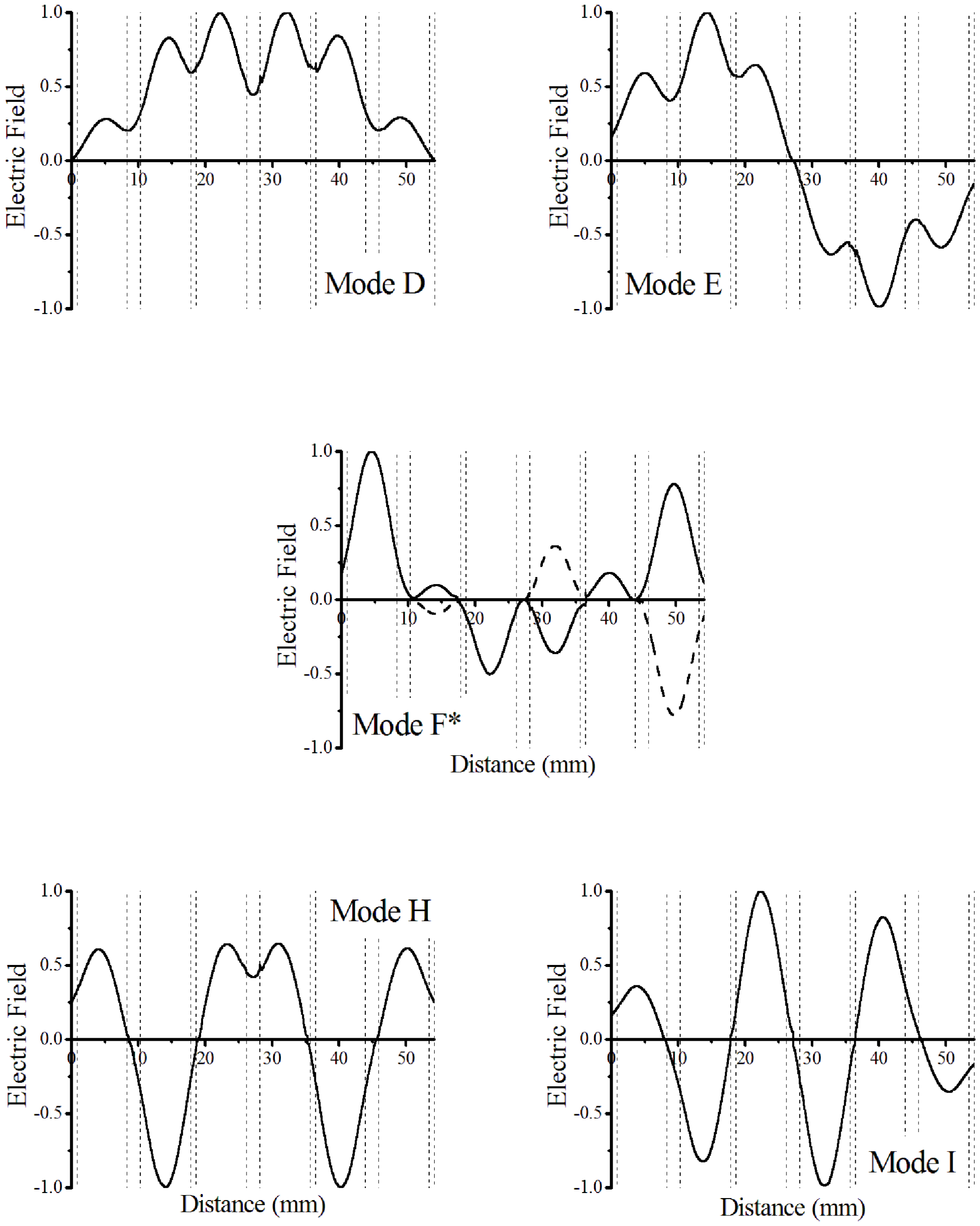

Figure 7.5: The numerically modelled complex magnitude of the electric field profiles for the reflection minima shown in Figure 7.4 (red line) labelled $D, E, F*, H, I$. The normalised complex magnitude taken at a phase corresponding to the maximum field enhancement.

electric field profile of mode $F*$ shows characteristics expected for both modes $F$ and $G$ at different points in the $2\pi$ phase cycle.

The electric field profile for mode $F$ (similar to the solid black line in Figure 7.5 Mode $F*$), would show that fields in pairs of cavities oscillate in phase via a *cosh*-like electric field profile in the metallic mesh region, with *sinh*-like modes coupling cavities through the second and third metallic mesh $A$ layers to oscillate out of phase. Whereas the electric field profile for Mode G (similar to the dashed black line in Figure 7.5 Mode $F*$), would show three *sinh*-like electric field profiles occur in the corresponding three metallic mesh $B$ layers with the second and third metallic mesh $A$ layers now supporting *cosh*-like electric field distributions. The magnitude of both of these modes would be symmetric about the centre of the stack in the propagation direction.

The electric field profile for mode $F*$ is not symmetric about the centre of the stack. It is exponential, where the rate of decay increases as the reflectivity of the mode increases (and the transmission reduces). This indicates that the electric field is greatest at the incident surface, suggesting a bound surface state between the first metallic mesh layers $A$ and $B$.

## 7.6 Variation of the thickness of the Metallic Meshes

To understand the origin of this mode, the evolution from identical to dissimilar metallic mesh thicknesses is considered, here yielding substantially different results when one metallic mesh thickness (layer $A$ or $B$) is reduced compared to the other, as shown in Figures 7.6 and 7.7. To undertake this a series of numerically modelled reflection responses were obtained for metamaterial dielectric stacks with varying metallic mesh thicknesses using parameters as stated in section 7.3. The metallic mesh thicknesses are both initially set to be equal at $t_{mA} = t_{mB} = 1.5$ mm.

### 7.6.1 Reducing the Thickness of Metallic Mesh Layer B

First consider Figure 7.6 where the thickness of the metallic mesh in layer $A$ is kept constant at $t_{mA} = 1.5$ mm while the thickness of metallic mesh in layer $B$ ($t_{mB}$) decreases. Figure 7.6 shows the numerically modelled reflection response for $t_{mB} = 1.5$ mm, $t_{mB} = 1$ mm, and $t_{mB} = 0.5$ mm (black dashed, solid red, and solid blue lines respectively). As the thickness of metallic mesh layer $B$ decreases modes $D, E, F$ and $G, H, I$ separate forming two sub-band stop regions each containing three reflection minima. As the thickness reduces further the system tends to the limit where $t_{mB} = 0$, so the stack will contain four metallic meshes of thickness $t_{mA}$, separated by twice the dielectric thickness ($2 \times t_d$). The double thickness dielectric layers reduce the position

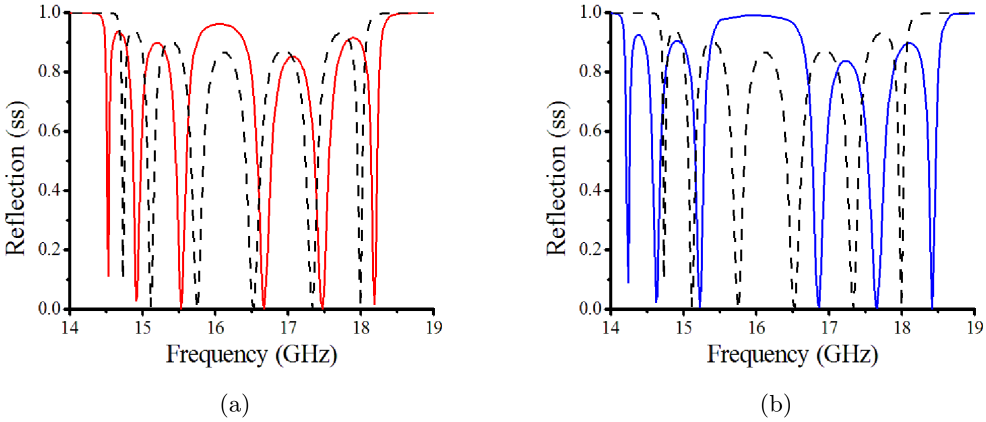

(a)

(b)

Figure 7.6: The numerically modelled reflection spectra when $t_{mA} = 1.5$ mm is kept constant and $t_{mB}$ is varied from $t_{mB} = 1.5$ mm (black dashed line) to (a) $t_{mB} = 1$ mm (solid red line) and (b) $t_{mB} = 0.5$ mm (solid blue line), all other model parameters are as the experimental sample described in section 7.3.

of the reflection minima, $D, E, F$ that continue to support the half wavelength resonant condition in the double thickness dielectric cavity. Whereas the three higher frequency reflection minima $G, H, I$ move to higher frequencies to support a whole wavelength in each double thickness dielectric cavity.

The formation of the reflectivity band gap when the metallic mesh layer $B$ thickness is decreased is due the splitting of the stop band region (containing six reflection minima) into two bands (each containing three reflection minima) which in the limit $t_{mB} \rightarrow 0$ becomes the first and second band stop regions, where the electric field profiles support a half wavelength and a full wavelength in each metallic mesh bounded dielectric cavities respectively.

### 7.6.2 Reducing the Thickness of Metallic Mesh Layer A

Now consider a stack where the thickness of metallic mesh layer $B$ is kept constant at $t_{mB} = 1.5$ mm, and the thickness of metallic mesh layer $A$ is reduced. Figure 7.7 shows the numerically modelled transmission response where $t_{mA} = 1.5$ mm, $t_{mA} = 1$ mm, $t_{mA} = 0.5$ mm , and $t_{mA} = 0.1$ mm (black dashed, solid red, solid blue lines and solid green lines respectively). As the thickness of metallic mesh layer $A$ decreases, reflection minima $F$ and $G$ merge together to form a composite electric field profile shown in Figure 7.5 Mode $F*$. As the thickness decreases further the amplitude of the electric field for the defect mode reduces exponentially, therefore increasing the reflectivity, leaving a band gap in between two sub–bands each containing two reflection minima

$D$, $E$ and $H$, $I$.

As the stack contains one less metallic mesh layer $A$ than $B$, when thickness of metallic mesh layer $A$ tends to zero, the stack will contain three metallic mesh $B$ layers separated by twice the thickness of dielectric. Then only two reflection minima are expected in each reflection band stop region. As before, the higher frequency reflection minima increase a small amount in frequency while the lower frequency reflection minima substantially reduce in frequency. The lower frequency band (containing modes $A$ and $B$), supports half wavelength resonant modes in each dielectric cavity, whereas the higher frequency band supports a full wavelength resonant mode in each dielectric cavity. Each of the two new bands contains two reflection minima relating to two resonant modes: one supporting a *cosh*-like and a second supporting *sinh*-like electric field profile in the central metallic mesh.

In summary the defect mode $F*$ experimentally observed in Figure 7.4, is formed by the reflection minima $F$ and $G$ merging into a composite mode. As the structure's response becomes dominated by metallic mesh layer $B$ when increasing it's thickness (or equally decreasing metallic mesh layer A's thickness), the defect mode is created, and two sub–bands form either side, each containing two reflection minima. As metallic mesh layer $A$ tends to zero thickness the reflection intensity of the defect mode increases, forming a band gap region between the two sub–bands. On the other hand, when the structure's response becomes dominated by metallic mesh layer $A$ when increasing it's thickness (or decreasing metallic mesh layer $B$'s thickness), the band separates into two sub–bands each containing three resonant modes, so no defect mode occurs.

## 7.7 Tunnel Barrier Analogy

As discussed in Chapter 5 the EM transmission response through a subwavelength metallic mesh is analogous to the quantum mechanical tunnel barrier system. In this section each metallic mesh layer is considered as a tunnel barrier with an equivalent potential. The dielectric spacing is considered the same as the semi-infinite incident and exit media. The tunnel barrier height, that corresponds to the potential associated with each metallic mesh layer, is a function of the geometry of the metallic mesh dictated by the pitch, hole size and thickness. In this investigation, the thickness of the metallic mesh has been varied, however it is equally productive to consider the variation in pitch, or as Taylor has investigated in [89] (using effective medium theory), consider the variation in hole size.

Figure 7.8 shows three diagrams that are the EM equivalent to the quantum mechanical potential diagrams. The first, Figure 7.8 (a) is for a structure where layers $A$ and $B$ are identical, yielding six tunnel barriers of equal height. The height of the first

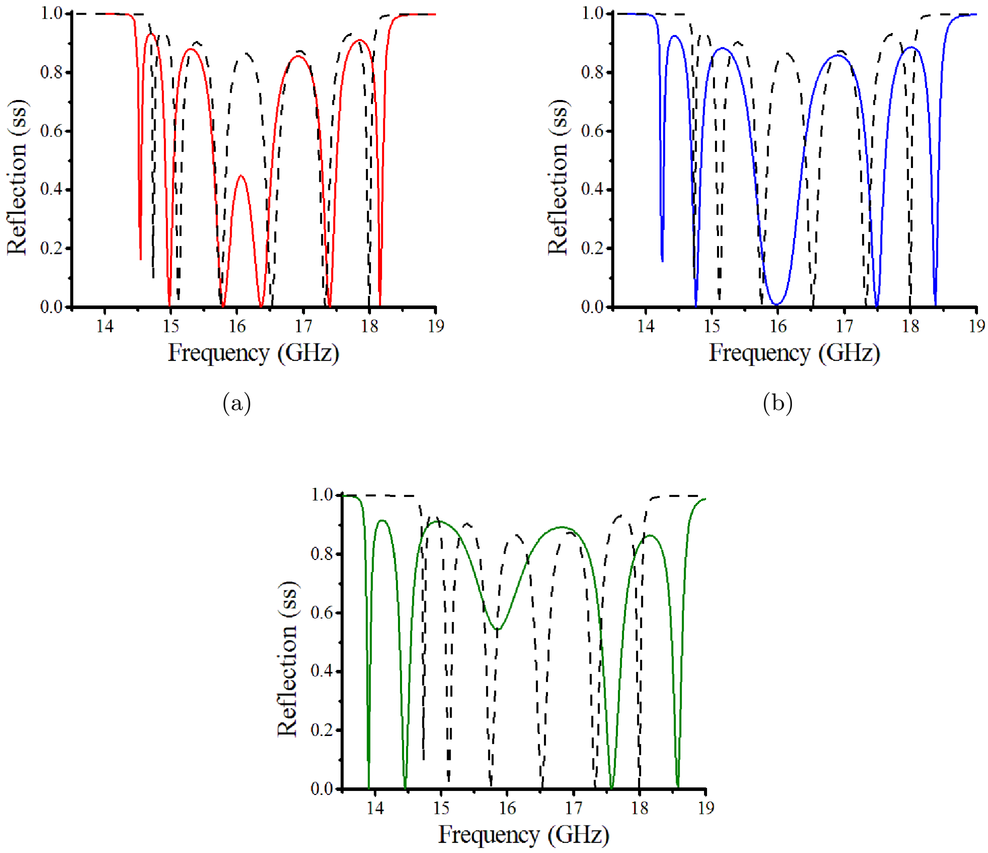

(a)

(b)

(c)

Figure 7.7: The numerically modelled reflection spectra when $t_{mB} = 1.5$ mm is kept constant and $t_{mA}$ is varied from $t_{mA} = 1.5$ mm (black dashed line), to (a) $t_{mA} = 1$ mm (solid red line), (b) $t_{mA} = 0.5$ mm (solid blue line) and (c) $t_{mA} = 0.1$ mm (solid green line), all other model parameters are as the experimental sample described in section 7.3.

and second tunnel barrier at the interface determines whether the system has an repulsive or attractive potential. To have an attractive potential there must be a negative potential inside the surface. Figures 7.8 (b) and 7.8 (c) represent the equivalent potential diagrams for the symmetric structures where $t_{mA} < t_{mB}$ (experimentally observed and numerically modelled) and $t_{mA} > t_{mB}$ (numerically modelled) respectively. Here both the incident and exit faces share the same potential with Figures 7.8 (b) and 7.8 (c) having attractive and repulsive potentials respectively. Note that it is the structure with attractive potentials on the incident and exit interfaces of the stack that supports the defect mode.

## 7.8 Topological Insulator Analogy

The attractive potential in this structure has been identified as a requirement when observing the physical realisation of a topological insulator state. Topology is the mathematical study of systems that can't be altered by stretching. It covers many physical research areas from geometrical objects to the movement of an electron gas and symmetry groups [156].

Atherton and Mathur [157, 158] predicted that to observe a topological insulator mode physically, a system possessing an attractive potential was required. The attractive potential creates at least one bound state in the band gap region. Using a photonic system to create such a structure may be possible. Although an in-depth discussion on the concept of topological insulators is not considered here, the experimental and numerical reflection response shown here represents a continuous transformation in the thickness of alternate metallic meshes (from identical to dissimilar), with the response showing the formation of the defect mode. This work may lead to advancements in the search for the physical realisation of this topological state.

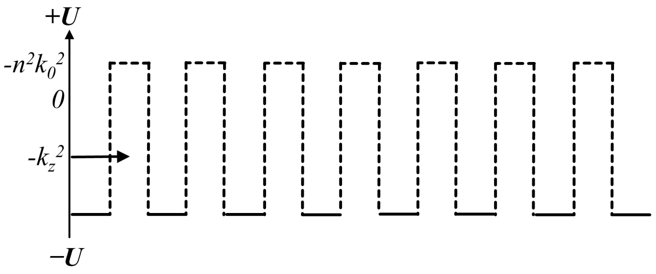

(a)

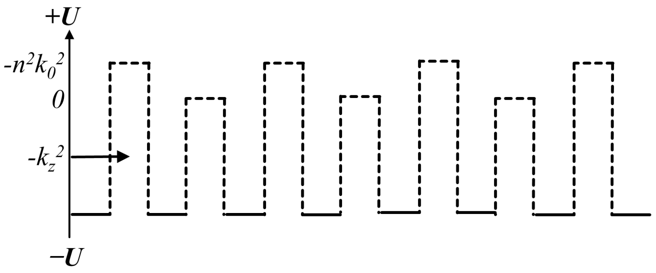

(b)

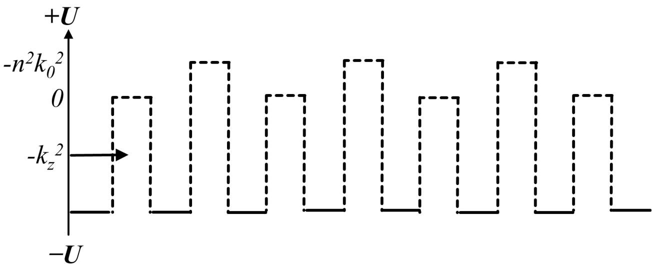

(c)

Figure 7.8: The EM equivalent of the potential diagram in quantum mechanics. The arrow indicates the incident potential, and the dashed lines indicate the position of the tunnel barriers. (a) Tunnel barriers of equal height for a metamaterial–dielectric stack where all the metallic meshes are identical. (b) Tunnel barriers of alternating height for a metamaterial–dielectric stack where the thickness of metallic mesh $A$ is greater than metallic mesh $B$. (c) Tunnel barriers of alternating height for a metamaterial–dielectric stack where the thickness of metallic mesh $A$ is less than metallic mesh $B$.

## 7.9 Concluding Remarks

In this chapter the EM response of a metallic mesh–dielectric stack has been experimentally and numerically investigated using a unit cell comprising of two dissimilar metallic meshes spaced by dielectric. The evolution from identical to dissimilar thickness metallic meshes was shown for a metamaterial–dielectric stack containing $N = 3.5$ $ACBC$ unit cells. When the metallic meshes are of equal thickness the $N = 3.5$ $ACBC$ unit cell structure supports a series of six resonant modes that allow transmission, and no reflection. However when the metallic meshes are dissimilar the structure is symmetric about this midpoint. As the metallic mesh thickness in layer $A$ becomes smaller than that of layer $B$ the three resonant modes that support the longest effective wavelengths reduce in frequency creating a band gap in between the six reflection minima. In this quantum mechanical tunnel barrier analogy this structure exhibits a repulsive potential on both faces. In contrast as the thickness of the metallic mesh in layer $A$ becomes greater than that of layer $B$ the central two reflection minima $F$ and $G$ merge and the resulting mode, mode $F*$, increases in reflection intensity forming the band gap region. The merging of these transmission peaks creates a defect mode that has been identified as possibly being the physical realisation of a topological state that may occur for a quantum mechanical tunnel barrier system with an attractive potential.

# Chapter 8

# Rotated Hole and Patch Arrays for Polarisation Conversion

## 8.1 Introduction

In this chapter a new type of chirality is demonstrated at normal incidence by employing two isotropic layers formed of non-chiral elements. Each layer is simply comprised of identical square arrays of subwavelength square metallic meshes (hole arrays) or patches. The holes or patches are arranged with their sides parallel to the axes of the square lattice, and are placed in close proximity with the axes of one array rotated relative to the other. The layers are aligned parallel to one another, and spaced such that, at frequencies below the onset of diffraction, they are situated within a decay length of each other's evanescent diffracted fields.

## 8.2 Chirality in Nature and Man–made Structures

Chirality is determined by the symmetry, or lack thereof, of a structure. The most obvious example of chirality is the symmetry of our hands. The left and right may be identical to their mirror image, however one cannot be translated to become the other. Lord Kelvin described chirality in 1904...

> "I call any geometric figure, or group of points, chiral, and say it has chirality, if it's image in a plane mirror, ideally realised, cannot be brought to coincide with itself." [159]

One of the most abundant chiral objects in nature are chiral molecules. A small selection of these is given in table 8.1.

| Object | Left hand | Right hand |
|---|---|---|
| Screws | Left helix | Right helix |
| Proteins | Used by the body | Rejected by the body |
| Carbohydrates | Rejected by the body | Used by the body |
| Sugars | Rejected by the body | Used by the body |
| Limonene | Lemon smell | Orange smell |
| Carvone | Caraway seed smell | Spearmint smell |

Table 8.1: Left and right handed objects

One example of the affects of chirality, with shocking consequences was observed worldwide. Synthesized in 1954 in West Germany and licensed to 46 countries, Thalidomide was a sedative advertised as helpful in treating anxiety, insomnia, and tension. It was described as safe for pregnant women and prescribed as a treatment for morning sickness [160–162]. In the 1960s medical research drew a correlation between Thalidomide when used in the first trimester of pregnancy and children born with teratogenic (abnormalities in physiological development) and peripheral neuropathic conditions (damage to nerves outside the brain and spinal chord) [163–165]. Thalidomide was removed from commercial sale in 1961, however it is estimated that more than 10,000 children were affected [161, 166]. The Thalidomide molecule has two chiral optical isomers being mirror images of one another. The 'S' optical isomer was found to be teratogenic, and the 'R' optical isomer was found to be a powerful sedative [167, 168]. The Thalidomide tragedy led to much stricter testing being imposed on drugs and pesticides before they could be licensed.

Another example of chirality existing in natural systems is in the structure that forms the carapase of some vividly coloured beetles such as Chysina Gloriosa [169], Eurpholus Magnificus [170], and Plusiotis Boucardi [171], many more can be found in [172]. Here 3D photonic crystals have naturally evolved over more than 500 million years into twisted multilayer systems, arranged in a helical form. Visible light interacts with these 3D photonic chiral structures to produce bright iridescent colours. It has also been found that these structures give a different response for different handed circularly polarised light. Structures that are electromagnetically (EM) chiral give rise to selective reflection or transmission of one specific circular polarisation state of EM radiation, and may induce rotation of the plane of polarisation on transmission or reflection.

The amount of rotation produced by a structure can vary according to many variables. Sugar solution, for example, gives rise to rather weak rotations of polarisation when illuminated with visible light, due to the intrinsic chirality of the sugar molecules

[173]. The molecules all have the same handedness even when viewed from different positions, therefore an ensemble of randomly orientated sugar molecules (such as in a sugar solution) will have a net handed response. Fructose molecules are left handed, and so will have different refractive indices when illuminated by right and left hand circularly polarised light. If linearly polarised light, made up of equal right and left handed polarised light, illuminates the same sample, the transmitted radiation would be elliptically polarised, as the left hand circularly polarised component would travel faster through the sample than the right [174].

Anisotropic (uniaxial) liquid crystals, are made up of rod shaped molecules that can flow like a fluid. By treating the surfaces containing the liquid crystal, alignment of the "director" (long axis) of the liquid crystal may be achieved. Different orientations of the liquid crystals have different optical properties due to their geometry. When arranged so that the director of the molecules twists slowly (compared to the wavelength of incident radiation) with distance perpendicularly away from the surface, very strong polarisation rotation occurs over distances of tens of micrometers. This phenomenon is used extensively in flat screen liquid crystal displays (LCDs) [175].

## 8.3 Electromagnetic Chirality

There is a long history in the study of chiral media in the EM regime, beginning in the optical where the rotation of the plane of a linearly polarised light source in quartz crystal, liquids and gases was studied in the early 19th century by Arargo, Biot and others [173, 176, 177]. It was suggested that the cause of the rotation was the geometry of the molecules making up the media, although the concept of molecule handedness was not confirmed until the 1840s by Pasteur. In the 1910s Lindeman introduced the concept of optical activity to radio waves, using helical coils as pseudo-molecules. Since then chiral media have served in many applications in the microwave regime such as antennas, polarisers and waveguides [176, 177].

Any material that rotates the plane of polarisation is said to be optically active [178], and recently, the concept of chirality in subwavelength-structured metamaterials has created much interest in the metamaterials research community after the possibility of using chiral media to produce negative refractive index materials was suggested by Pendry [179] and Tretyakov *et al.* [180, 181] independently, with potential applications as superlenses for circularly polarised waves. It was proposed that in order to provide a negative refractive index for one circularly polarised state the chirality parameter, a normalised measure of the difference between the left and right handed eigenvectors, needs to be larger than $\sqrt{\varepsilon\mu}$. Where the chirality parameter is formally defined as:

$$\kappa = \left(\frac{k_+ - k_-}{2 \times k_0}\right) \tag{8.1}$$

When $\kappa \neq 0$, the material is chiral. Here $k_-$ and $k_+$ are the eigenvectors for right and left handed circularly polarised radiation respectively (as seen from the source, in the direction of propagation), and $k_0 = \omega/c$ is the free-space wavevector. Further details for the process of obtaining the chirality parameter from experimental parameters can be found in [182].

In naturally occurring materials the chirality parameter is smaller than 1, while the $\sqrt{\varepsilon\mu}$ is greater than one. By artificially structuring a chiral metamaterial, the permittivity and permeability may be designed to be close to zero and the chirality designed to ensure the refractive index for one circular polarisation state is negative. This has led to an explosion in the work searching for a structure that may possess these characteristics. The study of these chiral metamaterials can be split into two broad categories: 2D and 3D structures, each exhibiting its own brand of optical activity.

### 8.3.1 3D Chirality

As previously mentioned 3D chirality in nature has been studied since optical activity was first observed by Arago in 1811 [173]. For more information, a thorough historical overview is given by Plum [183]. It is now widely accepted that materials with a 3D electromagnetically chiral nature exhibit circular birefringence and circular dichroism, together these are termed optical activity.

**Circular birefringence** the ability to rotate the plane of polarisation of EM waves regardless of the plane of polarisation.

**Circular dichroism** the difference in transmission for right and left handed circularly polarised waves.

In a bulk medium such as quartz this corresponds to different refractive indices for left and right hand circularly polarised waves. The real part (responsible for circular birefringence) results in different phase delays for each circular polarisation state, while the imaginary part (responsible for circular dichroism) determines the absorption losses. 3D chiral metamaterials are independent of the direction of propagation. Recently researchers have also considered structures with relatively complex chiral elements including helices [184], multiple layers of rosettes [185] and gammadions [186, 187] (for

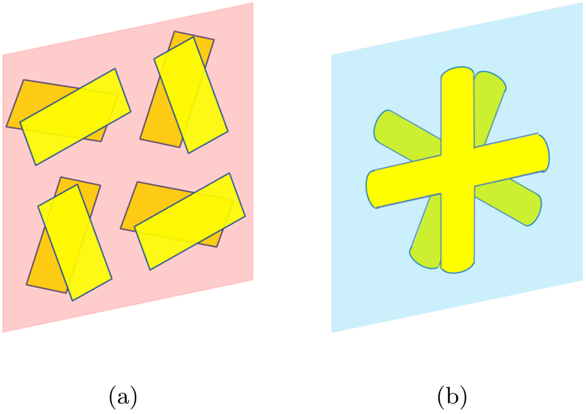

Figure 8.1: The unit cell of two 3D chiral materials arranged in two arrays separated by dielectric in the propagation direction. The unit cell for (a) an array of cut wire pairs and (b) an array of rotated crosses .

the geometry of a gammadion see the array in Figure 8.2), as well as much simpler geometries such as wire pairs [175, 188] (see Figure 8.1(a)), and layers of rotated crosses [189, 190] (see Figure 8.1(b)) in which individual elements are not chiral however the azimuth rotation of each inside the unit cell (not the array itself), combined with a second layer of a different rotation angle, render multilayer structures chiral.

Considering the work on rotated wire pairs in more detail [175, 188, 191], each unit cell contains four pairs of planar strips of metal. Each pair is separated in the propagation direction by 2 mm of FR4 dielectric, with a fixed azimuth angle between them. The four pairs within the unit cell all have a different starting angle (see Figure 8.1). Each strip of metal is described as a fully metallic "molecule with inductive coupling between the two parts". Svirko *et al.* [191] consider a normally incident EM wave, creating electric currents in the strips, driving the positive and negative charges to opposite ends of the strips, that act as dipoles. In turn, inductive coupling excites charges in the lower strip, (that again acts as a dipole) re-emitting the incident radiation at a different azimuth angle. This is observed as the rotation of the plane of polarisation in the scattered fields.

### 8.3.2 2D Chiral Structures

By considering the geometry of a 2D (planar) chiral structure such as that in Figure 8.2, the structure possesses opposite handedness when viewed from opposite sides. Therefore the crucial difference between 2D and 3D chirality is that planar chiral materials induce opposite polarisation changes for radiation transmitted through the structure

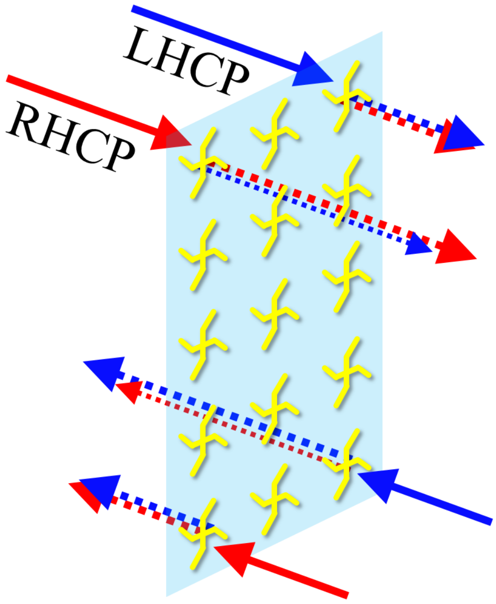

Figure 8.2: An array of gammadions illuminated with right hand circularly polarised light (RHCP - red arrow) and left hand circularly polarised light (LHCP - blue arrow) from both sides of a single array.

in opposite directions. Planar chiral metamaterials are optically active due to circular conversion dichroism (see below).

**Circular conversion dichroism** Left to right and right to left hand circular polarisation conversion efficiencies are not equal and crucially are reversed for opposite propagation directions (referred to as directional asymmetry). [183]

The majority of such structures comprise of a single plane of rotated elements in a regular unrotated array, such as split rings, rosettes, and gammadions [192–194]. A gammadion consists of a 4 arm cross, where each arm is formed of a straight section followed by a second section that is bent towards the normal by an acute angle. Consider a linearly polarised wave propagating normally to the planar array of metallic gammadions. When the gammadions are arranged in a square array, and spaced such that they do not interact with one another, an azimuthal rotation of the polarisation is observed. This structure is not only polarisation sensitive but also polarisation converting. This can be understood by considering how the electric and magnetic fields interact with the metallic gammadion. When the electric field is directed along one of the gammadion legs, the positive and negative charges within the metal flow to opposite ends of the legs around the bend to the second section, thereby inducing a small amount of polarisation perpendicular to the driving field. The re-emitted fields produced by this chiral structure are elliptically polarised and show rotation of the plane of polarisation [192, 195]. This description was first reported for anisotropic lossy planar chiral metamaterials at microwave frequencies [196, 197] noted as excitation of currents sensitive to the geometry of the structure that are responsible for this polarisation converting behaviour.

Investigations cited above, that utilise arrays of symmetric elements, break the intrinsic symmetry by rotating individual elements so that the mirror planes of the elements do not coincide with a mirror plane of the array. A new way of inducing chirality has recently been presented by Plum et al. [198], showing that asymmetric transmission of circularly polarised waves can in fact be achieved through any lossy periodically structured system radiated at oblique incidence.

In this present experimental study a 3D chiral structure is proposed and investigated. Unlike the structures discussed above, the individual elements are not chiral in geometry, nor are they rotated in azimuth within the unit cell. The arrays of elements are not chiral and are not orientated at an oblique angle of incidence with respect to the direction of the incident radiation. Instead, one square array is rotated relative to another and separated by less than the decay length of the EM fields in the propagation direction. In what follows two structures will be considered both experimentally and by using numerical modelling to gain insight into the EM mechanism responsible for the observed phenomena.

## 8.4 Commensurate Rotation

A commensurate rotation is formed when two or more lattices are rotated such that coincident points can be found from both set of lattices. This forms the commensurate unit cell that can be replicated in the chosen direction, in this case the $x$ and $y$ directions (orthogonal to the propagation direction, $z$). While the experimental sample does not require a commensurate unit cell to be formed, it is for ease of numerical modelling (in particular Finite Element Method (FEM) modelling) that a small and therefore commensurate unit cell is used. A small unit cell is of particular importance when investigating closely spaced multilayer subwavelength structures. The commensurate unit cell investigated here (Figure 8.3) uses a $(2, 1)$ rotation that corresponds to an angle of $\theta = 26.56^\circ$ about the $z$ axis, that equates to $\psi = \frac{\pi}{2} - (2\theta) = 53.12^\circ$ between two rotated arrays.

In order to find a commensurate rotation the lattice points of the first array must be rotated about the $z$ axis (orthogonal to both arrays) such that a sub–set of lattice points coincide to lie directly above a sub–set of lattice points on the second array. This

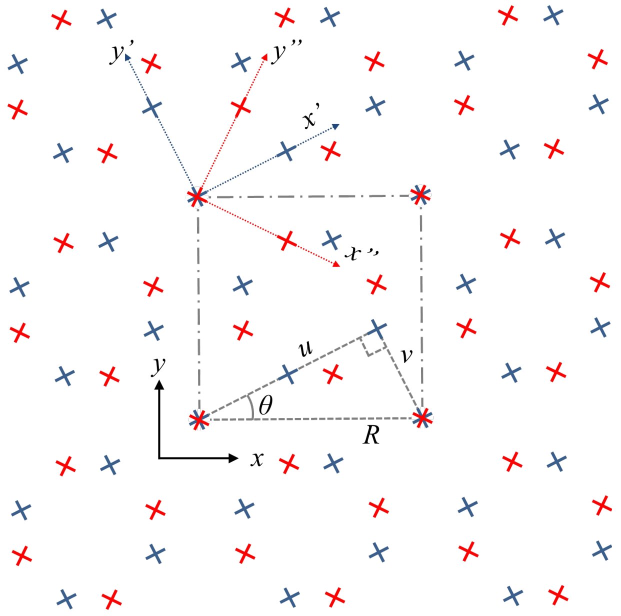

Figure 8.3: Diagram showing the coordinate systems of two arrays rotated by $\pm\theta = 26.56°$ (blue, and red respectively) to form a $(2, 1)$ rotation.

can be easily seen by rotating any two identical lattices with respect to one another in the azimuth $(xy)$ plane.

In this experimental study square lattices are used, however hexagonal lattices too could support this evanescent handedness phenomena, as discussed in section 9.3.3. By rotating two square lattices about a single lattice point and specifying that at some angle $\psi$ a sub–set of lattice points must coincide, a triangle $(uvR)$ is formed (shown in Figure 8.3) where $u$ and $v$ are the integer number of lattice points in the $x'$ and $y'$ directions respectively and $R$ is the pitch of the commensurate unit cell.

Using simple Pythagoras $(a^2 + b^2 = c^2)$ table 8.2 is constructed to find the smallest value of $R$.

In table 8.2 it is clear that the smallest commensurate unit cell is the $(u, v) = (1, 2)$ or $(2, 1)$, however it is constructive to consider larger combinations of $u, v$. Interestingly while the value of $R$ given for the $1, 3$ or $3, 1$ rotation is $\sqrt{10}$, this does not give the smallest commensurate unit cell that may be formed by this structure. The unit cell is shown in Figure 8.4, it is the diagonal of the unit cell that lies along the line at an angle $\frac{\pi}{4} - \theta$ to the array. The pitch of this smaller unit cell can be obtained by dividing $R$ by $\sqrt{2}$ to give $\sqrt{5}$; giving the same pitch as the $(1, 2)$ or $(2, 1)$ rotation.

By considering table 8.2, some general rules can be obtained for finding the unit cell pitch for commensurate rotations:

| | | | | | u | | | |
|---|---|---|---|---|---|---|---|---|
| | $R$ | 1 | 2 | 3 | 4 | 5 | 6 | 7 |
| | 1 | × | $\sqrt{5}$ | $\sqrt{10}$ | $\sqrt{17}$ | $\sqrt{26}$ | $\sqrt{37}$ | $\sqrt{50}$ |
| | 2 | $\sqrt{5}$ | × | $\sqrt{13}$ | $\sqrt{20}$ | $\sqrt{29}$ | $\sqrt{40}$ | $\sqrt{53}$ |
| | 3 | $\sqrt{10}$ | $\sqrt{13}$ | × | $\sqrt{25}$ | $\sqrt{34}$ | $\sqrt{45}$ | $\sqrt{58}$ |
| $v$ | 4 | $\sqrt{17}$ | $\sqrt{20}$ | $\sqrt{25}$ | × | $\sqrt{41}$ | $\sqrt{52}$ | $\sqrt{65}$ |
| | 5 | $\sqrt{26}$ | $\sqrt{29}$ | $\sqrt{34}$ | $\sqrt{41}$ | × | $\sqrt{61}$ | $\sqrt{74}$ |
| | 6 | $\sqrt{37}$ | $\sqrt{40}$ | $\sqrt{45}$ | $\sqrt{52}$ | $\sqrt{61}$ | × | $\sqrt{85}$ |
| | 7 | $\sqrt{50}$ | $\sqrt{53}$ | $\sqrt{58}$ | $\sqrt{65}$ | $\sqrt{74}$ | $\sqrt{85}$ | × |

Table 8.2: Integer values of $u$ and $v$ to form the rotation of two square arrays to find a commensurate unit cell side length $R$.

- If $u =$ odd and $v =$ odd, the diagonal of the smallest unit cell lies along the line at angle $\frac{\pi}{4} - \theta$ to one array, as shown for the $1, 3$ or $3, 1$ rotation in Figure 8.4.
- If $u =$ odd, and $v =$ even or $v =$ odd, and $u =$ even, the side of the smallest unit cell lines along the line at angle $\theta$ to one array, as shown for the $1, 2$ or $2, 1$ rotation shown in Figure 8.3.
- If $u =$ even and $v =$ even, simplify to find the smaller commensurate rotation.

The smallest unit cells are the following $\sqrt{5}$ formed by rotations $(1, 2)$ $(1, 3)$ $(2, 4)$ $(2, 6)$..., $\sqrt{13}$ formed by rotations $(2, 3)$ $(3, 5)$ $(4, 6)$..., $\sqrt{17}$ formed by rotations $(1, 4)$ $(3, 5)$..., and so on.

### 8.4.1 Creating the Commensurate Unit Cell in the FEM Model

As the unit cell for the $(2, 1)$ rotated structure has a unit cell side length $\sqrt{5}$ larger than the pitch of the individual array, more than one unit cell of the individual arrays must be modelled. The metallic meshes are initially considered followed by the complimentary patch structure. Everything discussed here for the metallic meshes can be applied to the complementary patch system.

In order to model this structure using the finite element method [83] a CAD front end is used to draw the physical unit cell, as explained in section 3.3.1. The unit cell of the square metallic mesh is created by subtracting a vacuum box of width $a$ from a thin metal sheet of width $d$ and thickness $t_m$. This is then duplicated in the $x$ and $y$ directions. This array represents the top or bottom metallic mesh of the sample. A similar array is created and separated from the first by the variable $t_d$ in the $z$ direction. The first array is rotated by $+26.56°$, while the second is rotated by $-26.56°$ about the $z$ axis. Both arrays are then cropped at $\sqrt{5} \times d$, creating the $(2, 1)$ rotated arrays as

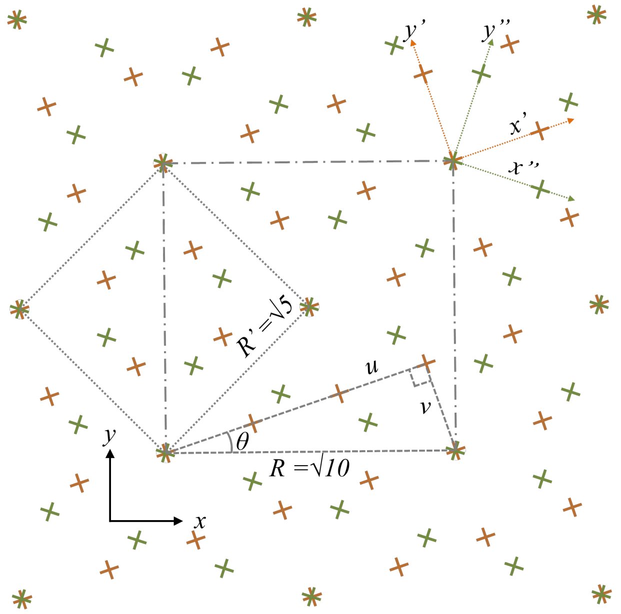

Figure 8.4: Diagram showing the coordinate systems of two arrays rotated by $\pm\theta = 18.43°$ (orange and green respectively) to form a $(3, 1)$ rotation, which is equivalent to a $(2, 1)$ rotation (Figure 8.3).

shown in Figure 8.5. In order for the model to be "repeated" to infinity in the $x$ and $y$ directions a master-slave boundary condition is used. First a vacuum box is created that covers the whole structure, then pairs of faces of this box in the $xz$ and $yz$ planes are selected where one becomes the master and the second the slave. As previously detailed Floquet ports are added to the top and bottom $xy$ faces of the vacuum box provide the incident radiation. See section 3.3.4 for further explanation.

## 8.5 The Chiral Geometry of the Experimental Sample

To be electromagnetically chiral there must be interaction between the two layers. To illustrate this two systems are considered: the first where the distance between the arrays, $t_d$, is large, the second where $t_d$ is small. However first it is instructive to consider the response of a single metallic mesh layer when rotated in the azimuth plane at normal incidence. To recap briefly the proportion of transmitted and reflected radiation is dependent on the pitch and hole size [29]. When this structure is rotated azimuthally the response of the system is unchanged due to the symmetry of the metallic mesh (equally true when the linear polarisation is rotated).

Now consider two hole arrays rotated by ±26.56° from the $x$ (or $y$) axis (as in the experimental sample) separated by a large distance (many wavelengths), illuminated with linearly polarised EM radiation. Here, although the structure is chiral according to the geometry, the arrays do not interact. The EM wave propagates to each metallic mesh where it is decomposed, evanescently transmitted and recomposed, transmitted unrotated through each array.

Consider the second case where the arrays are separated by a smaller gap, less than twice the evanescent decay length of the EM field, as defined in section 2.4.1.1 as ($\delta_m = \frac{1}{k_z} = (\varepsilon_m k_0^2 - k_x^2)^{-\frac{1}{2}}$. The evanescent decay of the EM fields from the two arrays interferes to form a resonant mode. Evanescent fields contain near field information regarding the geometry of the structure. Transmission of the near field information has been exploited in many investigations of near field imaging and super lensing where the evanescent fields associated with a subwavelength structure are transmitted over many wavelengths where they are interpreted as in [199]. This occurs when the subwavelength geometry is illuminated with a wavelength of radiation larger than the feature, evanescent diffraction occurs, the evanescent fields excite surface waves (surface plasmons) at the dielectric–silver interface, are coupled through the block of silver to a second surface plasmon on the silver–dielectric interface. Here the subwavelength structure allows the evanescent diffraction and the coupling to occur between the two layers, however evanescent fields still transmit EM subwavelength properties. Here the geometry of the structure includes the rotation, therefore when the near fields couple and chiral modes are formed, rotating the plane of polarisation through the structure. This unexplored area has been coined: evanescent handedness.

## 8.6 Rotating Metallic Meshes

### 8.6.1 Experimental Sample

In this study the experimental sample comprised of two $t_m = 100$ µm thick stainless steel free-standing meshes of pitch, $d = 4$ mm and hole size $a = 3.7$ mm were rotated by $\pm 26.56°$ from the $x$ axis about the $z$ axis, forming the $(2, 1)$ unit cell described previously. The metallic meshes were held in a circular sample holder as shown in Figure 8.6, suspended from thick metallic frames (metallic meshes on the inner faces). The metallic meshes were fixed to the frames in a variety of ways (a range of adhesive tapes, two part epoxy resin, nylon thread) however the final iteration of the design of the sample holder used nylon thread woven through alternate holes of the metallic mesh and through holes drilled into the 'L' shaped support frame on all four sides. These were tensioned, then two metallic meshes were then spaced by 0.5 mm by arranging Mylar strips around the edges of the frame (not in the experimental beam spot area). Free-standing metallic meshes with no dielectric super/substrate were used to ensure

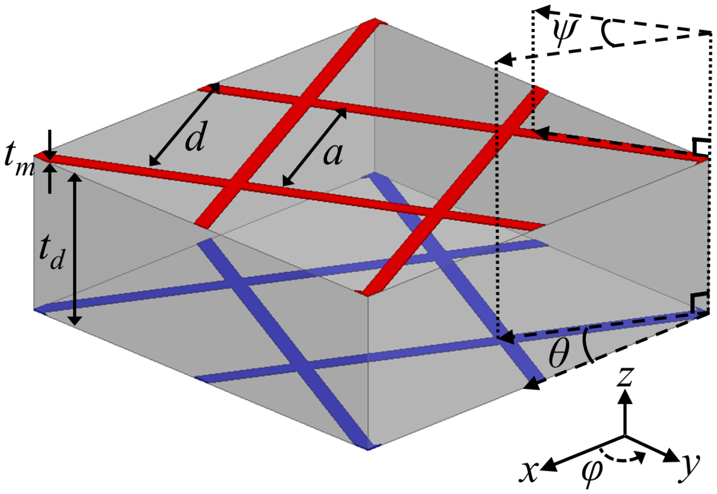

Figure 8.5: Exploded view of the modelled commensurate unit cell for the rotated metallic mesh structure, where $a = 3.7$ mm, and $d = 4$ mm, $t_m = 100$ µm, $t_d = 0.5$ mm $\psi = 36.88°$ and $\theta = \pm 26.56°$. Azimuthal angle $\phi$ for the detected polarisation (parallel to the $+x$ axis $\phi = 0°$).

minimum absorption by the structure. The metallic meshes were rotated by hand, and small locator pins used in the metallic meshes to hold the sample in the correct orientation while the sample holder was clamped together. The locator pins were then removed for the experimental measurements to be undertaken.

### 8.6.2 Experimental Setup

To be chiral the system must rotate the plane of polarisation, and have different responses for right and left right handed circularly polarised transmission. In this investigation linearly polarised radiation is used to probe the sample to prove it is chiral.

Linear polarised radiation can be considered as being composed of two circularly polarised components, if these components are rotating in opposite directions (right and left handed), have the same amplitude, and are coherent. The orientation of the plane of linear polarisation will be a function of the relative phase between the right and left hand circularly polarised components (RHCP and LHCP respectively) [174, 178].

If the transmission of the RHCP and LHCP components are unequal, then the result will be an elliptical polarisation state. This can be quantified by measuring the polarisation conserving and polarisation converting transmission, and also by rotating a linearly polarised detector (using a linearly polarised input) to sample the amount of transmission in the azimuth plane. See section 8.10 for more detail. The ellipticity of

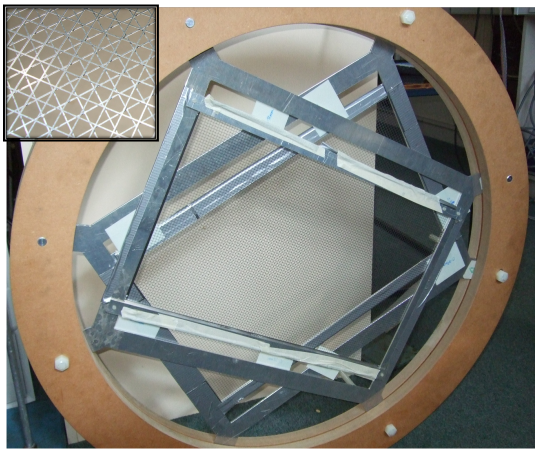

Figure 8.6: Photograph showing the sample and holder for the two rotated metallic meshes held at $\theta = 26.56°$. Inset shows a close up of the two layers of rotated metallic meshes.

the structure is a measure of the circular birefringence.

Finally by considering the complex transmission of both the orthogonal linearly polarised states, the transmission for right and left circularly polarised radiation can be calculated, see section 8.11.

The experimental technique used for measuring the polarisation conserving response of a system is described in section 4.3. The technique for measuring the polarisation converted response is similar. The apparatus must be accurately aligned as described in section 4.3 using both the linearly polarised emitting and detecting waveguide horns orientated such that the associated electric field vector is in the same direction. Care must be taken (and regular checks made) to ensure no polarisation converting signal occurs when a reference sample is used. To measured the polarisation response the detector is rotated by 90°.

It is misleading to talk about transverse electric and transverse magnetic or s- and p- polarised radiation at normal incidence. So here the electric field vector is defined as being parallel to the $x$ axis ($\phi = 0°$ in Figure 8.5) or the $y$ axis ($\phi = 90°$ in Figure 8.5). Therefore when considering a polarisation conserving response subscripts will read $xx$ or $yy$ to define the orientation of the emitter and detector respectively. Following this, a polarisation converting response will have subscripts $xy$ or $yx$.

### 8.6.3 Experimental Results

In Figure 8.7 and 8.8 the experimentally recorded results (black circles) and numerically modelled predictions (red line) show the polarisation conserving and converting transmitted response for $20 - 35$ GHz. The experimental signal does not show the resonant feature so prominent in the modelled predictions.

The Fano-shaped [200] features in the modelled polarisation conserving response occurring at 23.9 GHz and 29.6 GHz coincide with resonant peaks occurring in the modelled polarisation converting response. These modelled results reveal that at these frequencies small amounts of $x$-polarised radiation are expected to rotate to $y$-polarised radiation. This could indicate a chiral response. The lack of experimental evidence of these modes is attributed to two factors: beam spread, and the flatness of the metallic mesh. Beam spread in the experimental system arises because the wave impinging on the sample does not possess planar wave fronts. As previously discussed in section 4.2.2 the collimating mirrors are designed to work with a point source placed at the focal point. Here, the standard gain horns are assumed as the point source, however the beam is actually more Gaussian leading to a slight curvature of the wave fronts, leading to a reduction in the amplitude and an increase in the full width half maximum of the transmission peaks.

The second problem is the flatness of the metallic mesh when mounted to the frame, that causes the spacing between the metallic meshes, this needs to be constant across the beam spot area. First the metallic mesh was stretched and held over the metal frame using a series of adhesives tapes and then increasing strength adhesive glue including 2 part epoxy resin. Then thick nylon thread (fishing line) was woven through every second hole and wrapped around the frame. All of these increasingly improved the tension across the surface of the metallic mesh. However, the nylon thread prevented the metallic meshes from being placed close enough to excite strong resonant modes that could be experimentally observed. This was overcome using frames made out of bars with a ‘L’ shaped cross section. The metallic mesh was placed above the vertical section of the ‘L’, and again nylon thread was woven through every second hole and secured to holes drilled in the horizontal section of the frame. This provided a flatter, and very taught metallic mesh when all four sides were tightened in turn. The corners of the metallic meshes were cut to avoid bowing. Strips of 0.5mm thick Mylar were placed around the edge of the sample, however the sharp resonant modes were not observed in polarisation conservation or polarisation converted transmission responses even with all this care in sample mounting.

## 8.7 An Array of Holes Compared to an Array of Patches

The complementary structure was also investigated - two layers of rotated patch arrays. This could also be viewed as an air mesh in a metallic sheet and is also known as a capacitive mesh. Modelling shown in Figure 8.9(a) and 8.9(b) reveals resonant modes that have a stronger and broader polarisation converting response compared to the

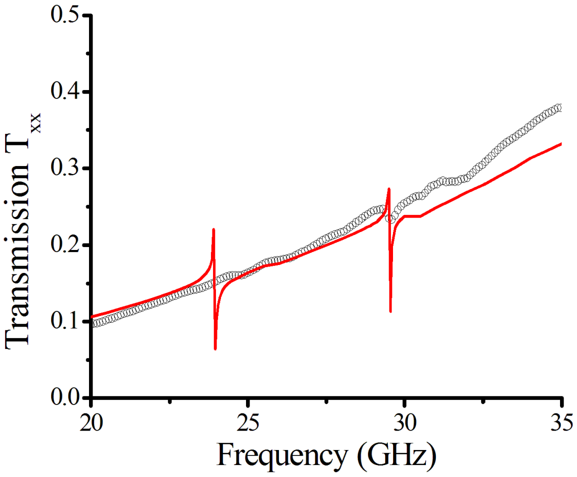

Figure 8.7: Experimentally observed (black circles) and numerically modelled (FEM - red line) polarisation conserved transmission for the rotated metallic meshes with a metallic mesh separation of $t_d = 0.5$ mm.

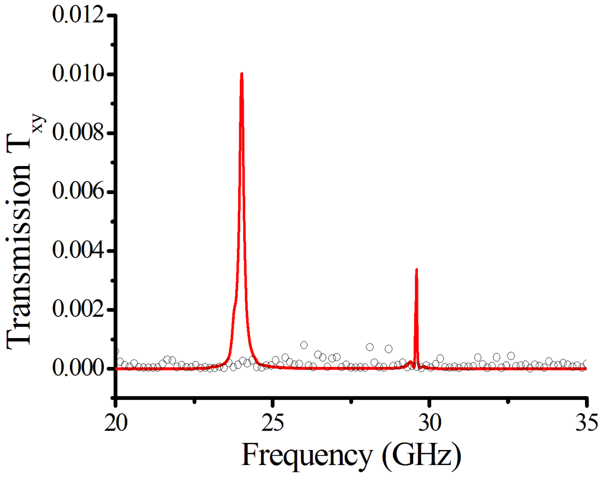

Figure 8.8: Experimentally observed (black circles) and numerically modelled (FEM - red line) polarisation converted transmission for the rotated metallic meshes with a metallic mesh separation of $t_d = 0.5$ mm.

response when using metallic meshes (note the extended frequency range). Here the resonant peaks associated with the polarisation converting modes lie in the wings of the resonant peaks which corresponds to a mode that is quantised between the two patch arrays. When the arrays are unrotated this resonance occurs at 28.8 GHz, (black line in Figure 8.9(a)) however when the patch arrays are rotated the patch area overlap decreases and this resonance increases in frequency to 32.0 GHz, the rotation also allows other combination patch resonances to occur.

The rotated patch array structure was optimised with an aim to broaden and intensify the polarisation converting modes. Resonant features $> 50\%$ transmission in the polarisation converted response were predicted (compared to 1% in the predicted rotated metallic mesh response), so all efforts were refocussed to explore this structure experimentally.

## 8.8 Metallic Patch Arrays

Metallic patch arrays have been extensively studied since the 1960s. Books by Munk, and Wu [1, 2] give excellent reviews of the literature in their introductory chapters which will not be repeated here.

Subwavelength patch arrays are considered as an alternative to the metallic mesh. The response of a single metallic patch arrays can be easily predicted by employing Babinet's principle [16, 201] (section 2.3). It is assumed that the metal is perfectly electrically conducting (PEC) and infinitely thin (sample thickness $< \frac{\lambda}{100}$), then the response of the patch array is $1 - T_{mesh}$ where $T_{mesh}$ is the transmission through the metallic mesh of the complimentary geometry. Below the onset of diffraction the disconnected patch array considered here is highly transmitting. The transmission decreases to a minimum close to the onset of diffraction. However, in this subwavelength regime the array can be considered as an isotropic effective medium. This is evidenced by the fact that the EM response of a single array is not dependent on the azimuthal angle between the plane of incidence and the axes of the lattice. Due to these low frequency characteristics, metallic patch arrays are well documented as finding applications as low pass filters, frequency selective surfaces and antenna arrays [1].

There also exists an extensive body of work exploring double–layer patch arrays [1, 2]. For two aligned and unrotated patch arrays, waveguide-like resonant modes in the cavity formed between the patch layers are supported [202]. Here the boundary conditions of the volume in which the EM fields are contained are reversed. For a perfect waveguide the EM fields are confined in the $x$ and $y$ directions by PEC walls and the incident and exit faces (in the $xy$–plane) are bounded by perfect magnetically conducting (PMC) boundaries. In a dual layer patch array system, the incident and

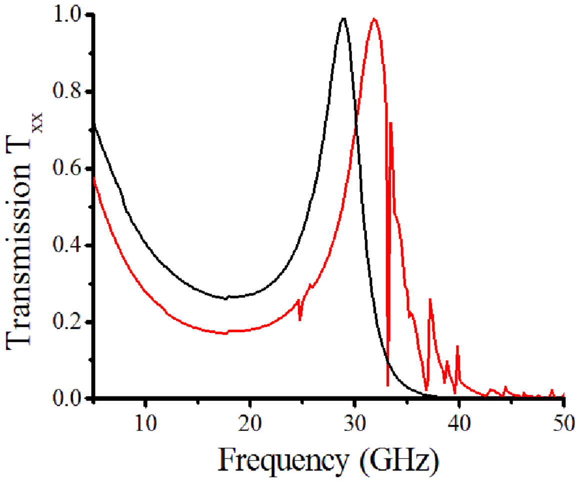

(a)

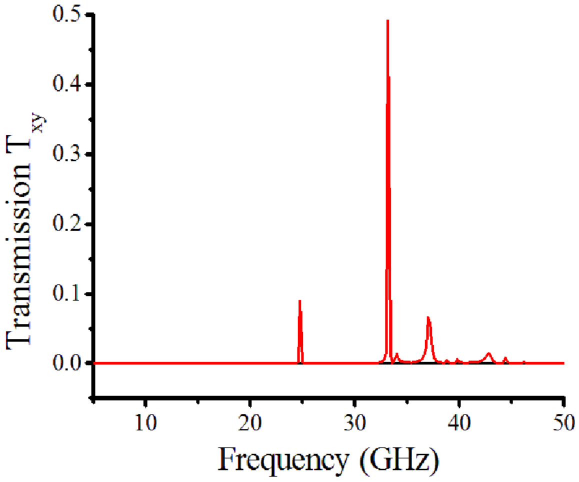

(b)

Figure 8.9: Preliminary FEM modelled polarisation conserved (a) and polarisation converted (b) transmission through two unrotated (black line) and rotated (red line) patch arrays, with a metallic patch array separation of $t_d = 0.5$ mm.

exit faces are the metallic patches (copper is near PEC in this regime), and the volume between the patches is assumed to be confined by PMC boundaries although in reality the EM fields extend between the patches, lowering the resonant frequency. In a dual layer system where the separation is large in the propagation direction, the EM response is independent of translational displacement in the plane of one array with respect to the other, as noted in Chapter 6. However when the layer spacing between the two patch arrays is small relative to the wavelength, the evanescent diffracted fields interfere and translational misalignment of the structure becomes important [88].

## 8.9 Rotating Patch Arrays

### 8.9.1 Experimental Sample and Setup

As discussed above it was found that patch arrays orientated using a $(2, 1)$ rotation are more likely to give observable polarisation rotating modes compared with the rotated metallic mesh structure. However, the original numerical model used perfectly electrically conducting patches suspended in vacuum. Obviously this could not be experimentally realised. Therefore a low loss dielectric described below was obtained. The substrate chosen was Rogers RO4003C, of permittivity $\varepsilon = 3.38 \pm 0.05$ and dielectric loss tangent $\tan\,\delta = 0.0027 \pm 0.0005$ specified at 10 GHz. This 0.508 mm thick dielectric ($t_d$) is supplied coated with a $17.5\ \mu\text{m} \pm 0.5\ \mu\text{m}$ layer of copper ($t_m$) on both sides. Using these parameters further numerical models optimized the remaining free parameters, patch pitch ($d$) and patch size ($a$). This design was chemically etched by Eurotech, a commercial Printed Circuit Board (PCB) manufacturer, with rotated arrays of pitch $d = 3.8$ mm, and square patch width $a = 3.5$ mm as shown in Figure 8.10.

By using a structure with a dielectric core formed of a dual sided PCB, earlier problems encountered with the two free-standing metallic meshes, mainly flatness and consistent spacing were overcome. The PCB thickness of 0.53 mm and associated error of ± 0.01 mm were measured after the chemical etching and include the copper coating. A simple two piece rectangular mount was used to clamp the sample holding it flat and orthogonal to the incident microwave radiation. An absorbing aperture was used to ensure a beam spot smaller than the sample area.

Linearly polarised microwave radiation is emitted from a waveguide horn with the electric vector parallel to the $x$-direction described in section 8.6.2. The detecting horn was mounted so it could be azimuthally rotated to allow quantification of any linear polarised output component. In what follows the polarisation state of each horn is defined by the angle $\phi$ the electric field makes with the $x$-axis (shown in Figure 8.10).

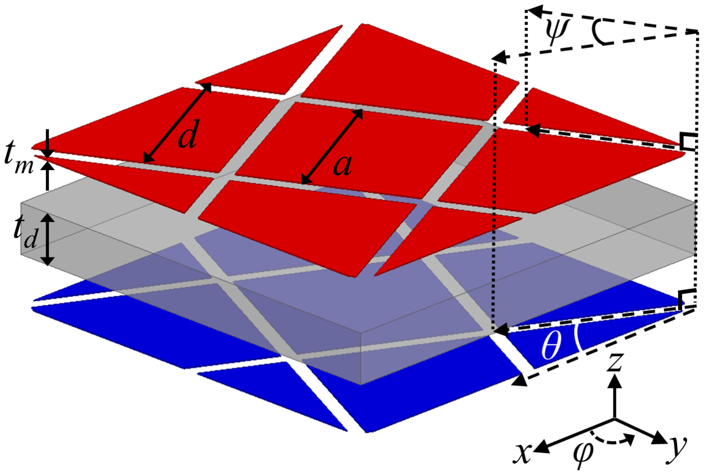

Figure 8.10: Exploded view of the modelled commensurate unit cell for the rotated patch array structure, where $a = 3.5$ mm, $d = 3.8$ mm, $t_m = 17.5$ µm, $t_d = 0.508$ mm, $\psi = 36.88°$ and $\theta = \pm 26.56°$. Azimuthal angle $\phi$ for the detected polarisation (parallel to the $+x$ axis $\phi = 0°$).

### 8.9.2 Experimental Results

The polarisation converted and polarisation conserved transmission results are shown in Figures 8.11 and 8.12 respectively. The black circles represents the experimentally recorded data and the red line represents the numerically modelled best fit line. Parameters fitted were the frequency dependent permittivity ($\varepsilon = 3.55 \pm 0.05$), dielectric loss tangent ($\tan\,\delta = 0.008$), and the $xy$ offset, ($x = 0.08$ mm$, y = 0.06$ mm). The $xy$ offset will be discussed further in section 8.9.2.3.

#### 8.9.2.1 Polarisation Converting Response

Two dominant peaks are observed in the polarisation converting transmission response (Figure 8.11) at 18.21 GHz and 25.08 GHz with a much weaker feature at 23.88 GHz. The latter peak arises when there is translational misalignment of the structure, see section 8.9.2.3. The two remaining transmission peaks are the polarisation converting modes. These modes arise from a series of modified patch resonances and do not occur when the two patch arrays are unrotated. The resonant modes form when the evanescent fields from each patch array interfere. These resonant modes have chiral EM field profiles in the dielectric region. Using the numerical model the vector electric field profiles have been plotted for a series of $xy$ planes in the propagation direction ($z$) in the dielectric region between the patch arrays, and are shown in Figure 8.13. These

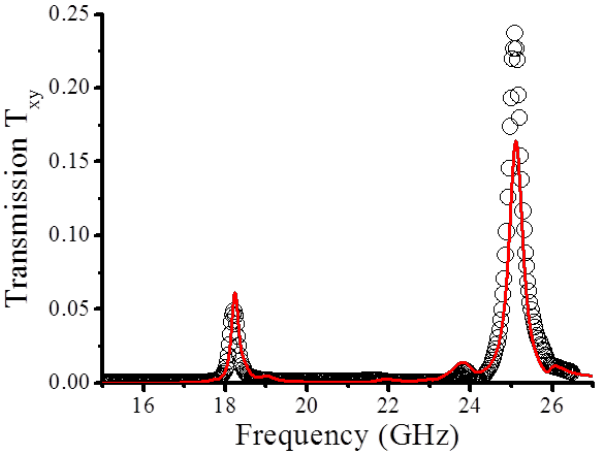

Figure 8.11: Experimentally observed (circles) and numerically modelled (line) response for polarisation conversion ($T_{xy}$). Subscripts refer to the orientation of the electric field vector in the incident and detected beams respectively.

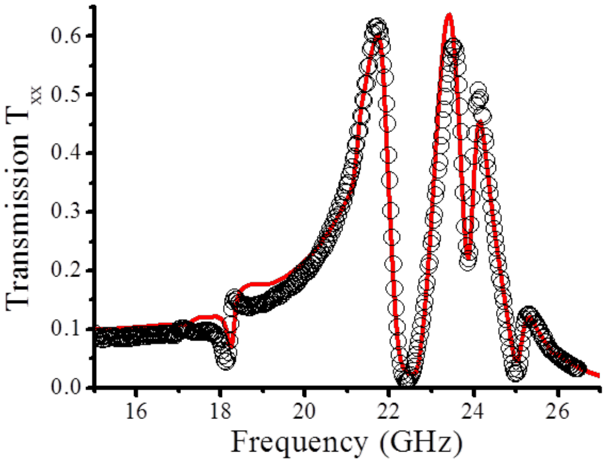

Figure 8.12: Experimentally observed (circles) and numerically modelled (line) response for polarisation conserving transmission ($T_{xx}$).

images shows the chiral nature of the resonant mode. At the upper patch–dielectric boundary the fields are concentrated normal to the slit regions of the first array, showing the decomposition of the incident field with respect to the unit vectors of the upper patch array. At the lower dielectric–patch boundary the fields are concentrated normal to the slit regions of the second array, showing the decomposition of the incident field with respect to the unit vectors of the upper patch array. In between the two, the electric field vectors interferes to form a resonant mode between the central patches that resembles an annular waveguide mode with a full resonant wavelength around the circumference. However the nodes of this wavelength occur along the diagonal of the unit cell, and excite secondary resonant patterns in the kite shaped regions along the diagonal.

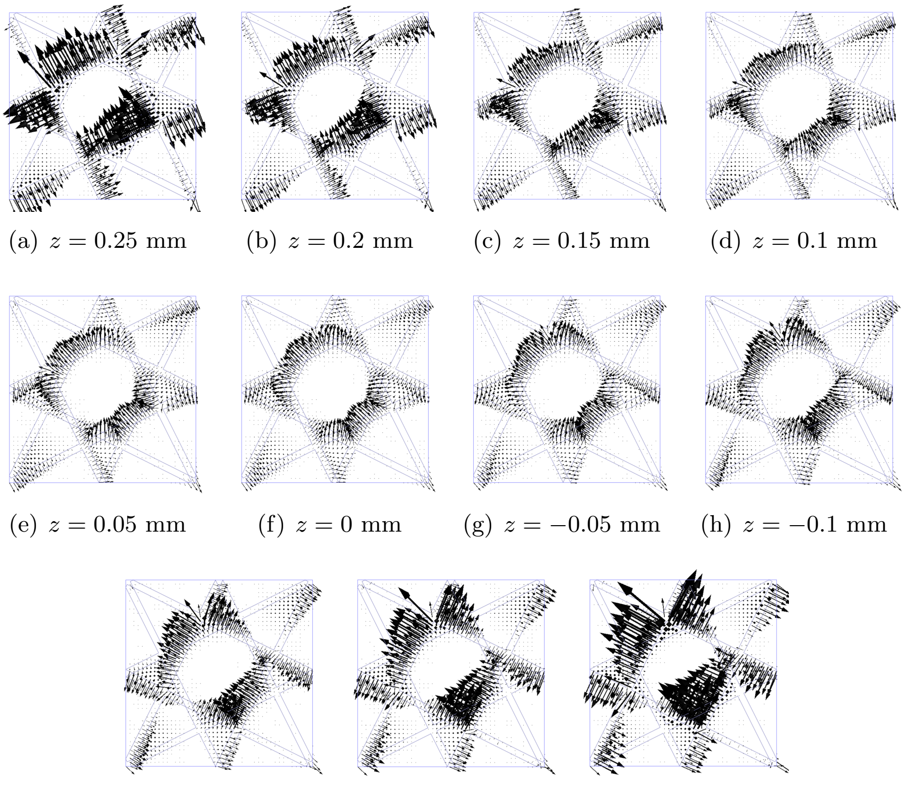

(a) $z = 0.25$ mm (b) $z = 0.2$ mm (c) $z = 0.15$ mm (d) $z = 0.1$ mm

(e) $z = 0.05$ mm (f) $z = 0$ mm (g) $z = -0.05$ mm (h) $z = -0.1$ mm

(i) $z = -0.15$ mm (j) $z = -0.2$ mm (k) $z = -0.25$ mm

Figure 8.13: Instantaneous vector electric field profiles for 18.21 GHz (taken at an arbitrary phase of 10°), shown in the $xy$–plane of the unit cell within the dielectric regions between the two patch arrays for a dielectric thickness of 0.508mm, where $z = 0$ is the centre of the dielectric region. All other parameters are as stated in section 8.9.2. The thickness and length of the arrows indicated the magnitude of the electric field enhancement that varies from 0 to 2000.

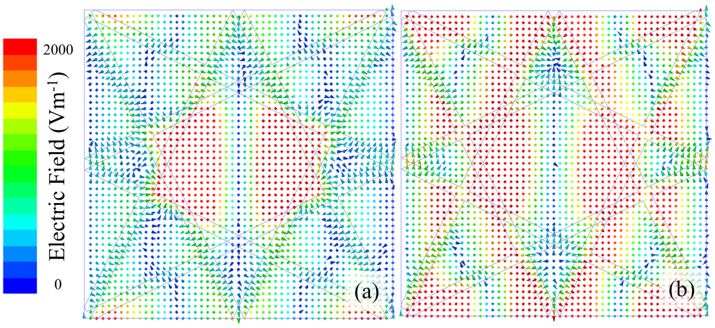

Figure 8.14: Instantaneous vector electric fields for polarisation conserving modes 20.81GHz and 22.46GHz (taken at a phase of 40° and 0° respectively, where the incident electric field is in the horizontal direction and the electric field varies from $0 - 2000$ $\mathrm{Vm}^{-1}$.

#### 8.9.2.2 Polarisation Conserving Response

Figure 8.12 shows the polarisation conserving transmission response. The three resonant modes associated with polarisation conversion, occur as three sharp troughs in the polarisation conserving response. These are superimposed onto a transmission response consisting of two large peaks separated by a minimum - that is not due to polarisation conversion (occurring at 22.3 GHz). The two peaks either side at 20.81 GHz and 22.46 GHz are patch resonances with electric field characters as shown in Figure 8.14.

The first mode occurring at 20.81 GHz is confined by the overlapping central patches of each patch array within the unit cell, supporting a waveguide–like mode in the dielectric region. Between the large fields to the left and right a null occurs, perpendicular to the incident radiation. This mode is reminiscent of the magnetic field for a $TE_{01}$ waveguide mode supported in an infinitely long cylindrical waveguide [6]. This mode is perturbed by a secondary resonance occurring in the largest kite shaped regions parallel to the incident electric field.

The second mode has a more curious electric field profile supporting many combination modes in the kite shaped regions. Here the mode occurring between the central patches is much stronger, forcing nodal regions at the top and bottom of the central diamond shape with further kite like resonances supported either side. In contrast to the polarisation converting resonant modes, here the modes are symmetrical along the central vertical axis, parallel to the plane of incidence, as opposed to the diagonal of the unit cell.

#### 8.9.2.3 The Affect of Translational Misalignment

The original FEM modelled polarisation conversion transmission results only revealed two resonant peaks. The transmission peak occurring at 23.88 GHz was absent. However, translational misalignment of the two square lattices in the $xy$–plane causes the weak feature experimentally observed to occur in the modelled transmission. The translation performed in the FEM modelling is shown in Figures 8.15 and 8.16 for translation in the $x$ and $y$ direction. By translating one array of patches in the $xy$–plane the centre of each array is offset. It is known that for closely spaced, evanescently coupled unrotated metallic meshes (and therefore through Babinet's principle for patch arrays) that the response of the structure will be perturbed with translation [88]. It is the evanescent fields that transmit the near field information about the structure that allow the polarisation conversion, observed here, to occur. Small translations change the area of overlapping metallic regions that excite other modified patch resonances that also allow a small amount of polarisation to occur. As the translation is increased the mode recorded in the polarisation converting response at 23.88 GHz strengthens accompanied by a sharp trough that deepens in the polarisation conserving response.

Numerical results do not provide a perfect fit to the experimental data. It is possible that a small error in the rotation of the two arrays could cause a similar change in the overlap patch area, however, the structure would no longer possess a unit cell. Therefore the structure would need to be modelled as a finite array, requiring more computational power than is available at this time.

## 8.10 Elliptically Polarised Waves

Linearly polarised radiation can be considered as being composed of two coherent, circularly polarised components, rotating in opposite directions with the same amplitude. The orientation of the plane of linear polarisation will be a function of the relative phase between the two circularly polarised states. If the transmission of the components is unequal, then the result will be an elliptical polarisation state [174, 178]. In order to show that this structure is chiral, circular birefringence, and circular dichroism must be demonstrated. The ellipticity of the resultant wave is a measure of the circular birefringence.

At the frequency at which the polarisation converting modes were recorded, a small proportion of unrotated transmission is simultaneously observed, evident as the nonzero polarisation conversion in Figure 8.12. Therefore, the resultant EM wave is elliptically polarised. This is experimentally measured and shown in Figure 8.17.

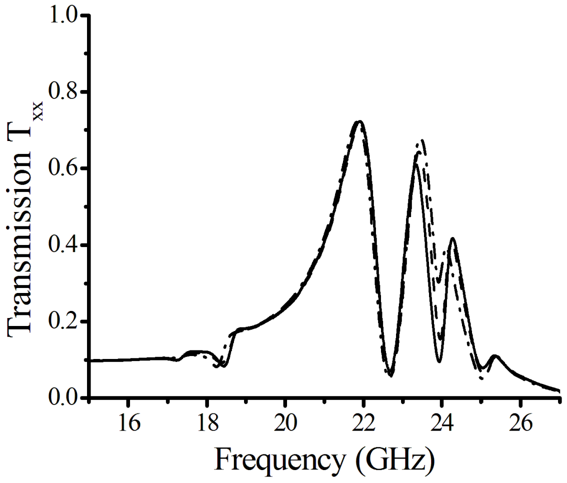

Figure 8.15: FEM modelled polarisation conserving transmission responses for translational offset of the top patch array with respect the the bottom patch array in the $xy$ plane by 0.05 mm, 0.08 mm, and 0.1 mm (solid line, dashed line, dot-dashed line respectively) in the $x$ and $y$ directions symmetrically.

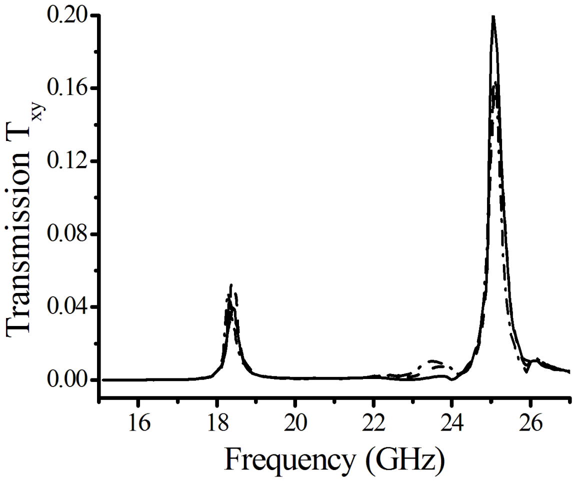

Figure 8.16: FEM modelled polarisation converted transmission responses for translational offset of the top patch array with respect the the bottom patch array in the $xy$ plane by 0.05 mm, 0.08 mm, and 0.1 mm (solid line, dashed line, dot-dashed line respectively) in the $x$ and $y$ directions symmetrically.

### 8.10.1 Experimental Setup

In order to quantify the rotation of the electric field evident in the FEM modelled response, the ellipticity of the transmitted wave is sampled by rotating a linearly polarised detector. The experimental technique closely follows that described in detail in section 8.6.2. Here the emitting horn is orientated such that the electric field is parallel to the direction of the $x$ axis (Figure 8.10). The detecting horn, is rotated by hand in 5° azimuth steps using a rotating mount. The azimuth rotation angle is defined as $\phi$ in Figure 8.10. Where the positive $x$ axis is orientated such that $\phi = 0$. The full $15 - 27$ GHz frequency spectrum is recorded. The response at the frequencies of interest were extracted to give the amount of transmission thorough the structure as a function of the azimuth angle of the detector.

### 8.10.2 Experimental Ellipticity Results

Experimentally recorded results shown in Figure 8.17 present the transmission as a function of the linearly polarised detector azimuth rotation angle ($\phi$). Two datasets are shown for frequencies of 18.21 GHz and 25.08 GHz (the frequencies at which the polarisation conversion occurs). The angle at which maximum transmission occurs for each mode determines the angle by which the plane of polarisation has been rotated; 65° and 40° ±5°, for the polarisation converting modes at 18.21 GHz and 25.08 GHz respectively. The radiation patterns do not close to a zero crossing to form a “figure of eight”. Instead, at $\phi = 0°$ and $\phi = 180°$, where the emitter and detector are co-polarised, a small amount of transmission occurs as seen in the polarisation conserving transmission in Figure 8.12. This transmission implies that the resultant wave is elliptically polarised. The degree of ellipticity can be calculated by measuring the maximum transmission, and the minimum transmission (at 90° to the maximum). These measurements form the major and minor axes of an ellipse where the ratio between these axes gives the degree of ellipticity.

$$\tan(\eta) = \frac{T_{major}}{T_{minor}}. \tag{8.2}$$

When $\eta = 0°$ the transmitted wave polarisation state is linear, and when $\eta = \pm 45°$ the transmitted wave state is right or left hand circularly polarised. Here $\eta = 4°$ and $\eta = 7°$ for the resonant modes at 18.21 GHz and 25.08 GHz respectively.

It is also interesting to note how the polarisation rotation occurs as a function of frequency. Figure 8.18 illustrates this for the lower frequency mode occurring at 18.21 GHz. Here the maximum and second maximum transmission values have been plotted as a function of frequency and azimuth rotation angle. The transition between

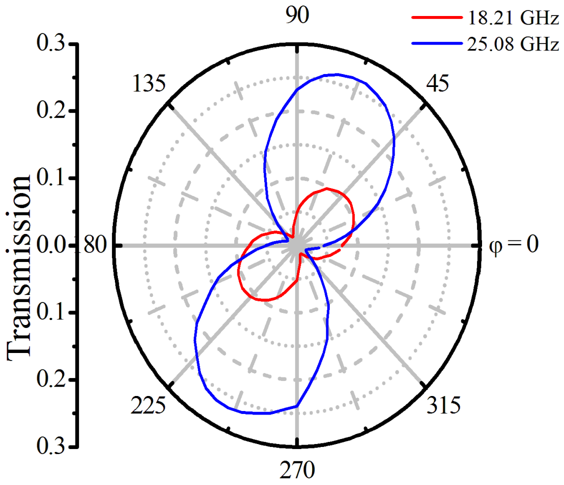

Figure 8.17: Polar plot presenting the experimental transmission as a function of detector azimuth angle $\phi$ for combination resonant modes at 18.21 GHz and 25.08 GHz. Data collected with the assistance of A.C. Oxlade.

$\phi = 180°$ and $\phi = 0°$ indicates the width of this mode. Note that points in the range $180° - 360°$ follow an identical pattern and have been included in this range for simplicity.

## 8.11 Circular Dichroism

By considering the complex transmission amplitude of the two orthogonal linearly polarised states from the experimentally recorded data, the transmission for right and left circularly polarised radiation can be calculated. The resultant ratio defines the circular dichroism.

In the following derivation the circular dichroism is defined in terms of the $x$ and $y$ transmission (the polarisation conserved and polarisation converted signals respectively). A linearly polarised beam of radiation can be represented by two circularly polarised components, right and left, with equal amplitude. Here we define the input polarisation as being solely in the $\hat{\mathbf{x}}$ direction.

$$\mathbf{E}_{inc} = \left(\frac{\hat{\mathbf{x}} + i\hat{\mathbf{y}}}{2}\right)_R + \left(\frac{\hat{\mathbf{x}} - i\hat{\mathbf{y}}}{2}\right)_L = 1\hat{\mathbf{x}}. \tag{8.3}$$

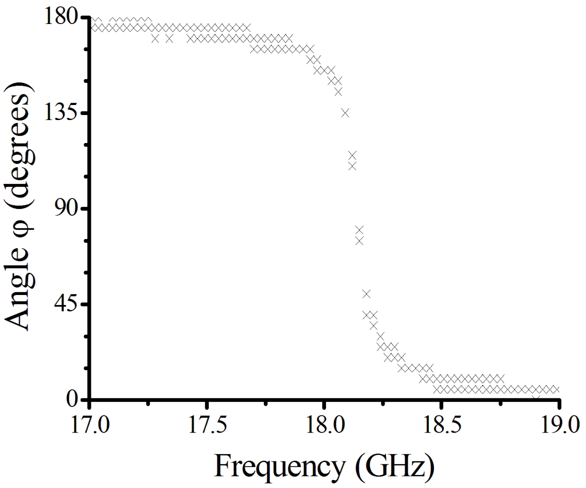

Figure 8.18: Experimental detector azimuth angle $\phi$ at which maximum transmission occurs as a function of frequency.

Therefore on transmission, the form of the electric field becomes:

$$\mathbf{E}_t = \left(\frac{\hat{\mathbf{x}} + i\hat{\mathbf{y}}}{2}\right)_R A_R e^{i\phi_R} + \left(\frac{\hat{\mathbf{x}} - i\hat{\mathbf{y}}}{2}\right)_L A_L e^{i\phi_L}. \tag{8.4}$$

So the $x$ and $y$ components are:

$$\mathbf{E}_{xt} = E_x e^{i\phi_x} = \frac{1}{2}(A_R e^{i\phi_R} + A_L e^{i\phi_L}), \tag{8.5}$$

$$\mathbf{E}_{yt} = E_y e^{i\phi_y} = \frac{1}{2}(A_R e^{i\phi_R} - A_L e^{i\phi_L}). \tag{8.6}$$

Equations 8.5 and 8.6, rearrange to give:

$$A_R = (E_x e^{i\phi_x} - iE_y e^{i\phi_y})e^{-i\phi_R}, \tag{8.7}$$

$$A_L = (E_x e^{i\phi_x} + iE_y e^{i\phi_y})e^{-i\phi_L}. \tag{8.8}$$

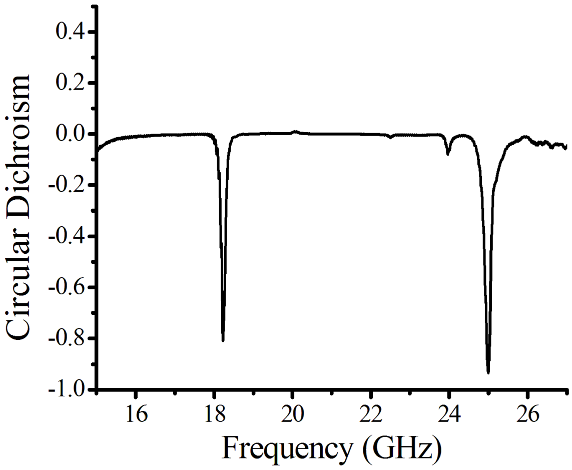

Figure 8.19: Normalised ratio of right hand circularly polarised to left hand circularly polarised transmission.

Using the complex conjugate of $A_R$ and $A_L$ and defining $\phi_{xy} = \phi_x - \phi_y$, $A_R^2$ and $A_L^2$ are found respectively.

$$A_R^2 = E_x^2 + E_y^2 - 2E_xE_y\sin(\phi_{xy}), \tag{8.9}$$

$$A_L^2 = E_x^2 + E_y^2 + 2E_xE_y\sin(\phi_{xy}). \tag{8.10}$$

As previously stated to find the circular dichroism we must compare the normalised difference in transmission between the right and left circularly polarised waves.

$$CD = \frac{A_R^2 - A_L^2}{A_R^2 + A_L^2}. \tag{8.11}$$

Thus:

$$CD = \frac{-2E_xE_y\sin\phi_{xy}}{E_x^2 + E_y^2}. \tag{8.12}$$

Figure 8.19 shows the circular dichroism over the frequency range measured where positive values indicate hand circularly polarised components of the transmitted EM field

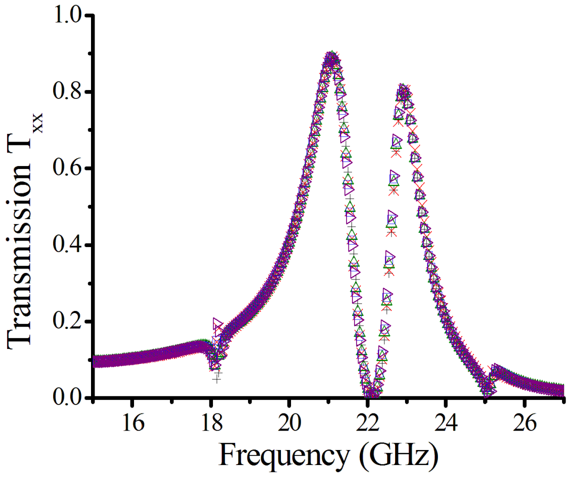

Figure 8.20: Modelled polarisation conserving transmission response for rotation of the azimuth angle of the plane of incident polarisation, showing almost invariant response at angles of $\phi = 0°, 10°, 20°, 30°$ and 45° (black cross, red cross, green triangle, blue square, purple triangle respectively).

dominate, and negative indicates left hand circularly polarised components dominate. At the frequencies at which the polarisation converting modes occur (18.21 GHz and 25.08 GHz) the circular dichroism shows the system is strongly chiral.

## 8.12 Azimuth Angle Independent Transmission

Experimentally measured and numerically modelled results indicate that the sample may be rotated by any azimuth angle, or equally illuminated by any azimuth angle of linear polarisation, yielding the same polarisation conserved and converted response. The polarisation conserving and polarisation converting response are shown of a structure with no misalignment in Figures 8.20 and 8.21. Changes in the experimentally recorded response (not shown) are due to the misalignment of the structure discussed in section 8.9.2.3, and are noted only to affect the feature at 23.88 GHz.

The two component subwavelength arrays have already been described as isotropic when considered in the frequency regime where the incident wavelength is much larger than the feature size. Therefore it is of little surprise that the structure is azimuth independent. It is the evanescent decomposition of the incident signal due to the unit vectors associated with the subwavelength geometry of the structure that allows any angle of linear polarisation to be rotated.

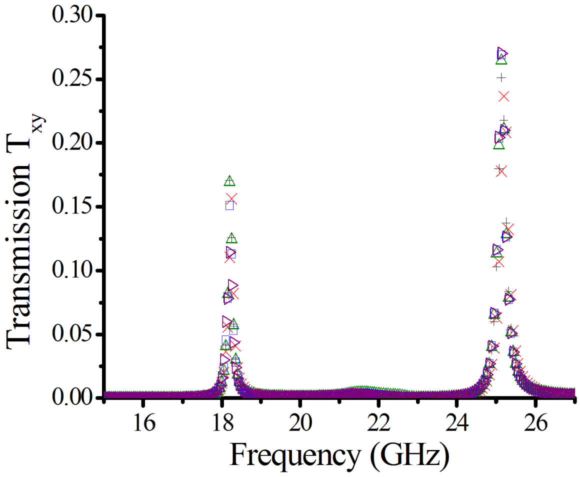

Figure 8.21: Modelled polarisation converting transmission response for rotation of the azimuth angle of the plane of incident polarisation, showing almost invariant response at angles of $\phi = 0°, 10°, 20°, 30°$ and 45° (black cross, red cross, green triangle, blue square, purple triangle respectively).

## 8.13 Concluding Remarks

This simple structure provides a potential new class for chiral EM metamaterials - "evanescent handedness". When two square-symmetric subwavelength patch arrays are several wavelengths apart there is no polarisation rotation as both arrays, for normal incidence radiation, have EM rotational invariance due to their square symmetry. However, as they are moved closer together, to within less than twice the evanescent decay length, significant polarisation rotation may occur. This ability to rotate the plane of polarisation is independent of azimuth angle but is frequency selective, depending on the size and shape of the patches chosen and the array symmetry.

# Chapter 9

# Conclusions and Further Work

## 9.1 Introduction

The work presented in this thesis details a series of original investigations into the microwave response of layered metamaterial structures incorporating a mesh structure. The mesh is either metallic, or a 2D array of slits in a metallic surface forming the complimentary structure - a patch array. Each chapter focuses on advancing the understanding of the resonant modes supported by a different structure when studied in the regime where the mesh is subwavelength, compared to the wavelength of the incident microwave radiation. Below the onset of diffraction and the cut off frequency (associated with the holes), the metallic mesh acts as an array of waveguides below their cut off frequencies, supporting no propagating fields in the holes, only evanescently decaying fields. Through a suitable choice of parameters and arrangement of the layers, the resonant modes can be tuned to form band pass or band stop regions extending to low frequency, with extended band widths and supporting unique modes with a chiral nature, allowing control through design.

## 9.2 Summary of Thesis

In the first section of this thesis, the microwave response of different stacks of metallic meshes were reported. Whilst enhanced transmission has been a well reported topic in recent years, these studies are conducted in the far subwavelength regime where surface waves are loosely bound to the metallic mesh interfaces and therefore do not produce an enhancement of the EM fields, instead the evanescently diffracted EM fields decay exponentially into the subwavelength holes. In Chapter 5, a single subwavelength metallic mesh is placed between two layers of dielectric, the EM experimental transmission response exhibits a remarkably wide highly transmitting band pass region.

By considering the metallic mesh as an effective medium, effective permittivity values where assigned and are shown to be analogous to a plasmonic metal in the visible regime. However, this structure exhibits no loss and therefore acts as an ideal tunnel barrier. The effect of the evolution of the thickness of the effective medium layer was analytically considered and revealed the merging of two resonant modes.

Numerical modelling of this structure has showed that the extended band pass region originates from the superposition of two non-interacting modes. The modelled fields revealed the *cosh* and *sinh*-like nature of the EM fields in the subwavelength hole of the metallic mesh coupling to the Fabry–Pérot-like modes in the dielectric cavity in and out of phase, for the lower and high frequency modes respectively. The low frequency mode was shown to be derived from the zeroth–order Fabry–Pérot mode, which occurs at low frequency ($\lambda \rightarrow \infty$). Here this mode is quantised by the *cosh*-like fields in the metallic mesh. The effective wavelength for this mode is much greater than twice the structure thickness (as expected for a dielectric–dielectric stack) and reducing the thickness or hole size of the metallic mesh, increases the effective wavelength, with the limiting case tending to infinity. The higher frequency mode is derived from the first–order Fabry–Pérot mode and can be tuned though a suitable choice of dielectric parameters allowing a pass band of almost complete transmission of frequency span greater than 20 GHz.

In Chapter 6 metallic meshes and thick dielectric spacers are arranged in a periodic stack. The experimentally recorded and numerically modelled microwave transmission response showed two pass band regions each containing multiple modes, the number of which corresponds to the number of bounded dielectric cavities in the stack. As in Chapter 5 the EM fields in neighbouring dielectric cavities oscillate in phase or out of phase depending on the form of the electric fields in the subwavelength holes of the metallic mesh being *cosh*-like or *sinh*-like respectively. The effective wavelength of each resonant mode is determined by the combination of the EM fields in the metallic mesh layers and may be tuned through appropriate choice of parameters. Here a numerical study shows the important result that increasing the number of unit cells does not increase the frequency band width by reducing the resonant frequency of the lowest frequency mode. It is found that the pass band width is almost independent of the number of layers, only depending on the properties of the unit cell. The number of unit cells only dictates the number of resonant peaks in the band pass of the transmission response.

In the third experimental Chapter 7, the EM response of a metallic mesh–dielectric stack was once again considered, however here two different metallic meshes were used in a single unit cell. The metallic meshes $A$ and $B$ where inter-spaced with thick dielectric layers (layer $C$) to give the unit cell $ACBC$. A stack containing 3.5 unit cells (four $A$

layers, three $B$ layers spaced by six $C$ layers) was experimentally considered. When investigating the properties of this structure using the tunnel barrier analogy it is shown to have an attractive potential associated with both the incident and exit interfaces (being symmetrical about the midpoint in $z$). This structure has been suggested by Atherton and Mather [157, 158] to posses a topological symmetry state. The study here focuses on the evolution from identical to dissimilar metallic meshes by changing the thickness of one metallic mesh layer whilst holding the second constant. The formation of a band gap region when layer $A$ dominates is shown as the band pass splits into two sub-bands. When layer $B$ dominates a defect mode that is shown to be the hybridisation of the two central resonant modes is observed. This mode increases in reflection amplitude as the thickness of layer $A, t_{mA} \to 0$ leaving a band gap between two sub bands. This result may be the realisation of the topological symmetry state. Here the main focus was the understanding of the origin of the defect modes as a hybridisation of the two central resonant modes.

The last section of this thesis contains an unique investigation into the chiral properties of a structure composed of two layers of subwavelength square arrays of square holes, and square patches arranged parallel to one another. The layers are rotated about the $z$ axis (propagation direction). When the layers are separated by a large distance each layer acts as an effective medium, however when spaced by less than twice the evanescent decay length, resonant modes with chiral EM fields occur. The polarisation conserved and converted transmission responses are experimentally recorded at normal incidence and are used to calculate the circular dichroism showing (along with the FEM modelled vector electric field profiles) the rotation of the EM field polarisation between the two arrays.

Overall the experimental and numerical studies within this thesis have shown that the microwave response of very simple square mesh based metamaterials can be manipulated in numerous ways. Experimental results are in good agreement with modelling techniques which give physical insight into the phenomena explained though the use of modelled EM field profiles. Through careful selection of the metamaterial's geometric parameters and arrangement, the transmission and reflection response can be tuned for a particular purpose.

## 9.3 Further Work

In this section some ideas for possible future study are considered. The first section relates to the work presented in Chapter 6 on the transmission response of the metallic mesh–dielectric stack. Here it is proposed that by placing a mirror midway through the stack (in the propagation direction) similar EM field profiles could be recorded leading to a tunable band of reflection minima. The second section of work relates to an extension of the work presented in Chapter 7 on the physical realisation of the topological symmetry state in a photonic structure, here proposed for an asymmetric stack of alternating thickness metallic meshes spaced by dielectric. Finally a wealth of work is suggested for the further characterisation of the structure exhibiting evanescent handedness, as presented in Chapter 8.

### 9.3.1 The EM Response of the Half Metallic Mesh–Dielectric Stack

The tunable response of metallic mesh–dielectric stacks in the microwave regime has been extensively studied throughout this thesis. Here it is proposed that by placing a flat metallic sheet, acting as a perfect mirror for microwave radiation, at the midpoint of the stack (in the propagation direction) a subset of the same EM resonant modes may be supported. Thus allowing a reduction in the microwave reflectivity response of the stack. Two schematics of suggested structures are presented in Figure 9.1 (a).

Consider the resonant modes presented in Chapter 6. For this structure four transmission peaks are experimentally observed. These correspond to four resonant modes, where each effective wavelength is determined by the combination of *cosh*-like or *sinh*-like electric field profiles in the subwavelength holes of the metallic mesh coupling the electric field in the neighbouring dielectric cavities in or out of phase. By placing a metallic plate half way through the stack the electric field profiles at the centre of the third metallic mesh must fall to zero. This implies that the *cosh*-like electric field profiles cannot be supported in the subwavelength holes of this metallic mesh, so only two of the four resonant modes may be supported. Preliminary numerical results shown in Figure 9.1 (b) indicate this to be the case, recording two reflection minima per band stop region.

However it is more interesting to consider placing the mirror at different points throughout the stack. When using a stack that contains an odd number of dielectric cavities, placing the metallic plate at the midpoint of the stack would position it in the centre of a dielectric layer. Therefore although both *cosh*-like and *sinh*-like electric field profiles would be supported in the subwavelength holes of the metallic mesh layers, only solutions with a zero at the centre of the dielectric cavity would be supported, i.e. when the dielectric cavity supports multiples of a full wavelength.

### 9.3.2 The Investigation of the Topological Symmetry State in an Asymmetric Stack

The search for the physical realisation of the topological symmetry state is briefly considered by exploring the microwave response of a symmetrical metallic mesh–dielectric

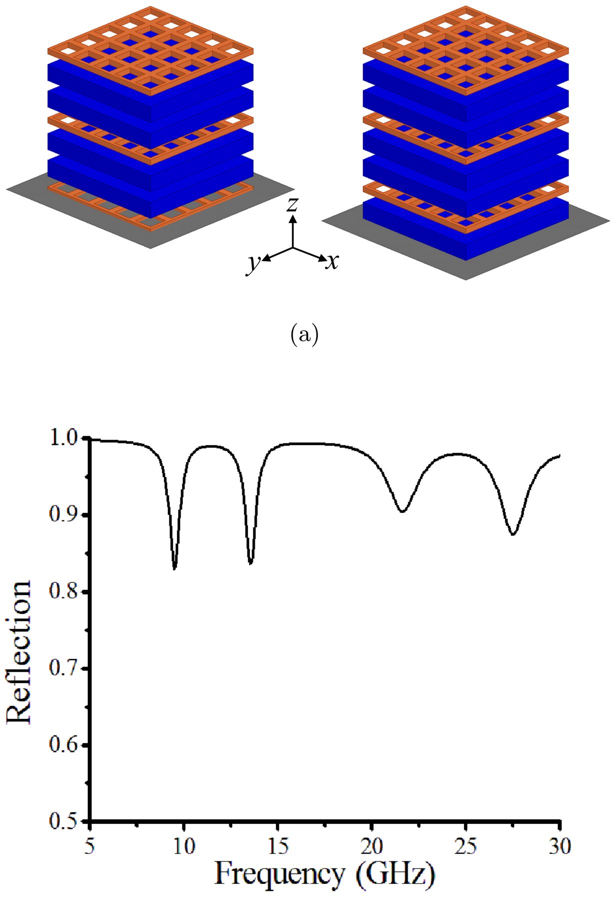

(a)

(b)

Figure 9.1: (a) Exploded schematic showing the position of the metal plate acting as a mirror for microwave radiation in a metallic mesh–dielectric stack, where the electric field falls to zero. (b) Numerically modelled reflectivity response for the metallic mesh–dielectric stack where the stack contains two metallic mesh–dielectric unit cells on a metallic ground plane (left hand schematic).

stack containing four metallic meshes of thickness $t_{mA}$ - referred to as layer $A$, and three metallic meshes of thickness $t_{mB}$ - referred to as layer $B$, which alternate through the stack and are spaced by a dielectric layer $C$. This structure is symmetrical about its mid point in the propagation direction. Consider a structure consisting of four $A$ layers and four $B$ layers (again spaced by layer $C$) as shown in Figure 9.2 (a), only one interface has an associated attractive potential that required to support the topological symmetry state.

Here the initial findings of this structure are presented. As in Chapter 7, first consider the reflection response when layers $A$ and $B$ are of equal thickness (and identical in all other dimensions), the reflection response of this structure (which now contains eight identical metallic meshes spaced by seven dielectric cavities) contains seven minima per band stop region, as shown as black dashed lines in Figures 9.3 and 9.4.

The reflectivity response as the thickness of one metallic mesh increases or decreases while the other remains constant is shown in Figures 9.3 and 9.4. The fourth mode which occurs at 16.14 GHz exponentially increases in reflection intensity, leaving a band gap between two sub-bands. This was also observed in the preliminary experimental results shown in Figure 9.1 as a small dip in the reflection intensity occurring at 16.6 GHz in the band gap region. The data was recorded for the an experimental sample with $N = 4$ $ACBC$ unit cells, with parameters as described in Chapter 7.

To understand the response of the structure when illuminated by microwave radiation, consider the case where the thickness of layer $A$ or layer $B$ tends to zero. This structure now has four metallic mesh layers separated by twice the dielectric spacer thickness ($2 \times t_d$) therefore the fourth reflection amplitude must increase to create a band gap between two sub-bands, each containing 3 resonant reflection minima. Here the three lower and three upper frequency reflection minima support a half and a full wavelength resonance respectively in each dielectric cavity.

Further investigations into this area may reveal the fourth mode that increases in reflection intensity as the EM response of one layer dominates over the other, to be a topological symmetry state in both the symmetric structure experimentally considered in Chapter 7 and the asymmetric structure noted here.

### 9.3.3 The Realisation of Evanescent Handedness in New Structures

The discovery of the evanescent handedness phenomena leads to a whole new and bespoke area of research. Firstly, simple and thorough experiments are needed to gain insight into how the angle between the arrays affects the polarisation converting modes. In Chapter 8 a commensurate rotation was used to allow the system to be modelled using a unit cell with master slave boundaries to replicate an infinite array of elements

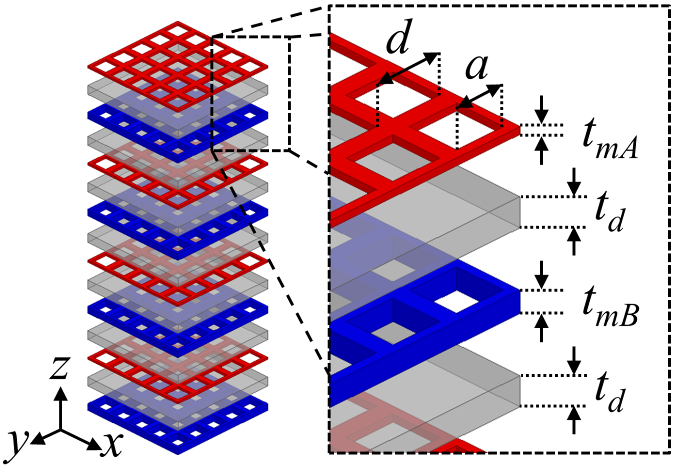

(a)

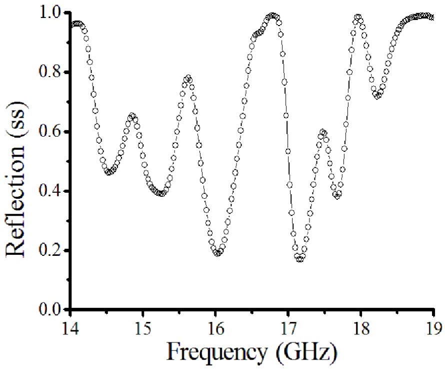

(b)

Figure 9.2: (a) Exploded schematic and (b) the experimentally recorded reflection response at $\theta = 10°$ of a $N = 4$ $ACBC$ unit cell stack where layers $A$ are not identical to layer $B$, dimensions as defined in Chapter 7.

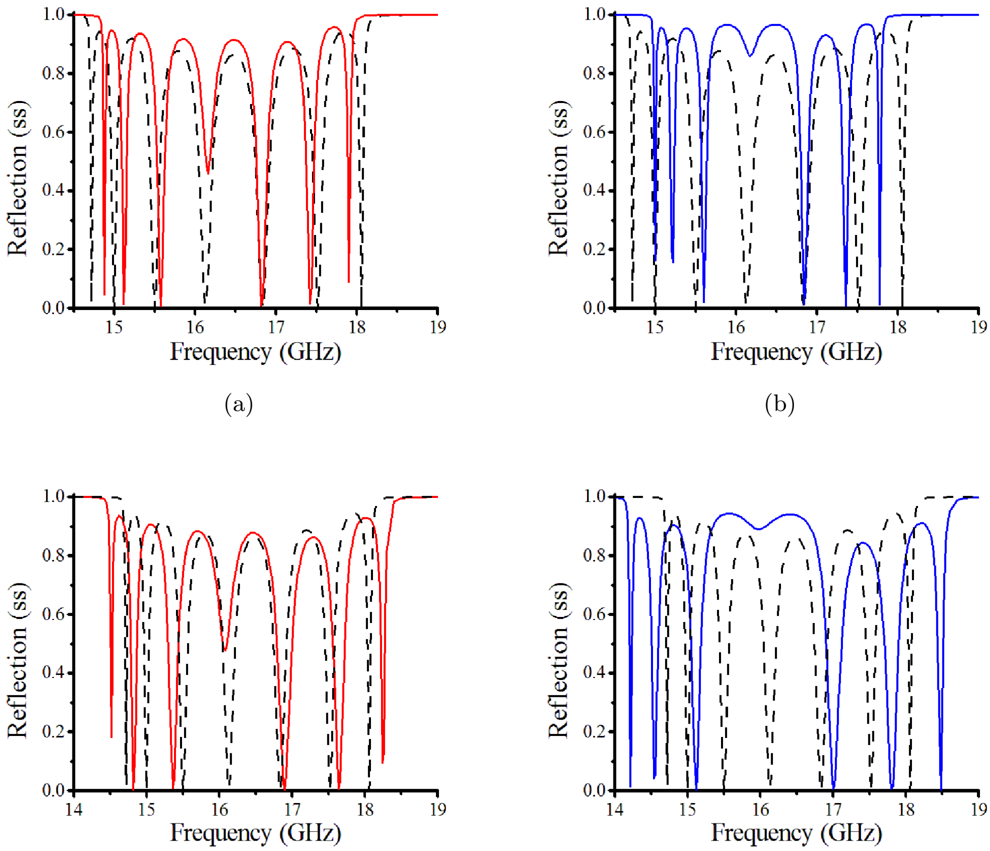

(a) (b)

(c) (d)

Figure 9.3: The numerically modelled reflection spectra at $\theta = 10°$ of a $N = 4$ $ACBC$ unit cell stack where layers $A$ is not identical to layer $B$. The thickness of metallic mesh layer $A$ is increased from $t_{mA} = 1.5$ mm (black dashed line), to (a) $t_{mA} = 2$ mm (solid red line), and (b) $t_{mA} = 2.5$ mm (solid blue line). The thickness of metallic mesh layer $A$ is reduced from $t_{mA} = 1.5$ mm (black dashed line), to (c) $t_{mA} = 1$ mm (solid red line), and (d) $t_{mA} = 0.5$ mm (solid blue line) whilst the thickness of metallic mesh layer $B$ is kept constant at $t_{mB} = 1.5$ mm.

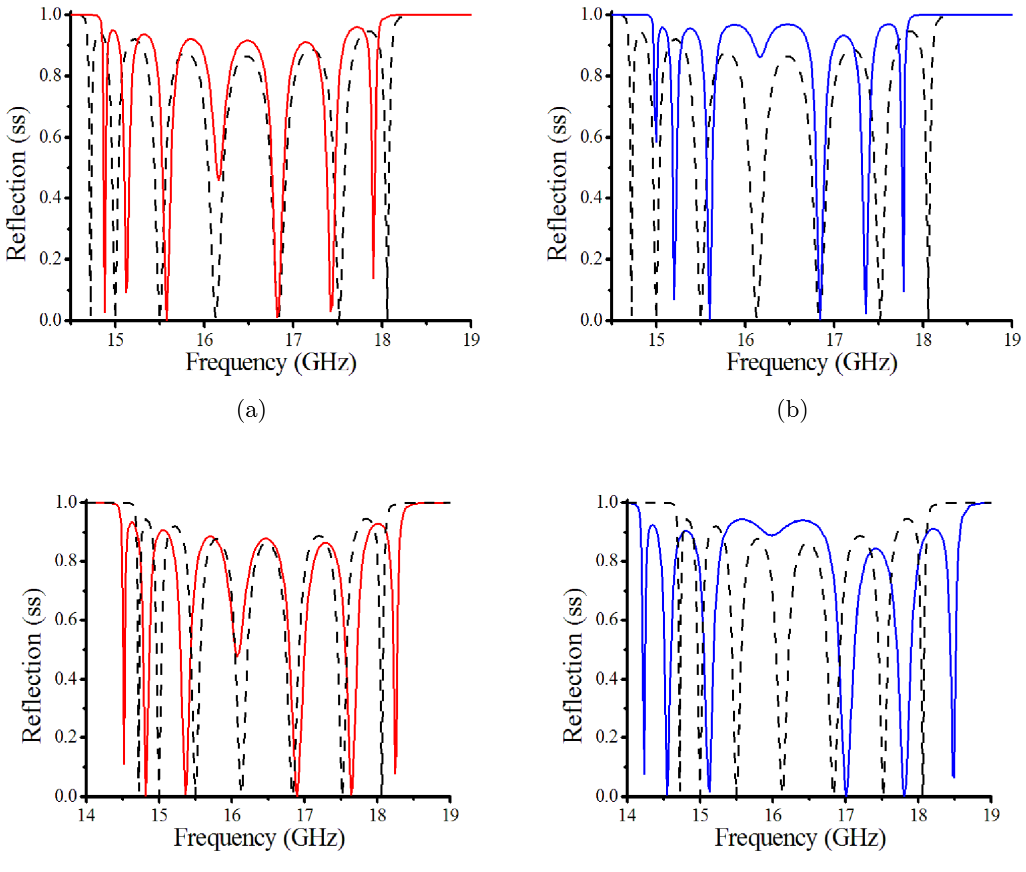

(a)

(b)

(c)

(d)

Figure 9.4: The numerically modelled reflection spectra at $\theta = 10°$ of a $N = 4$ $ACBC$ unit cell stack where layers $A$ is not identical to layer $B$. The thickness of metallic mesh layer $B$ is increased from $t_{mB} = 1.5$ mm (black dashed line), to (a) $t_{mB} = 2$ mm (solid red line), and (b) $t_{mB} = 2.5$ mm (solid blue line). The thickness of metallic mesh layer $B$ is reduced from $t_{mB} = 1.5$ mm (black dashed line), to (c) $t_{mB} = 1$ mm (solid red line), and (d) $t_{mB} = 0.5$ mm (solid blue line) whilst the thickness of metallic mesh layer $A$ is kept constant at $t_{mA} = 1.5$ mm.

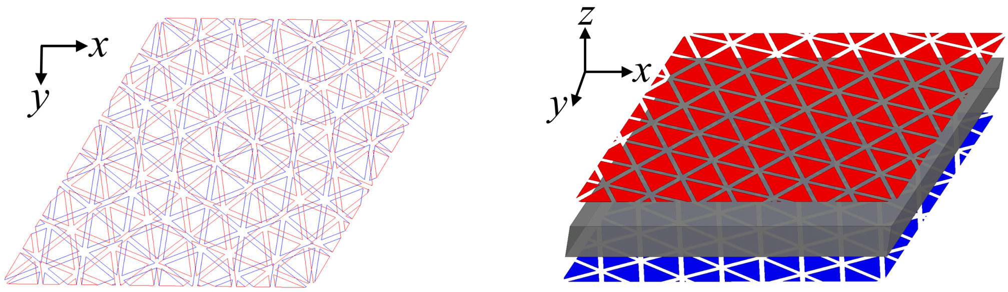

(a) (b)

Figure 9.5: Exploded schematic showing the suggested design for two arrays of hexagonal arrays of triangles separated by a distance less than twice the evanescent decay length.

in the FEM modelling software. By recording the ellipticity as a function frequency for a range of rotation angles between the arrays (labelled as $\psi$ in Figure 8.10), the rotation of the plane of polarisation could be explored along with the dependence on the transmission amplitude and frequency position of the polarisation converting modes.

Extending the concept further many layers could be used to possibly create a controlled adiabatic rotation (a small constant rotation between metallic mesh or patch array layers). It is unclear at this stage how the polarisation converting modes would be impacted by the addition of extra layers. This is beyond the capabilities of the current computational power available (even when using commensurate unit cells) and therefore is best considered experimentally.

Finally it is suggested that this evanescent chirality may be present using geometries other than the square system presented in Chapter 8. Instead a hexagonal array of triangles could be used, as shown in Figure 9.5. Even arrays of Penrose tiles (see Figure 9.6) could be rotated. As Penrose tiles have no long range diffracted orders (although they contain regular elements) this would be interesting to consider and potentially provide further evidence that this phenomena does not depend on diffraction, only that it is the evanescent near fields that interfere to support resonant modes with chiral electric fields. This occurs when the structure is considered below the cut off frequency associated with the element of the arrays used. It is suggested that this structure too could support evanescent handedness.

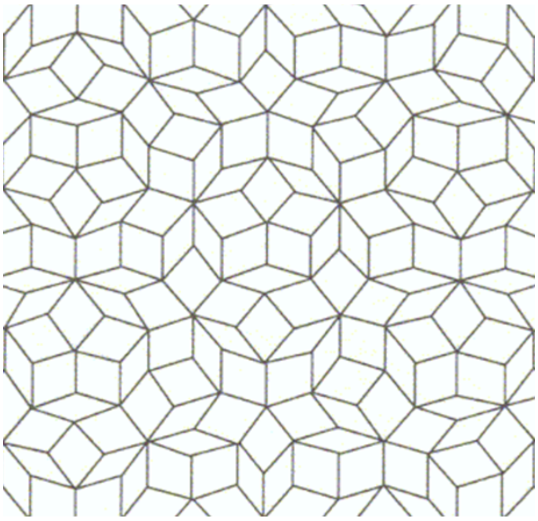

Figure 9.6: Schematic of a Penrose tile, with rhombic elements.

## 9.4 Publications

1. "Microwave transmissivity of a metamaterial–dielectric stack", Celia A. M. Butler, James Parsons, J. Roy Sambles, Alastair. P. Hibbins, Peter A. Hobson, *Applied Physics Letters*, **95**, 174101 (2009).

2. "Circuit modeling of the transmissivity of stacked two-dimensional metallic meshes", Chandra S. R. Kaipa, Alexander B. Yakolev, Francisco Medina, Francisco Mesa, Celia A. M. Butler, and Alastair P. Hibbins, *Optics Express*, **18**, 13, 13309-13320 (2010).

3. "Metamaterial tunnel barrier gives broadband microwave transmission", Celia A. M. Butler, Ian R. Hooper, Peter A. Hobson, Alastair P. Hibbins, and J. Roy Sambles, *Journal of Applied Physics*, **109**, 013104 (2011).

4. "Evanescent handedness", Celia A. M. Butler, Peter A. Hobson, Alastair P. Hibbins and J. Roy Sambles, submitted to *Physical Review B* (under review).

5. "Topological resonances in metamaterial Stacks", Timothy J. Atherton, Harsh Mathur, Melita C. Taylor, Ian R. Hooper, Alastair P. Hibbins and J. Roy Sambles, in preparation.

## 9.5 Conference Presentations

1. Oral presentation at Nanometa 2009, Celia A. M. Butler, Peter. A. Hobson, Alastair P. Hibbins and J. Roy Sambles, “The microwave response of multi-layer metamaterial-dielectric stacks”, Seefeld, Austria, 6th January 2009.

2. Poster presentation at Metamaterials (2009) conference, Celia A. M. Butler, James Parsons, Peter A. Hobson, J. Roy Sambles, and Alastair P. Hibbins, “The microwave response of a metamaterial–dielectric stack”, London, United Kingdom, 2nd September 2009.

3. Ansoft’s HFSS user conference, Basingstoke, United Kingdom, 23rd September 2009.

4. Poster Presentation at META 10, 2nd International Conference on Metamaterials, Photonic Crystals and Plasmonics, Celia A. M. Butler, Alastair P. Hibbins, J. Roy Sambles and Peter A. Hobson, “Broadband transmission thought a single layer of metamaterial clad in dielectric”, Cairo, Egypt, 22nd February 2010.

5. Poster Presentation at The Royal Society, Theo Murphy International Scientific Meeting on Metallic Metamaterials and Plasmonics, Celia A. M. Butler, Alastair P. Hibbins, J. Roy Sambles and Peter A. Hobson, “Broadband transmission thought a single layer of metamaterial clad in dielectric”, Chicheley Hall, United Kingdom, 2nd June 2010.

6. Poster Presentation at Functional Materials, Elizabeth M. G. Brock, Celia A. M. Butler, and Helen J. Rance, “Experimental Microwave Photonics”, University of Exeter, United Kingdom, 1st December 2010.

7. Poster Presentation at Metamaterials (2011) Conference, Celia A. M. Butler, Peter A. Hobson, Alastair, P. Hibbins, and J. Roy. Sambles, “Evanescent Handedness”, Barcelona, Spain, 12th October 2011.

8. Poster presentation at ONYX Celia A. M. Butler, Peter A. Hobson, Alastair P. Hibbins and J. Roy Sambles, “The microwave response of multi-layer metamaterial-dielectric stacks”, The University of Bristol, Clifton, 8th July 2011.

# References

[1] B. A. Munk, *Frequency Selective Surfaces: Theory and Design*. Wiley-Interscience, 2000. 1, 23, 24, 54, 85, 118

[2] T. K. Wu and C. H. Chan, *Frequency Selective Surfaces and Grid Array*. John Wiley and Son, Inc., 1995. 1, 23, 54, 118

[3] T. Ebbesen, H. Lezec, H. Ghaemi, T. Thio, and P. Wolff, "Extraordinary optical transmission through sub-wavelength hole arrays," *Nature*, vol. 391, no. 6668, pp. 667–669, 1998. 1, 22, 55, 72

[4] H. Bethe, "Theory of diffraction by small holes," *Physical Review*, vol. 66, pp. 163–182, Oct. 1944. 1, 16, 24, 55

[5] H. F. Ghaemi, T. Thio, D. E. Grupp, T. W. Ebbesen, and H. J. Lezec, "Surface plasmons enhance optical transmission through subwavelength holes," *Physical Review B*, vol. 58, no. 11, pp. 6779–6782, 1998. 1, 22

[6] D. M. Pozar, *Microwave Engineering*. John Wiley and Son, Inc., 2005. 5, 8, 51, 124

[7] D. M. Pozar, "A review of aperture coupled microstrip antennas: history, operation, development, and applications," Tech. Rep. May, University of Massachusetts, 1996.

[8] D. Russell, "The waveguide below-cutoff attenuation standard," *IEEE Transactions on Microwave Theory and Techniques*, vol. 45, no. 12, pp. 2408–2413, 1997.

[9] R. Levy and S. Cohn, "A History of Microwave Filter Research, Design, and Development," *IEEE Transactions on Microwave Theory and Techniques*, vol. 32, pp. 1055–1067, Sept. 1984.

[10] H. Meinel, “Commercial applications of millimeterwaves: history, present status, and future trends,” *IEEE Transactions on Microwave Theory and Techniques*, vol. 43, pp. 1639–1653, July 1995. 5

[11] M. J. Lockyear, *Electromagnetic Surface Wave Mediated Absorption and Transmission of Radiation at Microwave Frequencies.* PhD thesis, University of Exeter, Exeter, 2004. 5

[12] C. J. Bouwkamp, “Diffraction Theory,” *Reports on Progress in Physics*, vol. 17, pp. 35–100, Jan. 1954. 16

[13] A. Roberts, “Electromagnetic theory of diffraction by a circular aperture in a thick, perfectly conducting screen,” *Journal of the Optical Society of America A*, vol. 4, pp. 1970–1983, Oct. 1987. 16

[14] F. J. García de Abajo, R. Gómez-Medina, and J. J. Sáenz, “Full transmission through perfect-conductor subwavelength hole arrays,” *Physical Review E*, vol. 72, no. 1, pp. 3–6, 2005. 16, 26

[15] R. Gordon, “Bethes aperture theory for arrays,” *Physical Review A*, vol. 76, p. 053806, Nov. 2007. 16

[16] M. Babinet, “No Title,” *Comptes Rendus de lAcadémie des Sciences*, vol. 4, p. 638, 1837. 16, 118

[17] J. Zenneck, “Uber Die Fortpflanzung Ebener Elektromagnetischer Wellen Langes Einer Ebenen Leiterflache Und Ihre Beziehung Zur Dratlosen Teleprahie (German),” pp. 846–866, 1907. 17

[18] A. Sommerfeld, “Uber die fortpflanzung electrodynamischer wellen langs eines drahtes,” *Annlen der Physik and Chemie*, vol. 67, p. 233, 1899. 17

[19] H. M. Barlow and A. L. Cullen, “Surface Waves.” 17, 23

[20] R. W. Wood, “On a Remarkable Case of Uneven Distribution of Light in a Diffraction Grating Spectrum,” *Proceedings of the Physical Society of London*, vol. 18, pp. 269–275, June 1902. 17

[21] L. Rayleigh, “On the dynamical theory of gratings,” *Proceedings of the Royal Society of London. Series A*, vol. 79, no. 532, pp. 399–416, 1907. 17

[22] U. Fano, “The theory of anomalous diffraction gratings and of quasi-stationary waves on metallic surfaces (Sommerfelds waves),” *Journal of the Optical Society of America*, vol. 31, p. 213, Mar. 1941. 17

[23] R. Ritchie, "Plasma losses by fast electrons in thin films," *Physical Review*, vol. 106, pp. 874–881, June 1957. 18

[24] C. Powell and J. Swan, "Effect of oxidation on the characteristic loss spectra of aluminum and magnesium," *Physical Review*, vol. 118, pp. 640–643, May 1960. 18

[25] H. Raether, *Surface Plasmons on Smooth and Rough Surfaces and on Gratings*. Springer-Verlag, 1988. 18

[26] S. A. Maier, *Plasmonics: Fundamentals and Applications*. Springer, 2007. 18

[27] F. Yang, J. R. Sambles, and G. W. Bradberry, "Long-range surface modes supported by thin films," *Physical Review B*, vol. 44, pp. 5855–5872, Sept. 1991. 18

[28] P. Drude, "Zur elektronentheorie der metalle," 1889. 19

[29] T. Thio, H. F. Ghaemi, H. J. Lezec, P. A. Wolff, and T. W. Ebbesen, "Surface-plasmon-enhanced transmission through hole arrays in Cr films," *Journal of the Optical Society of America B*, vol. 16, p. 1743, Oct. 1999. 22, 112

[30] J. A. Porto, F. J. García-Vidal, J. B. Pendry, and F. J. Garcia-Vidal, "Transmission Resonances on Metallic Gratings with Very Narrow Slits," *Physical Review Letters*, vol. 83, pp. 2845–2848, Oct. 1999. 22

[31] M. M. J. Treacy, "Dynamical diffraction explanation of the anomalous transmission of light through metallic gratings," *Physical Review B*, vol. 66, p. 195105, Nov. 2002.

[32] U. Schröter and D. Heitmann, "Surface-plasmon-enhanced transmission through metallic gratings," *Physical Review B*, vol. 58, pp. 15419–15421, Dec. 1998. 22

[33] S. Enoch, E. Popov, M. Neviere, and R. Reinisch, "Enhanced light transmission by hole arrays," *Journal of Optics A: Pure and Applied Optics*, vol. 4, pp. S83–S87, Sept. 2002. 22

[34] A. Krishnan, T. Thio, T. J. Kim, H. J. Lezec, T. W. Ebbesen, P. A. Wolff, J. Pendry, L. Martin-Moreno, and Garcia-Vidal, "Evanescently coupled resonance in surface plasmon enhanced transmission," *Optics Communications*, vol. 200, pp. 1–7, Dec. 2001.

[35] W. Barnes, W. Murray, J. Dintinger, E. Devaux, and T. Ebbesen, "Surface plasmon polaritons and their role in the enhanced transmission of light through periodic arrays of subwavelength holes in a metal film," *Physical Review Letters*, vol. 92, p. 107401, Mar. 2004.

[36] L. Salomon, F. Grillot, A. Zayats, and F. de Fornel, "Near-field distribution of pptical transmission of periodic subwavelength holes in a metal film," *Physical Review Letters*, vol. 86, pp. 1110–1113, Feb. 2001. 22

[37] M. Sun, J. Tian, S. Han, Z. Li, B. Cheng, D. Zhang, A. Jin, and H. Yang, "Effect of the subwavelength hole symmetry on the enhanced optical transmission through metallic films," *Journal of Applied Physics*, vol. 100, no. 2, p. 024320, 2006. 22

[38] F. Przybilla, C. Genet, T. W. Ebbesen, and C. Geneta, "Enhanced transmission through Penrose subwavelength hole arrays," *Applied Physics Letters*, vol. 89, p. 121115, 2006.

[39] T. Matsui, A. Agrawal, A. Nahata, and Z. V. Vardeny, "Transmission resonances through aperiodic arrays of subwavelength apertures," *Nature*, vol. 446, pp. 517–521, 2007.

[40] N. Papasimakis, V. A. Fedotov, A. S. Schwanecke, N. I. Zheludev, and F. J. Garcia de Abajo, "Enhanced microwave transmission through quasicrystal hole arrays," *Applied Physics Letters*, vol. 91, p. 081503, 2007. 22

[41] A. Mary, S. G. Rodrigo, L. Martín-Moreno, and F. J. García-Vidal, "Plasmonic metamaterials based on holey metallic films," *Journal of Physics: Condensed Matter*, vol. 20, no. 30, p. 304215, 2008. 22, 72

[42] C. Genet and T. Ebbesen, "Light in tiny holes," *NATURE-LONDON-*, vol. 445, no. 7123, p. 39, 2007. 23

[43] C. E. Stewart, I. R. Hooper, and J. R. Sambles, "Surface plasmon differential ellipsometry of aqueous solutions for bio-chemical sensing," *Journal of Physics D: Applied Physics*, vol. 41, p. 105408, May 2008. 23

[44] C. Cutler, "Genesis of the corrugated electromagnetic surface," in *Proceedings of IEEE Antennas and Propagation Society International Symposium and URSI National Radio Science Meeting*, vol. 3, pp. 1456–1459, IEEE, 1994. 23

[45] P. A. R. Ade, G. Pisano, C. Tucker, and S. Weaver, "A review of metal mesh filters," in *Proceedings of SPIE*, vol. 6275, pp. 62750U–62750U–15, 2006. 23, 54

[46] C. Chen, "Transmission of Microwave Through Perforated Flat Plates of Finite Thickness," *IEEE Transactions on Microwave Theory and Techniques*, vol. 21, pp. 1–6, Jan. 1973.

[47] R. Ulrich, "Submillimeter waveguiding on periodic metal structure," *Applied Physics Letters*, vol. 22, no. 5, p. 251, 1973.

[48] R. Ulrich, "Effective low-pass filters for far infrared frequencies," *Infrared Physics*, vol. 7, pp. 65–74, June 1967. 23

[49] R. Mittra, C. Chan, and T. Cwik, "Techniques for analyzing frequency selective surfaces-a review," *Proceedings of the IEEE*, vol. 76, no. 12, pp. 1593–1615, 1988. 23

[50] H. J. Lezec, A. Degiron, E. Devaux, R. A. Linke, L. Martin-moreno, F. J. Garcia-Vidal, and T. W. Ebbesen, "Beaming light from a subwavelength aperture.," *Science*, vol. 297, pp. 820–822, Aug. 2002. 24

[51] L. Martín-Moreno, F. García-Vidal, H. Lezec, A. Degiron, and T. Ebbesen, "Theory of highly directional emission from a single subwavelength aperture surrounded by surface corrugations," *Physical Review Letters*, vol. 90, p. 167401, Apr. 2003.

[52] F. J. Garcia-vidal, H. J. Lezec, T. W. Ebbesen, and L. Martin-Moreno, "Multiple paths to enhance optical transmission through a single subwavelength slit," *Physical Review Letters*, vol. 90, p. 213901, 2003. 24

[53] A. Sihvola, "Metamaterials in electromagnetics," *Metamaterials*, vol. 1, pp. 2–11, Mar. 2007. 25, 29

[54] H. A. Macleod, *Thin film optical filters (3rd Edition)*. Birstol and Philadelphia: Institute of Physics Publishing, 2001. 25, 71

[55] J. B. Pendry, L. Martín-Moreno, and F. J. Garcia-Vidal, "Mimicking surface plasmons with structured surfaces," *Science (New York, N.Y.)*, vol. 305, pp. 847–8, Aug. 2004. 25, 26, 42

[56] F. J. Garcia-Vidal, L. Martín-Moreno, and J. B. Pendry, "Surfaces with holes in them: new plasmonic metamaterials," *Journal of Optics A: Pure and Applied Optics*, vol. 7, pp. S97–S101, Feb. 2005. 25

[57] E. Stone and E. Hendry, "Dispersion of spoof surface plasmons in open-ended metallic hole arrays," *Physical Review B*, vol. 84, p. 035418, July 2011. 26, 42

[58] E. Hendry, A. P. Hibbins, and J. R. Sambles, "Importance of diffraction in determining the dispersion of designer surface plasmons," *Physical Review B*, vol. 78, p. 235426, 2008. 26

[59] A. P. Hibbins, B. R. Evans, and J. R. Sambles, "Experimental verification of designer surface plasmons," *Science*, vol. 308, pp. 670–672, Apr. 2005. 27

[60] A. P. Hibbins, M. J. Lockyear, I. R. Hooper, and J. R. Sambles, "Waveguide arrays as plasmonic metamaterials: transmission below cutoff," *Physical Review Letters*, vol. 96, p. 073904, 2006.

[61] M. Lockyear, A. Hibbins, and J. Sambles, "Microwave surface-plasmon-like modes on thin metamaterials," *Physical Review Letters*, vol. 102, p. 073901, Feb. 2009. 27

[62] E. Shamonina and L. Solymar, "Metamaterials: how the subject started," *Metamaterials*, vol. 1, pp. 12–18, Mar. 2007. 29

[63] V. G. Veselago, "The electrodynamics of surfaces with simultaneously negative values of permittivity and permeability," *Soviet Physics Uspekhi*, vol. 10, pp. 509–514, Apr. 1968. 29

[64] D. R. Smith, W. J. W. Padilla, D. C. Vier, S. C. S. C. Nemat-Nasser, and S. Schultz, "Composite medium with simultaneously negative permeability and permittivity," *Physical Review Letters*, vol. 84, pp. 4184–4187, May 2000. 29, 57

[65] J. Pendry, A. Holden, D. Robbins, and W. Stewart, "Magnetism from conductors and enhanced nonlinear phenomena," *IEEE tTansactions on Microwave Theory and Techniques*, vol. 47, no. 11, pp. 2075–2084, 1999. 29

[66] J. B. Pendry, A. J. Holden, W. J. Stewart, I. Youngs, and I, "Extremely low frequency plasmons in metallic mesostructures," *Phys. Rev. Lett.*, vol. 76, no. 25, pp. 4773–4776, 1996. 29

[67] R. Shelby, D. Smith, and S. Schultz, "Experimental verification of a negative index of refraction," *Science*, vol. 292, pp. 77–79, 2001. 29

[68] J. Pendry, “Negative refraction makes a perfect lens,” *Physical Review Letters*, vol. 85, pp. 3966–3969, Oct. 2000. 29, 72

[69] D. R. Smith, J. B. Pendry, and M. C. K. Wiltshire, “Metamaterials and negative refractive index.,” *Science (New York, N.Y.)*, vol. 305, no. 5685, pp. 788–92, 2004. 29

[70] J. Shin, J.-T. Shen, and S. Fan, “Three-dimensional metamaterials with an ultrahigh effective refractive index over a broad bandwidth,” *Physical Review Letters*, vol. 102, p. 093903, Mar. 2009. 29

[71] D. Schurig, J. J. Mock, B. J. Justice, S. a. Cummer, J. B. Pendry, a. F. Starr, and D. R. Smith, “Metamaterial electromagnetic cloak at microwave frequencies.,” *Science (New York, N.Y.)*, vol. 314, pp. 977–80, Nov. 2006. 29

[72] J. B. Pendry, D. Schurig, and D. R. Smith, “Controlling electromagnetic fields,” *Science*, vol. 312, pp. 1780–2, June 2006.

[73] U. Leonhardt, “Optical conformal mapping,” *Science*, vol. 312, pp. 1777–80, June 2006.

[74] U. Leonhardt, “Optical Conformal Mapping and Dielectric Invisibility Devices,” *arxiv.org*, p. Physics/0602092, 2006.

[75] A. Alù and N. Engheta, “Plasmonic and metamaterial cloaking: physical mechanisms and potentials,” *Journal of Optics A: Pure and Applied Optics*, vol. 10, p. 093002, Sept. 2008.

[76] A. Alù and N. Engheta, “Achieving transparency with plasmonic and metamaterial coatings,” *Physical Review E*, vol. 72, p. 016623, July 2005. 29

[77] M. Gil, J. Bonache, and F. Martin, “Metamaterial filters: a review,” *Metamaterials*, vol. 2, no. 4, pp. 186–197, 2008. 29

[78] O. Sakai and K. Tachibana, “Plasmas as metamaterials: a review,” *Plasma Sources Science and Technology*, vol. 21, p. 013001, 2012.

[79] K. Bliokh, Y. Bliokh, V. Freilikher, S. Savelev, and F. Nori, “Colloquium: Unusual resonators: plasmonics, metamaterials, and random media,” *Reviews of Modern Physics*, vol. 80, pp. 1201–1213, Oct. 2008. 29

[80] B. Archambeault, “Software simulation tools for EMC control of high-speed signals,” tech. rep., 2007. 32

[81] K. Yee, "Numerical solution of initial boundary value problems involving maxwell's equations in isotropic media," *IEEE Transactions on Antennas and Propagation*, vol. 14, no. 3, pp. 302 – 307, 1996. 32

[82] W. C. Gibson, *The Method of Moments in Electromagnetics.* Boca Raton, USA: Chapman and Hall/CRC, 2008. 32

[83] "HFSS, Ansoft Corporation, Pittsburgh, PA, USA." 32, 33, 111

[84] "HFSS Technical Notes," tech. rep., Ansoft. 35

[85] D. Edgar, "HFSS: Hybrid FE-BI for efficient simulation for antenna and fields," tech. rep., HFSS, Ansoft Corporation, 2011. 35

[86] S. Tretyakov, *Analytical Modeling in Applied Electromagnetics.* Artech House, 2003. 36

[87] C. S. R. Kaipa, A. B. Yakovlev, F. Medina, F. Mesa, C. A. M. Butler, and A. P. Hibbins, "Circuit modeling of the transmissivity of stacked two-dimensional metallic meshes," *Optics Express*, vol. 18, p. 13309, June 2010. 41

[88] M. C. Taylor, A. P. Hibbins, and J. R. Sambles, "The electromagnetic response of closely spaced metal meshes," *Physical Review B*, vol. (accepted), 2012. 42, 63, 83, 120, 125

[89] M. Taylor, *Modelling the microwave response of metal arrays using modal matching.* PhD thesis, University of Exeter, 2012. 42, 98

[90] "Flann Microwave: Microwave Products, Bodmin, United Kingdom," 2010. 44, 50, 51

[91] A. P. Hibbins, *Grating coupling of surface plasmon polaritons at visible and microwave frequencies.* PhD thesis, University of Exeter, 1999. 46

[92] E. M. G. Brock, E. Hendry, and A. P. Hibbins, "Subwavelength lateral confinement of microwave surface waves," *Applied Physics Letters*, vol. 99, no. 5, p. 051108, 2011. 52

[93] M. Gedny, "VectorStar Training Course, Exeter," tech. rep., Anritsu, 2009. 52

[94] Unknown, *The Essentials of Vector Network Analysis.* Anritsu (USA), 2009. 52

[95] J. M. Lamarre, N. Coron, R. Courtin, G. Dambier, and M. Charra, "Metallic mesh properties and design of submillimeter filters," *International Journal of Infrared and Millimeter Waves*, vol. 2, no. 2, pp. 273–292, 1981. 54

[96] R. Ulrich, "Interference Filters for the Far Infrared," *Applied Optics*, vol. 7, p. 1987, Oct. 1968. 54

[97] F. J. Garcia-Vidal, T. W. Ebbesen, and L. Kuipers, "Light passing through subwavelength apertures," *Reviews of Modern Physics*, vol. 82, pp. 729–787, Mar. 2010. 55

[98] J. Bravo-Abad, L. Martín-Moreno, F. García-Vidal, E. Hendry, and J. Gómez Rivas, "Transmission of light through periodic arrays of square holes: From a metallic wire mesh to an array of tiny holes," *Physical Review B*, vol. 76, p. 241102, 2007. 55

[99] R. Dragila, B. Luther-Davies, and S. Vukovic, "High transparency of classically opaque metallic films," *Physical Review Letters*, vol. 55, no. 10, pp. 1117–1120, 1985. 55

[100] R. Ortuño, C. García-Meca, F. J. Rodríguez-Fortuño, J. Martí, and A. Martínez, "Multiple extraordinary optical transmission peaks from evanescent coupling in perforated metal plates surrounded by dielectrics," *Optics Express*, vol. 18, pp. 7893–7898, Mar. 2010. 55

[101] I. R. Hooper, T. W. Preist, and J. R. Sambles, "Making tunnel barriers (including metals) transparent," *Physical Review Letters*, vol. 97, no. 5, p. 53902, 2006. 55, 64, 76

[102] C. Fabry and A. Perot, "Théorie et applications d'une nouvelle méthode de Spectroscopie Interferentielle," *Annales des Chimie et des Physique*, vol. 16, pp. 115–144, 1899. 56, 61

[103] L. Zhou, W. Wen, C. Chan, and P. Sheng, "Electromagnetic-wave tunneling through negative-permittivity media with high magnetic fields," *Physical Review Letters*, vol. 94, p. 243905, June 2005. 56

[104] B. Hou, H. Wen, Y. Leng, and W. Wen, "Electromagnetic wave transmission through subwavelength metallic meshes sandwiched between split rings," *Applied Physics Letters*, vol. 87, no. 20, p. 201114, 2005. 57, 88

[105] V. Lomakin and E. Michielssen, “Enhanced transmission through metallic plates perforated by arrays of subwavelength holes and sandwiched between dielectric slabs,” *Physical Review B*, vol. 71, p. 235117, June 2005. 57

[106] “Eurotech, PCB manufacturer, Exmouth, United Kingdom.” 58

[107] M. Born and E. Wolff, *Principles of Optics*. Cambridge University Press, 2002. 60

[108] M. R. Gadsdon, J. Parsons, and J. R. Sambles, “Electromagnetic resonances of a multilayer metal/dielectric stack,” *Journal of optical society of america B*, vol. 26, no. 4, pp. 734–742, 2009. 62, 72, 76, 92

[109] D. R. Smith and S. Schultz, “Determination of effective permittivity and permeability of metamaterials from reflection and transmission coefficients,” *Physical Review B*, vol. 65, p. 195104, Apr. 2002. 63

[110] W. Geffcken, “Deutsches Reich Patentschrift,” 1939. 71

[111] W. Zhang, X. Lei, Z. Wang, D. Zheng, W. Tam, C. Chan, and P. Sheng, “Robust photonic band gap from tunable scatterers,” *Physical Review Letters*, vol. 84, pp. 2853–2856, Mar. 2000. 72

[112] M. Scalora, G. D’Aguanno, N. Mattiucci, M. Bloemer, D. de Ceglia, N. Akozbek, M. Cappeddu, M. Fowler, and J. Haus, “Negative refraction and sub-wavelength focusing in the visible range using transparent metallo-dielectric stacks,” *Optics Express*, vol. 15, no. 2, pp. 508–523, 2007. 72

[113] M. Scalora, M. J. Bloemer, A. S. Pethel, J. P. Dowling, C. M. Bowden, and A. S. Manka, “Transparent, metallo-dielectric, one-dimensional, photonic band-gap structures,” *Journal of Applied Physics*, vol. 83, no. 5, p. 2377, 1998. 72

[114] R. Sauleau, P. Coquet, J. P. Daniel, T. Matsui, H. Hirose, and N. Hirose, “Study of Fabry-Perot cavities with metal mesh mirrors using equivalent circuit modes. Comparison with experimental results in the 60 GHz band,” *International Journal of Infrared and Millimeter Waves*, vol. 19, no. 12, pp. 1693–1710, 1998. 72

[115] V. Kuzmiak, A. Maradudin, and F. Pincemin, “Photonic band structures of two-dimensional systems containing metallic components,” *Physical Review B*, vol. 50, pp. 16835–16844, Dec. 1994.

[116] V. Kuzmiak and A. A. Maradudin, “Photonic band structures of one- and two-dimensional periodic systems with metallic components in the presence of dissipation,” *Physical Review B*, vol. 55, pp. 7427–7444, Mar. 1997. 72

[117] R. Ortuño, C. García-Meca, F. Rodríguez-Fortuño, J. Martí, and A. Martínez, “Role of surface plasmon polaritons on optical transmission through double layer metallic hole arrays,” *Physical Review B*, vol. 79, p. 075425, Feb. 2009. 72

[118] M. Beruete, M. Sorolla, M. Navarro-Cía, and I. Campillo, “Polarized left-handed extraordinary optical transmission of subterahertz waves.,” *Optics Express*, vol. 15, pp. 8125–34, June 2007.

[119] T. Li, J.-Q. Li, F.-M. Wang, Q.-J. Wang, H. Liu, S.-N. Zhu, and Y.-Y. Zhu, “Exploring magnetic plasmon polaritons in optical transmission through hole arrays perforated in trilayer structures,” *Applied Physics Letters*, vol. 90, p. 251112, 2007.

[120] M. Notomi, “Negative refraction in photonic crystals,” *Optical and Quantum Electronics*, vol. 34, pp. 133–143, 2002.

[121] E. Cubukcu, K. Aydin, E. Ozbay, S. Foteinopoulou, and C. M. Soukoulis, “Electromagnetic waves: Negative refraction by photonic crystals,” *Nature*, vol. 423, pp. 604–605, 2003.

[122] S. Zhang, W. Fan, N. C. Panoiu, K. J. Malloy, R. M. Osgood, and S. R. J. Brueck, “Experimental Demonstration of Near-Infrared Negative-Index Metamaterials,” *Physical Review Letters*, vol. 95, pp. 1–4, Sept. 2005. 73

[123] S. Zhang, W. Fan, K. J. Malloy, S. J. Brueck, N. C. Panoiu, and R. M. Osgood, “Near-infrared double negative metamaterials,” *Optics Express*, vol. 13, no. 13, p. 4922, 2005.

[124] G. Dolling, M. Wegener, C. M. Soukoulis, and S. Linden, “Negative-index metamaterial at 780 nm wavelength,” *Optics Letters*, vol. 32, no. 1, pp. 53–55, 2007.

[125] G. Dolling, C. Enkrich, M. Wegener, C. M. Soukoulis, and S. Linden, “Simultaneous negative phase and group velocity of light in a metamaterial.,” *Science*, vol. 312, pp. 892–4, May 2006. 72, 73

[126] M. Beruete, M. Sorolla, and I. Campillo, “Inhibiting left-handed wave propagation by a band gap of stacked cut-off metallic hole arrays,” *IEEE Microwave and Wireless Components Letters*, vol. 7, no. 1, pp. 1309–1531, 2007. 72

[127] M. Beruete, M. Sorolla, and I. Campillo, “Left-handed extraordinary optical transmission through a photonic crystal of subwavelength hole arrays,” *Optics Express*, vol. 14, no. 12, p. 5445, 2006. 73

[128] M. Beruete, M. Navarro-Cía, F. Falcone, I. Campillo, and M. Sorolla, “Connection between extraordinary transmission and negative refraction in a prism of stacked sub-wavelength hole arrays,” *Journal of Physics D: Applied Physics*, vol. 42, p. 165504, Aug. 2009.

[129] M. Beruete, M. Navarro-Cía, M. Sorolla, and I. Campillo, “Negative refraction through an extraordinary transmission left-handed metamaterial slab,” *Physical Review B*, vol. 79, p. 191507, 2009.

[130] M. Beruete, M. Navarro-Cía, and M. Sorolla, “Strong lateral displacement in polarization anisotropic extraordinary transmission metamaterial,” *New Journal of Physics*, vol. 12, p. 063037, June 2010.

[131] M. Beruete, M. Navarro-Cía, M. Sorolla, and I. Campillo, “Planoconcave lens by negative refraction of stacked subwavelength hole arrays.,” *Optics Express*, vol. 16, pp. 9677–83, June 2008.

[132] M. Beruete, M. Navarro-Cia, I. Campillo, F. Flacone, I. Arnedo, and M. Sorolla, “Parametrical study of left-handed or right-handed propagation by stacking hole arrays,” *Optical and Quantum Electronics*, vol. 39, no. 4-6, pp. 285–293, 2007.

[133] M. Navarro-Cia, M. Beruete, M. Sorolla, and I. Campillo, “Negative refraction in a prism made of stacked subwavelength hole arrays,” *Optics Express*, vol. 16, no. 2, pp. 560–566, 2008.

[134] M. Navarro-Cía, M. Beruete, M. Sorolla, and I. Campillo, “Viability of focusing effect by left-handed stacked subwavelength hole arrays,” *Physica B: Condensed Matter*, vol. 405, no. 14, pp. 10–14, 2010.

[135] A. Mary, S. G. Rodrigo, F. J. Garcia-Vidal, and L. Martin-Moreno, “Theory of negative-refractive-index response of double-fishnet structures,” *Physical Review Letters*, vol. 101, no. 10, pp. 2–5, 2008. 73

[136] A. Alù and N. Engheta, “Evanescent growth and tunneling through stacks of frequency-selective surfaces,” *IEEE Antennas and Wireless Propagation Letters*, vol. 4, no. 11, p. 417, 2005. 72

[137] V. M. Shalaev, “Optical negative-index metamaterials,” *Nature Photonics*, vol. 1, pp. 41–48, Jan. 2007. 73

[138] M. Kafesaki, I. Tsiapa, N. Katsarakis, T. Koschny, C. Soukoulis, and E. Economou, “Left-handed metamaterials: The fishnet structure and its variations,” *Physical Review B*, vol. 75, p. 235114, June 2007. 73

[139] C. A. M. Butler, I. R. Hooper, A. P. Hibbins, J. R. Sambles, and P. A. Hobson, “Metamaterial tunnel barrier gives broadband microwave transmission,” *Journal of Applied Physics*, vol. 109, p. 013104, 2011. 76

[140] M. Scalora, M. J. Bloemer, and C. M. Bowden, “Laminated photonic band structures with high conductivity and high transparency: metals under a new light,” *Optics and Photonics News*, vol. 10, p. 24, Sept. 1999. 85

[141] H. Wen, B. Hou, Y. Leng, and W. Wen, “Resonance-induced wave penetration through electromagnetic opaque object,” *Optics Express*, vol. 13, pp. 7005–10, Sept. 2005. 88

[142] H. Wen, B. Hou, Y. Leng, and W. Wen, “Enhanced transmission of electromagnetic waves through metamaterials,” *Applied Physics A*, vol. 87, pp. 217–221, Jan. 2007.

[143] W. Wen, L. Zhou, B. Hou, C. T. Chan, and P. Sheng, “Resonant transmission of microwaves through subwavelength fractal slits in a metallic plate,” *Physical Review B*, vol. 72, p. 153406, 2005.

[144] R. P. Drupp, J. A. Bossard, Y.-h. Ye, D. H. Werner, and T. S. Mayer, “Dual-band infrared single-layer metallodielectric photonic crystals,” *Applied Physics Letters*, vol. 85, no. 10, pp. 1835–1837, 2004. 88

[145] E. Ozbay, A. Abeyta, G. Tuttle, M. Tringides, R. Biswas, C. T. Chan, C. M. Soukoulis, and K. Ho, “Measurement of a three-dimensional photonic band gap in a crystal structure made of dielectric rods,” *Physical Review B*, vol. 50, no. 3, pp. 1945–1948, 1994. 89

[146] K. Ho, C. Chan, C. Soukoulis, R. Biswas, and M. Sigalas, “Photonic band gaps in three dimensions: New layer-by-layer periodic structures,” *Solid State Communications*, vol. 89, pp. 413–416, Feb. 1994.

[147] S. Lin, J. Fleming, D. Hetherington, B. Smith, R. Biswas, K. Ho, M. M. Sigalas, W. Zubrzycki, S. R. Kurtz, and J. Bur, "A three-dimensional photonic crystal operating at infrared wavelengths," *Nature*, vol. 394, pp. 251–253, 1998. 89

[148] Z.-Y. Li, I. El-Kady, K.-M. Ho, S. Y. Lin, and J. G. Fleming, "Photonic band gap effect in layer-by-layer metallic photonic crystals," *Journal of Applied Physics*, vol. 93, no. 1, p. 38, 2003. 89

[149] P. Sun and J. D. Williams, "Passband modes beyond waveguide cutoff in metallic tilted-woodpile photonic crystals.," *Optics Express*, vol. 19, pp. 7373–80, Apr. 2011.

[150] A. Chang, Y. Kim, M. Chen, and Z. Yang, "Visible three-dimensional metallic photonic crystal with non-localized propagating modes beyond waveguide cutoff," *Optics Express*, vol. 15, no. 13, pp. 8428–8437, 2007.

[151] J. Fleming, S. Lin, I. El-Kady, and R. Biswas, "All-metallic three-dimensional photonic crystals with a large infrared bandgap," *Nature*, vol. 417, pp. 1548–1551, 2002. 89

[152] E. Ozbay, B. Temelkuran, M. Sigalas, G. Tuttle, C. M. Soukoulis, and K. M. Ho, "Defect structures in metallic photonic crystals," *Applied Physics Letters*, vol. 69, no. 25, p. 3797, 1996. 89

[153] W. Y. Leung, G. Tuttle, M. M. Sigalas, R. Biswas, and K. M. Ho, "Optimizing the Q value in three-dimensional metallic photonic band gap crystals," *Journal of Applied Physics*, vol. 84, p. 4091, 1998. 89

[154] J. S. McCalmont, M. M. Sigalas, G. Tuttle, K.-M. Ho, and C. M. Soukolis, "A layer-by-layer metallic photonic band-gap structure," *Applied Physics Letters*, vol. 68, no. 19, p. 2759, 1996. 89

[155] C. A. M. Butler, J. Parsons, J. R. Sambles, A. P. Hibbins, and P. A. Hobson, "Microwave transmissivity of a metamaterial-dielectric stack," *Applied Physics Letters*, vol. 95, no. 17, p. 174101, 2009. 92

[156] B. Mendelson, *Introduction to Topology*. Courier Dover Publications, 1990. 100

[157] T. Atherton and H. Mathur, "A Photonics Analogy to Topological Insulators," tech. rep., Case Western University, 2010. 100, 135

[158] T. Atherton and H. Mathur, "Topological states in one dimensional solids and photonic crystals," tech. rep., Case Western University, 2011. 100, 135

[159] L. Kelvin, *Baltimore Lectures on Molecular Dynamics and the Wave Theory of Light*. London: Clay and Sons, Cambridge University Press Warehouse, 1904. 103

[160] W. G. McBride, "Thalidomide embryopathy," *Teratology*, vol. 16, pp. 79–82, Aug. 1977. 104

[161] M. T. Miller and K. Strömland, "Teratogen update: Thalidomide: a review, with a focus on ocular findings and new potential uses," *Teratology*, vol. 60, pp. 306–21, Nov. 1999. 104

[162] M. Melchert and A. List, "The Thalidomide saga," *The International Journal of Biochemistry & Cell Biology*, vol. 39, pp. 1489–99, Jan. 2007. 104

[163] W. G. McBride, "Thalidomide and Congenital abnormalities," *The Lancet*, vol. 278, p. 1358, Jan. 1961. 104

[164] W. Lenz, R. Pfeiffer, W. Kosenow, and D. Hayman, "Thalidomide and congenital abnormalities," *The Lancet*, vol. 279, pp. 45–46, Jan. 1962.

[165] R. Smithells, "Thalidomide and malformations in Liverpool," *The Lancet*, vol. 279, pp. 1270–1273, June 1962. 104

[166] T. Ito, H. Ando, T. Suzuki, T. Ogura, K. Hotta, Y. Imamura, Y. Yamaguchi, and H. Handa, "Identification of a primary target of Thalidomide teratogenicity," *Science*, vol. 327, pp. 1345–50, Mar. 2010. 104

[167] S. Fabro, R. L. Smith, and R. T. Williams, "Toxicity and teratogenicity of optical isomers of Thalidomide," *Nature*, vol. 215, pp. 296–296, July 1967. 104

[168] T. K. Devi and A. Bhattacharjee, "A review of liquid crystal dimers," *Assam University Journal of Science & Technology: Physical Sciences and Technology*, vol. 5, no. 2, pp. 225–228, 2010. 104

[169] V. Sharma, M. Crne, J. O. Park, and M. Srinivasarao, "Structural origin of circularly polarized iridescence in jeweled beetles.," *Science*, vol. 325, pp. 449–51, July 2009. 104

[170] C. Pouya, D. G. Stavenga, and P. Vukusic, “Discovery of ordered and quasi-ordered photonic crystal structures in the scales of the beetle Eupholus magnificus.,” *Optics Express*, vol. 19, pp. 11355–64, June 2011. 104

[171] S. A. Jewell, P. Vukusic, and N. W. Roberts, “Circularly polarized colour reflection from helicoidal structures in the beetle Plusiotis boucardi,” *New Journal of Physics*, vol. 9, p. 99, Apr. 2007. 104

[172] T. Lenau and M. Barfoed, “Colours and metallic sheen in beetle shells  a biomimetic search for material structuring principles causing light interference,” *Advanced Engineering Materials*, vol. 10, pp. 299–314, Apr. 2008. 104

[173] F. J. D. Arago, “Mémoire sur une modification remarquable qu’éprouvent les rayons lumineux dans leur passage à travers certains corps diaphanes et sur quelques autres nouveaux phénomènes d’optique,” *Mémoires de la classe des sciences math. et phys. de l’Institut Impérial de France*, vol. 1, p. 93, 1811. 105, 106

[174] F. S. Crawford, *Waves (Berkeley Physics Course Vol. 3)*. McGraw-Hill, 1968. 105, 114, 125

[175] Y. Ye and S. He, “90 polarization rotator using a bilayered chiral metamaterial with giant optical activity,” *Applied Physics Letters*, vol. 96, no. 20, p. 203501, 2010. 105, 107

[176] S. W. Smith, “Chiral toxicology: it’s the same thing...only different.,” *Toxicological sciences*, vol. 110, pp. 4–30, July 2009. 105

[177] L. D. Barron, *Molecular light scattering and Optical activity*. Cambridge University Press, 2004. 105

[178] E. Hecht, *Optics 4th Edition*. Addison-Wesley, 2002. 105, 114, 125

[179] J. B. Pendry, “A chiral route to negative refraction,” *Science*, vol. 306, pp. 1353–5, Nov. 2004. 105

[180] S. Tretyakov, I. Nefedov, A. Sihvola, S. Maslovski, and C. Simovski, “Waves and Energy in Chiral Nihility,” *Journal of Electromagnetic Waves*, vol. 17, pp. 1–9, Nov. 2002. 105

[181] S. Tretyakov, A. Sihvola, and L. Jylhä, “Backward-wave regime and negative refraction in chiral composites,” *Photonics and Nanostructures - Fundamentals and Applications*, vol. 3, pp. 107–115, Dec. 2005. 105

[182] B. Wang, J. Zhou, T. Koschny, M. Kafesaki, and C. M. Soukoulis, "Chiral metamaterials: simulations and experiments," *Journal of Optics A: Pure and Applied Optics*, vol. 11, p. 114003, Nov. 2009. 106

[183] E. Plum, *Chirality and Metamaterials*. PhD thesis, University of Southampton, 2010. 106, 108

[184] N. Wongkasem, C. Kamtongdee, A. Akyurtlu, and K. A. Marx, "Artificial multiple helices: polarization and EM properties," *Journal of Optics*, vol. 12, p. 075102, July 2010. 106

[185] E. Plum, J. Zhou, J. Dong, V. A. Fedotov, T. Koschny, C. M. Soukoulis, and N. I. Zheludev, "Metamaterial with negative index due to chirality," *Physical Review B*, vol. 79, p. 035407, Jan. 2009. 106

[186] K. Konishi, M. Nomura, N. Kumagai, S. Iwamoto, Y. Arakawa, and M. Kuwata-Gonokami, "Circularly polarized light emission from semiconductor planar chiral nanostructures," *Physical Review Letters*, vol. 106, p. 057402, Feb. 2011. 106

[187] E. Hendry, T. Carpy, J. Johnston, M. Popland, R. V. Mikhaylovskiy, A. J. Lapthorn, S. M. Kelly, L. D. Barron, N. Gadegaard, and M. Kadodwala, "Ultrasensitive detection and characterization of biomolecules using superchiral fields.," *Nature Nanotechnology*, vol. 5, pp. 783–7, Nov. 2010. 106

[188] Z. Wu, J. Zhu, M. Jia, H. Lu, and B. Zeng, "A double-layer metamaterial with negative refractive index originating from chiral configuration," *Microwave and Optical Technology Letters*, vol. 53, pp. 163–166, Jan. 2011. 107

[189] J. Zhou, J. Dong, B. Wang, T. Koschny, M. Kafesaki, and C. M. Soukoulis, "Negative refractive index due to chirality," *Physical Review B*, vol. 79, p. 121104, Mar. 2009. 107

[190] Z. Li, H. Caglayan, E. Colak, J. Zhou, C. M. Soukoulis, and E. Ozbay, "Coupling effect between two adjacent chiral structure layers," *Optics Express*, vol. 18, pp. 5375–83, Mar. 2010. 107

[191] Y. Svirko, N. I. Zheludev, and M. Osipov, "Layered chiral metallic microstructures with inductive coupling," *Applied Physics Letters*, vol. 78, no. 4, pp. 498–500, 2001. 107

[192] A. Papakostas, A. Potts, D. M. Bagnall, S. Prosvirnin, H. Coles, and N. I. Zheludev, “Optical manifestations of planar chirality,” *Physical Review Letters*, vol. 90, pp. 1–4, Mar. 2003. 108, 109

[193] A. Potts, A. Papakostas, N. I. Zheludev, H. J. Coles, R. Greef, and D. M. Bagnall, “Planar chiral meta-materials for photonic devices,” *Journal of Material Science: Materials in Electronics*, vol. 14, pp. 393–395, 2003.

[194] A. Potts, A. Papakostas, D. M. Bagnall, and N. I. Zheludev, “Planar chiral meta-materials for optical applications,” *Microelectronic Engineering*, vol. 73-74, pp. 367–371, June 2004. 108

[195] W. Zhang, *Optical activity and applications of planar chiral metamaterials*. PhD thesis, University of Southampton, 2006. 109

[196] V. A. Fedotov, P. Mladyonov, S. Prosvirnin, A. Rogacheva, Y. Chen, and N. I. Zheludev, “Asymmetric propagation of electromagnetic waves through a planar chiral structure,” *Physical Review Letters*, vol. 97, pp. 1–4, Oct. 2006. 109

[197] E. Plum, V. A. Fedotov, and N. I. Zheludev, “Planar metamaterial with transmission and reflection that depend on the direction of incidence,” *Applied Physics Letters*, vol. 94, no. 13, p. 131901, 2009. 109

[198] E. Plum, V. A. Fedotov, and N. I. Zheludev, “Asymmetric transmission: a generic property of two-dimensional periodic patterns,” *Journal of Optics*, vol. 13, p. 024006, Feb. 2011. 109

[199] N. Fang, H. Lee, C. Sun, and X. Zhang, “Sub-diffraction-limited optical imaging with a silver superlens.,” *Science (New York, N.Y.)*, vol. 308, pp. 534–7, Apr. 2005. 113

[200] U. Fano, “Effects of configuration interaction on intensities and phase shifts,” *Physical Review*, vol. 124, pp. 1866–1878, Dec. 1961. 116

[201] J. D. Edmunds, M. C. Taylor, A. P. Hibbins, J. R. Sambles, and I. J. Youngs, “Babinets principle and the band structure of surface waves on patterned metal arrays,” *Journal of Applied Physics*, vol. 107, no. 10, p. 103108, 2010. 118

[202] A. P. Hibbins, R. J. Sambles, C. R. Lawrence, and J. Brown, “Squeezing millimeter waves into microns,” *Physical Review Letters*, vol. 92, p. 143904, Apr. 2004. 118